

BIOMASS BURNING AND ITS RELATIONSHIP WITH WATER CYCLE
DYNAMICS OF THE CHARI-LOGONE CATCHMENT OF LAKE CHAD BASIN

A THESIS IN
Environmental and Urban Geosciences

Presented to the Faculty of the University of
Missouri-Kansas City in partial fulfillment of
the requirements for the degree

MASTER OF SCIENCE

By
Forrest Black

B.A., Geography
University of Missouri - Kansas City

Kansas City, Missouri
2018

© 2018

FORREST BLACK

ALL RIGHTS RESERVED

BIOMASS BURNING AND ITS RELATIONSHIP WITH WATER CYCLE
DYNAMICS OF THE CHARI-LOGONE CATCHMENT OF LAKE CHAD BASIN

Forrest Black, Candidate for the Master of Science Degree

University of Missouri-Kansas City, 2018

ABSTRACT

The present study investigates the effect of biomass burning on the water cycle dynamics of the Chari-Logone catchment, which is the primary water source of Lake Chad, in central sub-Saharan Africa, providing approximately 95% of surface water inflow to the lake. A significant challenge in calculating water balance for this region is the lack of meteorological station data and the low temporal frequency of sampling by the few existing stations. WetSpass-M, a monthly water balance model, was chosen for this study due to its ability to calculate water balance without the large amount of data that many other models require. Satellite observations from TRMM, MODIS, and SRTM, and other earth science missions provide well distributed data at reasonable spatial scales. For a more comprehensive look at the effects of burning, i.e. albedo change, which has been shown to have a significant impact on a number of environmental factors, was considered when calculating potential evapotranspiration as a model input. Two water balance simulations, one considering burning and one without, were compared from the years 2003 to 2011. A groundwater model was also built using Processing MODFLOW, using actual evapotranspiration from both burning and non-burning water balance outputs.

The resulting calculated runoff from the model agreed well with ground observations, with a Nash-Sutcliffe Efficiency of 0.57. Seasonal analysis shows a correlation between water-cycle parameters and burning, and is affected by the region's seasonal variability, where burning increases during the dry season and decreases during the wet season.

The groundwater model performed well for dry season months when there was less rainfall. However, when wet season evapotranspiration (ET) was used, the model over exaggerated the groundwater levels. This was most likely due to the way the groundwater and evapotranspiration parameters are handled in WetSpas-M.

When the primary land cover types were studied (grass, savanna, and cropland); all three land cover types showed a significant reduction in ET. This is shown by average wet season ET decreasing $-5.E+13$ m³per month and a decrease $7.E+13$ m³for the dry season months. This lends support to the hypothesis that with increased burning, there is a decrease in certain hydrologic parameters including precipitation.

APPROVAL PAGE

The faculty listed below, appointed by the Dean of the College of Arts and Sciences have examined a thesis titled "Biomass Burning and Its Relationship with Water Cycle Dynamics of the Chari-Logone Catchment of Lake Chad Basin" presented by Forrest Black, candidate for the Master of Science degree, and hereby certify that in their opinion it is worthy of acceptance.

Supervisory Committee

Jejung Lee, Ph.D., Committee Chair and Research Advisor
Department of Geosciences

Wei Ji, Ph.D.
Department of Geosciences

Tina Niemi, Ph.D.
Department of Geosciences

CONTENTS

ABSTRACT	iii
ILLUSTRATIONS	ix
TABLES	xii
ACKNOWLEDGEMENTS	xiii
Chapter	
1. INTRODUCTION.....	1
1.1 Statement of Problems.....	1
1.2 Purpose of Study.....	3
1.3 Biomass Burning	4
2. WetSPASS-M	7
2.1 Basic Concept of WetSpass-M.....	7
2.2 Water Balance Calculation in WetSpass-M	8
3. LITERATURE REVIEW	11
4. METHODOLOGY	15
4.1 Precipitation.....	15
4.2 Soil.....	20
4.3 Land Cover	21
4.4 Temperature.....	38
4.5 Wind Speed.....	41

4.6 PET	43
4.7 Elevation	49
4.8 Groundwater	50
4.9 Processing Results	51
4.10 Groundwater Model.....	52
5. RESULTS.....	62
5.1 Water Balance Model Validation	62
5.2 Analysis of CLC Water Balance	67
5.3 Analysis of Water Balance by Land Cover Type	71
5.4 Groundwater Model Results.....	74
6. CONCLUSION	77
APPENDIX.....	79
A. WetSpass-M Land Use Look-up Table	79
B. NOAA NCEI Global Summaries of the Day Stations Used for Averaging Monthly Wind Speed	81
C. Python Program for Wind Speed Data	82
D. Albedo Table of Land Use Without Fire.....	84
E. Albedo Table of Land Use Considering Fire.....	85
F. NOAA NCEI Climate Stations Used for Relative Humidity and to Calculate Extraterrestrial Radiation and Surface Radiation.....	86

G. ASCII to Tiff Arcpy Tool.....	90
H. Summation of Raster by Land Use Class Arcpy Tool	92
I. BGR Stations Used for River Input in Groundwater Model.....	97
REFERENCES	98
VITA.....	106

ILLUSTRATIONS

Figure	Page
1. Map of Lake Chad Basin located in Sahelian Africa.....	2
2. LCB regional cumulative rainfall anomalies taken from climate stations.....	4
3. Schematic representation of water balance in a non-homogeneous land-cover pixel	9
4. Conceptual diagram of recharge in WetSpass-M.	10
5. Climate stations in Lake Chad Basin with continuous monthly data for 2005.....	15
6. GIS model for precipitation input rasters for WetSpass-M.	17
7. Comparison of February 2006 precipitation data.	19
8. Soil map of Chari-Logone catchment using data from the Harmonized World Soil Database.....	21
9. ArcGIS model for processing land cover inputs into WetSpass-M.....	25
10. Land cover map of Chari-Logone catchment based on modified MODIS MDC12Q1 (Type1) land cover.....	26
11. MODIS bowtie-effect	28
12. January 2010 fire counts from MOD14.....	30
13. August 2010 fire counts from MOD14.....	31
14. GIS model for creating land cover rasters considering burning	32
15. 2010 map showing WetSpass-M land use classifications	33
16. January 2010 map showing WetSpass-M land use classifications.	34
17. Distribution of land cover percentages in the Chari-Logone catchment.	37

18. Average percent of monthly burning for major land cover types.....	38
19. ArcGIS model used to process temperature raster inputs.....	39
20. January 2010 land surface temperature model input.....	40
21. Monthly temperature averages from 2003-2011.....	41
22. ArcGIS model used to process monthly averaged winds.....	42
23. ArcGIS model used to create PET considering burning and non-burning scenarios ..	45
24. PET considering burning for January 2010.....	46
25. PET not considering burning for January 2010.....	47
26. CGIAR 1950 - 2000 monthly averaged PET for January.....	48
27. Comparison of averaged PET by month against CGIAR data..	49
28. Chari-Logone elevation from SRTM DEM.....	50
29. Map of groundwater levels used for input into GIS.....	51
30. GIS model for extracting WetSpas-M outputs by vegetative class.....	52
31. Cholera cases, deaths, and cholera fatality rate (CFR) from 1971-2011.....	54
32. Cross-Section of Lake Chad Basin geology.....	55
33. Geology of Chari-Logone Catchment.....	56
34. Schematic of a finite difference grid.....	57
35. Groundwater Model Grid in PMWIN.....	58
36. Hydraulic head map used in study overlaid on map of Chari-Logone Catchment	61
37. Flow map of Chari-Logone Catchment	63

38. Calculated discharge not considering rainy days per month	63
39. Calculated discharge considering rainy days per month and using site specific WetSpass-M settings compared to measurements from Bongor station.	65
40. Scatter plot of monthly discharge data from Bongor station compared to model outputs considering burning.....	66
41. Averaged water balance output parameters from burning model compared to calculated PET considering albedo change from burning.	67
42. Correlation coefficients between biomass burning count ompared to water balance model outputs considering burning.....	69
43. Scatter plot of monthly biomass burning count against precipitation.....	70
44. Average output difference from model considering minus model not considering burning.	71
45. Scatterplot of well observations to groundwater model calculated heads not considereing ET.	73
46. Scatterplot of well observations to groundwater model calculated heads considereing January 2009 ET data from WetSpass-M outputs.	75
47. Potentiality map of Chari-Logone Catchment showing depth to water table.	76

TABLES

Table	Page
1. Conversion table of MODIS land cover class values to WetSpass-M class values.....	23

ACKNOWLEDGEMENTS

First and foremost, I thank God for creating such a magnificent earth to study. It is with deep gratitude that I thank my mentor and thesis advisor, Jejung Lee, for his wisdom and instruction in research, especially this project. He has been a source of inspiration and an incredible instructor on many aspects of earth science. Professors Wei Ji and Tina Niemi have my sincere thanks for serving as my thesis committee, giving input and advice on this thesis.

I am also grateful to scientists at NASA Goddard Space Flight Center who have helped me with this study. Charles Ichoku and Luke Ellison provided essential fire data and insight in this project. Charles Gatebe provided advice and data pertaining to the effect of burning on surface albedo change.

Rakiya Babamaaji has my sincere thanks for helping me to understand how to run the seasonal model of WetSpass and Changhui Park was vital to getting WetSpass to run. Khodayar Abdollahi deserves many thanks for helping me to run WetSpass-M and calibrate the model.

Finally, I would like to thank parents Ward and Laurie, my sister Julia, and my girlfriend April along with the many family and friends that have given tremendous support and encouragement throughout my academic journey.

CHAPTER 1

INTRODUCTION

1.1 Statement of Problems

Environmental and meteorological systems are large and complex yet imperative to study in order to plan for the future and mitigate potential damage. One area that has received particular attention from the scientific community and the general public is Lake Chad, which is located in sub-Saharan Africa. The lake has shrunk, from 25,000 km² in 1963 to less than 3,000 km² in 2008 (Musa, 2008). The Lake Chad Basin (LCB) is the total area where precipitation is collected and drained into a common outlet, in this case, Lake Chad (Figure 1). The LCB is home to more than 8.2 million people and a diverse ecosystem that has been greatly impacted by extreme change in lake water availability (WHO, 2017). Lake Chad's shrinkage is significantly detrimental to regional sustainability as it is an economically important water resource that agricultural and fishing industries depend upon. In a series of surveys conducted in 1993 under the British Government fisheries research project, 25,000 households living along the southwestern portion of Lake Chad were interviewed. 59% of the households earned three-quarters of their income from farming, 36% earned income from a combination of fishing and farming, and only 5% relied entirely on fishing (Sarch, 2001).

A number of factors have been attributed to lake shrinkage including decrease in precipitation (Kimmage & Adams, 1992), poor water management practices (FAO Water 2009), and land use change (Babamaaji & Lee, 2014). Another factor influencing environmental change is the occurrence of biomass burning, whether through wildfires or human induced burning. Biomass burning has been shown to have significant impacts on

climate by altering land cover and vegetation (Thonicke, Venevsky, Sitch, & Cramer, 2001; Lyons, Jin, & Randerson, 2008; Bowman et al., 2009), introducing aerosols (Ichoku & Ellison, 2014; van der Werf et al., 2010), and changing land surface characteristics especially in regard to surface albedo (De Sales, Xue, & Okin, 2014; Gatebe, Ichoku, Poudyal, Román, & Wilcox, 2014). Though there have been an increasing number of studies looking at burning using general circulation models, there are few studies on regional burning effects and even fewer at the local scale.

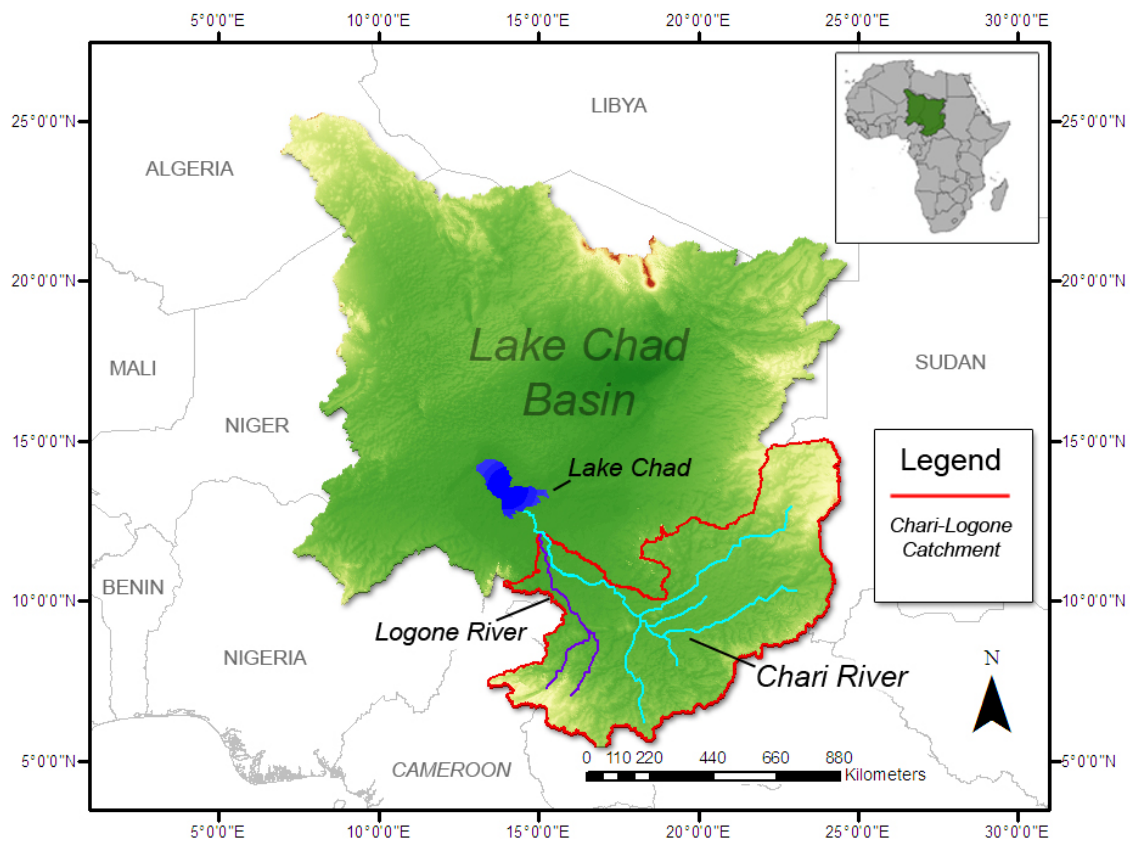


Figure 1. Map of Lake Chad Basin located in Sahelian Africa.

1.2 Purpose of Study

The purpose of this study is to quantitatively determine how biomass burning affects important water cycle parameters within the LCB. The water cycle is the continuous movement of water within the earth system and can be divided into the hydrologic processes of precipitation, interception, runoff, evapotranspiration, infiltration, and recharge. The Chari-Logone catchment (CLC), a sub-basin of LCB (Figure 1), was chosen for this study as it provides 95% of the water input to Lake Chad and is the main driver for the entire lake system (Gao, Bohn, Podest, McDonald, & Lettenmaier, 2011). The Chari and Logone rivers provide an average of 1,946 mm/year to the lake whereas direct rainfall contributes a mere 329 mm annually (Babamaaji, 2013). The spatial extent of the study area is 601,350 km² and is located within the borders of Cameroon, Chad, Central African Republic, and Sudan. The catchment lies between 5° N and 15° N at the eastern part of the Sahel (Figure 1).

Most of the rainfall in the Lake Chad is immediately lost to evapotranspiration (ET) (Bouchez et al. 2016) leaving the region sensitive to precipitation anomalies. Precipitation in the region is bi-seasonal with wet season monsoonal rains lasting from April to October and the dry season the rest of the year. The monsoonal rains are driven by the Intertropical Convergence Zone (ITCZ), created by the convergence of trade winds from the northern and southern hemispheres forming the ascending branch of the Hadley circulation (Nicholson, Some, & Kone, 2013) (Figure 2). ITCZ precipitation in the Sahel has been shown to be affected by the El Niño-Southern Oscillation (ENSO) system, which is a cycle of ocean and atmospheric interaction. During El Niño years, flow from the West African Monsoon has been shown to create a dry condition across the

Sahel region leading to precipitation deficits (Nicholson, Some, & Kone, 2000). High variability of rainfall due to these meteorological factors have contributed to a series of droughts in the 1970s and 1980s with a gradual annual rainfall recovery occurring since the 1980s.

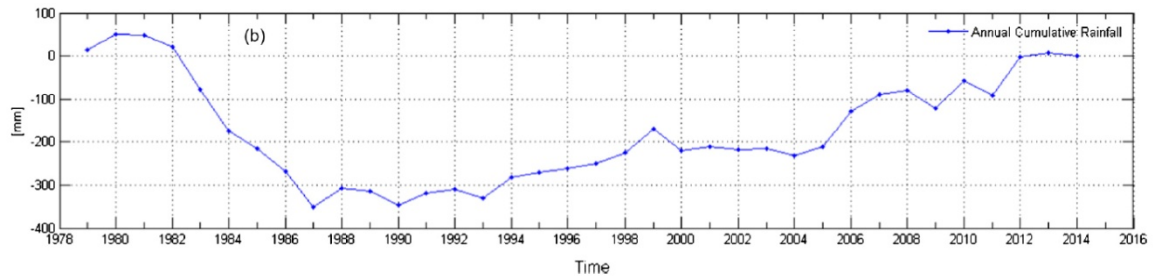


Figure 2. Annual cumulative rainfall anomalies averaged over LCB GPCP based precipitation. (Ndehedehe, Awange, Kuhn, Agutu, & Fukuda, 2017).

Land cover in the CLC is primarily composed of grassland, savanna, and cropland. Other land cover types in the catchment include bare soil, wetland, forest, and urban areas (Babaamaji et al., 2014). While the vast majority is grassland, it is worth noting that the confluence of the Chari and Logone rivers, draining into Lake Chad, is primarily cropland. The percentage of each land cover type plays an important part in the water cycle. For example, interception is greatly affected by tree canopy preventing precipitation from reaching the soil. Additionally, the amount of transpiration depends on vegetative type (Tsiko, Makurira, Gerrits, & Savenije, 2012).

1.3 Biomass Burning

A large contributor to biomass burning within the CLC is the use of fire to remove vegetative growth at the end of a growing season and the clearing of grassland and

savanna for agricultural use. At the early to late dry season (November-April), a patch mosaic burning regime has been used historically by the indigenous people to clear savannah and woody areas of wild animals and facilitate clearing land for planting crops. With European colonization, this practice was discouraged out of fear of it causing land degradation. Burning primarily occurs during the dry season, when rainfall is at a minimum, to clear the wet season's growth or to convert the land for future agricultural use. There are however caveats to biomass burning environmentally. Aerosol byproducts of biomass burning have been known to produce significant amounts of black carbon, carbon monoxide, and carbon dioxide (*e.g.* Ichoku et al., 2014). Furthermore, the resultant ash and charcoal deposition, as well as change in land cover, have been known to have a significant impact on surface albedo (Gatebe et al., 2014; Govaerts, Pereira, Pinty, & Mota, 2002; Maier, Ebke, & Ruppert, 2005).

Surface albedo is the ratio of solar radiation reflected from a surface to total radiation received by the surface. The values of surface albedo range from 0 (completely absorption), to 1 (completely reflected). Albedo surface darkening from burning is caused by char deposition that increases absorption of solar radiation, whereas albedo lightening can occur when wind and precipitation remove the burnt surface layer to expose the bare soil underneath (Saha, D'Odorico, & Scanlon., 2017).

Desales et al. (2016) found that change in albedo coupled with a decrease in leaf area index (LAI) and vegetative land cover fraction from burning was linked to convective instability. The cause of this convective instability and precipitation loss is a cooling and drying of the atmosphere leading to the weakening of upward atmospheric motion during the onset and mature stages of the monsoon.

Biomass burning effect on water cycle in the Sahel have been addressed to some degree in regard to ET, soil moisture, and precipitation, but conclusive evidence is limited by issues associated with burning and vegetative seasonality (Ichoku et al., 2016). Other studies associating water cycle changes with burning include its effect soil infiltration rates, surface runoff (De Bano, 1981), and soil erosion (Rulli, Offeddu, & Santini, 2005; Nyman et al., 2015). The time period chosen for this study is from 2003 to 2011 in order to use albedo change from burning as described by Gatebe et al. (2014).

CHAPTER 2

WetSPASS-M

2.1 Basic Concept of WetSpass-M

Previous studies on the water cycle of Sahelian regions use models focused on terrestrial water storage (TWS) using data from satellites such as the Gravity Recovery and Climate Experiment (GRACE) (Buma, Lee, & Seo, 2016; Ndehedehe et al., 2017; Ramillien, Frappart, & Seoane, 2014). While these models have made significant advances in understanding hydrologic dynamics on a climate scale, the spatial resolution is too coarse for this study. Lack of *in-situ* data is largely due to few meteorological stations that provide only inconsistent data on a daily or even monthly basis (Eklund, Romankiewicz, Brandt, M., Doevenspeck, & Samimi, 2016; Sanogo et al., 2015; Zhang, Brandt, Guichard, Tian, & Fensholt., 2015). Additionally, installing new stations is difficult in the CLC due to insecurity in the region. WetSpass, which stands for Water and Energy Transfer between Soil, Plants and Atmosphere under quasi-Steady State, is a physically-based water balance model that is not as data intensive as those previously mentioned though it operates at a seasonal time scale (Batelaan & De Smedt, 2007). Babamaji (2013) demonstrated the effective use of WetSpass in Lake Chad. A drawback of WetSpass is its inability to calculate water balance beyond a seasonal scale. This, however, has been somewhat corrected through the introduction of WetSpass-M.

WetSpass-M has shown favorable results for modeling water balance in the western Sahel in the Black Volta Basin (Abdollahiet al., 2017) and in Northern Africa (Melki, 2017).

Water balance is the conservation of hydrologic inputs and outputs within a system. The water balance equation used by WetSpass-M is:

$$P = ET + S + R \quad (1)$$

where P is the precipitation, ET is the actual evapotranspiration, S is the surface runoff, and R is the groundwater recharge.

2.2 Water Balance Calculation in WetSpass-M

WetSpass was previously reliant on a Geographic Information System (GIS) program, but WetSpass-M is able to run as a stand alone program using Iron Python and its stand alone computational spatial engine H2PL. WetSpass-M utilizes raster data for input and treats a basin or region as a regular pattern of raster cells, which are then sub-divided into vegetated, bare soil, open water, and impervious surface fraction. Water balance calculation of each pixel is processed in the following order: interception (process 1), surface runoff (process 2), evapotranspiration (process 3), and recharge (process 4) (Figure 3). Additionally, land-use/land-cover fraction values for each pixel are used as weighting factors for the calculation of the water balance (Abdollahi, 2015).

Recharge, being the final process, is the residual water from the other water balance processes:

$$R = P - S - ET \quad (2)$$

Where R is the recharge, P is the precipitation, S is the surface runoff and ET is the evapotranspiration. This differs from WetSpass, which depicted groundwater in long-term spatial patterns. For each monthly calculation, the water storage of the previous month and the groundwater recharge are used to calculate base-flow for each cell.

However, static and interflow between cells is not considered in the calculation. Recharge in WetSpass-M is a combination of soil-water storage and baseflow.

Soil-water storage, or the amount of water stored in the plant root zone of soil, is a function of the surface area of soil particles and the porosity (void spaces between soil particles). Baseflow refers to the portion of groundwater contributing to a stream. Therefore, WetSpass-M does not consider the portion of recharge that is contributed to the water table, only the water near the surface (Figure 4).

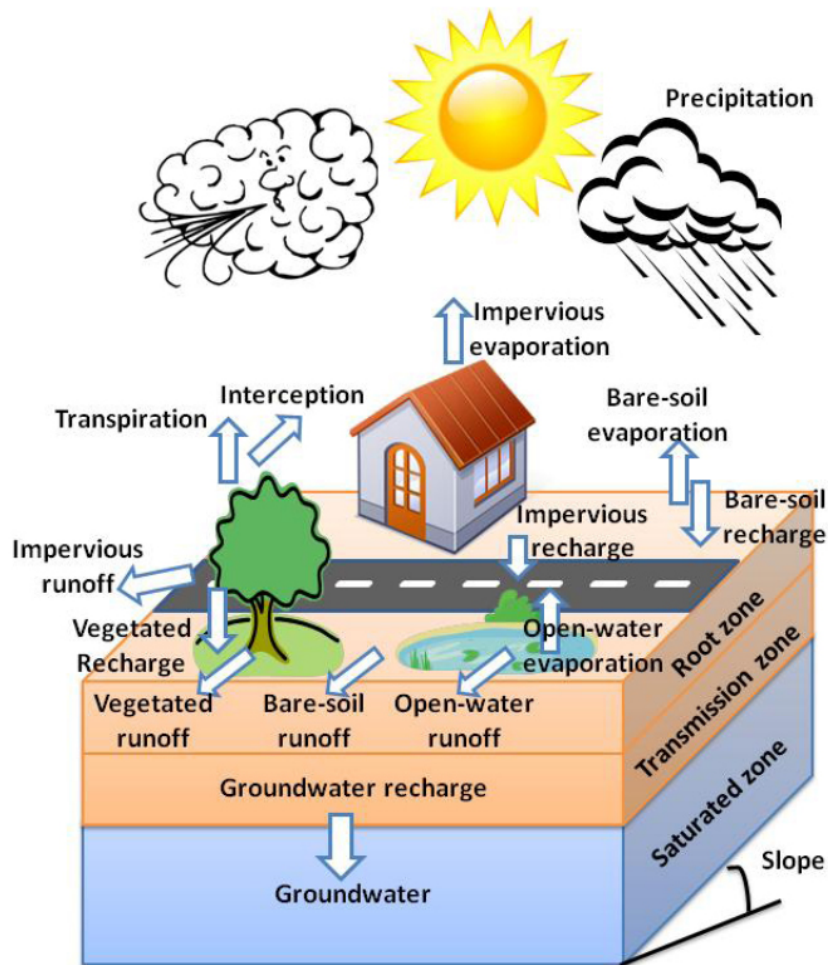


Figure 3. Schematic representation of water balance in a non-homogeneous land-cover pixel (Batelaan & De Smedt, 2001; Batelaan & De Smedt, 2007; Ampe et al., 2012)

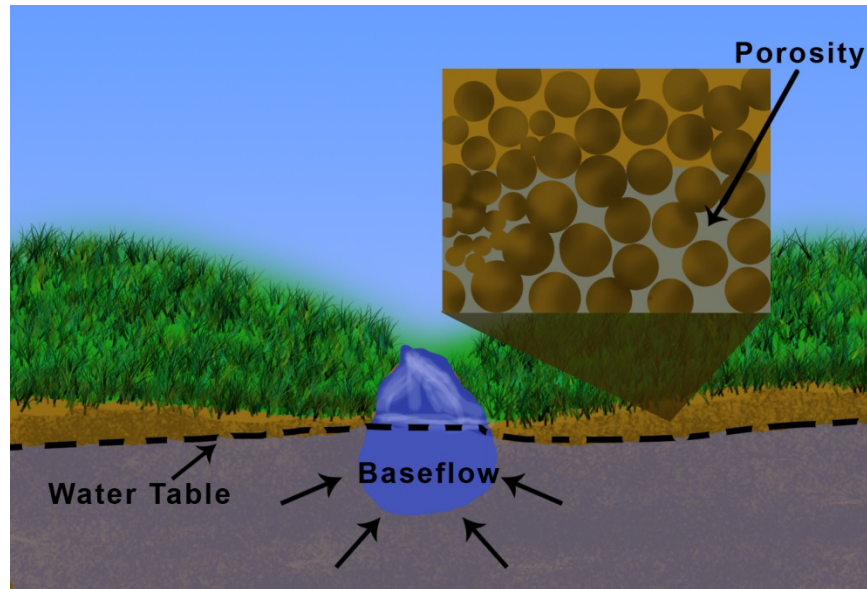


Figure 4. Conceptual diagram of recharge in WetSpass-M.

Raster datasets required for input into WetSpass-M include precipitation, temperature, wind, soil, land cover, elevation, slope, and potential evapotranspiration (PET).

The model outputs of the water balance model are interception, actual evapotranspiration, surface runoff, and recharge; the summation of which are equal to precipitation. WetSpass-M calculates impervious or actual evapotranspiration using vegetation coefficients in conjunction with potential evapotranspiration.

CHAPTER 3

LITERATURE REVIEW

There have been a number of studies of the Lake Chad Basin, though usually focusing focus on the basin as a whole and not specifically the CLC watershed. Many of these studies look at change in lake level and stream flow to the lake (Vuillaume, 1981; Coe & Foley, 2001; Leblanc et al. 2003; Schuster, et al., 2005; Leblanc, et al., 2007; Le Coz, et al., 2009). One such study by Coe and Foley (2001), quantified a response in Lake Chad to discharge loss in the Chari-Logone river system induced by climate variation. Their method utilized two different models, IBIS (the integrated biosphere simulator) a land surface biophysics model and HYDRA (the hydrological routing algorithm) for hydrology. Their model was at the course resolution of $0.5^{\circ} \times 0.5^{\circ}$ and covered the years 1953-1979. Data used for the models came from one source, the Climate Research Unit of the University of East Anglia, Norwich, providing temperature, precipitation, humidity, and cloudiness. Coe and Foley (2001) showed that a decrease in lake area was primarily due to decreased precipitation and increased water loss from irrigation. Irrigation alone was found to reduce river discharge an average of 33% annually. The study also found that the lake area was reduced by approximately 45% for the study period.

Early studies of LCB calculating water balance parameters, relied exclusively on collecting *in situ* data (Isiorho & Nkereuwem, 1996; Carter, Morgulis, Dottridge, & Agbo, 1994). More recent studies have made use of remote sensing. While often not as accurate as climate station data, provides better spatial coverage and temporal continuity.

However, these studies, though using some remote sensing data, rely heavily on station data.

LeCoz, Delclaux, Genthon, & Favreau (2009) used Digital Elevation Model (DEM) data from Shuttle Radar Topography Mission (SRTM) for input into THMB (Terrestrial Hydrology Model Biogeochemistry). THMB is a physically based water balance model operating at a 10 km x 10 km resolution and statistical methods in spatial downscaling were tested to see how the SRTM DEM data, with a 90 m resolution might best be aggregated to 90 km for use in THMB . The investigation found that mean and median methods produce a smoother representation of the topography. Though water balance calculations were performed, only surface runoff was considered for drainage comparison.

Babamaaji (2013) used the physically based model WetSpas to calculate water balance parameters from 2003 to 2010 on a seasonal scale (6 month). The resolution for the model was 2 km x 2 km and used a combination of satellite and climate station data. Station data was used for ET, windspeed, temperature, and relative humidity. Though station data was limited it worked well on a seasonal scale with groundwater recharge estimates matching closely to another study.

Babamaaji (2013) found that it is evident from the simulated results that precipitation is the highest controlling factor followed by land use-land cover (LULC) and soil texture in the basin influencing ET, runoff, interception and recharge. Surface runoff were found to account for about 50 - 70% for the built-up impervious surfaces, which is 2 to 3 times higher than the runoff from the agricultural land. Annual mean ET was also found to account for 90% of the annual precipitation. Savanna and agricultural land indicated a

higher sensitivity to the change of precipitation in balancing transpiration and soil evaporation.

Studies of the Quaternary aquifer underlying a portion of the CLC, have investigated recharge and water storage loss using a variety of computational models (Eberschweiler, 1993; Leblanc, 2002; Boronina, Favreau, Coudrain, Leduc, & Dieulin, 2007). Boronina and Ramillien (2008) use GRACE (gravity recovery and climate experiment) and AVHRR (advanced very high resolution radiometer) data for input into S-SEBI. S-SEBI is a surface energy balance model that calculates ET from net radiation and evaporative fraction. The study found that actual ET over the Quaternary aquifer is highest at the end of rainy season and then it decreases as the surface layers of the soil dry and plants lose their leaves. The study also revealed that over N'Djamena, ET might have been less than annual rainfall with positive annual balance of water storage.

Buma et al. (2016) used GRACE and Global Land Data Assimilation System (GLDAS) data for input into the Water GAP Global Hydrology Model (WGHM) to calculate terrestrial water storage (TWS) a $1^{\circ} \times 1^{\circ}$ resolution. A significant finding of the study is the existence of a phase shift between rainfall and TWS by 1.5 months. From trend analysis, rainfall that precedes TWS increases throughout the study period of 2003-2013. Though there are a number of studies investigating components of water balance change in the LCB, none of the aforementioned investigations examine burning effect on those parameters.

Ichoku et al. (2016) study the effect of burning on Northern South-Saharan Africa (NSSA) from 2001 to 2014 using NDVI, MODIS, and a variety of other satellite data. A finding of particular significance in the study is the effect of burning on hydrological

parameters, especially in savanna areas. Seasonal peak burning was determined to be anticorrelated with annual water-cycle indicators such as precipitation, soil moisture, vegetation greenness, and evapotranspiration. This is important as it shows the contribution of the lag between burning and seasonal precipitation changes.

CHAPTER 4
METHODOLOGY

4.1 Precipitation

Since precipitation is a key input in the water balance calculation, choosing the best dataset available is imperative. Ground station observations from the National Oceanic and Atmospheric Administration's (NOAA) National Center for Environmental Information (NCEI) database are available for sub-Saharan Africa. However, the stations in the study area are relatively few as compared to the United States or Europe and monthly or even yearly data is not always recorded for many stations. African stations are also not always accurate either due to instrument error or poor management (Figure 5).



Figure 5. Climate stations in Lake Chad Basin with continuous monthly data for 2005.

With such few ground stations, even if data is accurate, when the data is interpolated large areas within the study area, they are skewed based on spatial distribution. Even station data averaged on a seasonal time scale does not match the spatial resolution of TRMM. For these reasons, data from the National Aeronautics and Space Administration (NASA) Tropical Rainfall Measurement Mission (TRMM) was used for precipitation. The TRMM satellite was launched November 27, 1997 in a joint space mission between the National Aeronautic and Space Administration (NASA) and the Japan Aerospace Exploration Agency (JAXA) designed to monitor subtropical precipitation systems (Simpson et al., 1988). Data from TRMM is available to the public in a variety of products. TRMM level 3 combined rainfall product 3B31 was used for the study, with a 0.5 degree x 0.5 degree resolution at a monthly time scale and units in mm/month. The data covers the area from 40°N to 40°S latitude, and were collected from January 1998 to April 2015, shortly before the satellite re-entered Earth's atmosphere. A number of studies have examined the accuracy of TRMM data compared to station data in different regions (Hughes, 2006; Li and Shao, 2010; Pombo and Proença de Oliveira, 2015). One such study by Ojo and Omotosho (2003) looked specifically at the accuracy of TRMM in Nigeria. The study found that TRMM performed very well when compared to the few meteorological stations available (Figure 7). TRMM did however have a tendency to marginally over estimate precipitation especially toward southwestern Nigeria.

At the time of download, the data were only available in HDF4 format. HDF4 is a compressed multi-dimensional format file type and was not georeferenced. A model was

built using ESRI's ArcMap Model Builder to process the TRMM data for input into WetSpass-M.

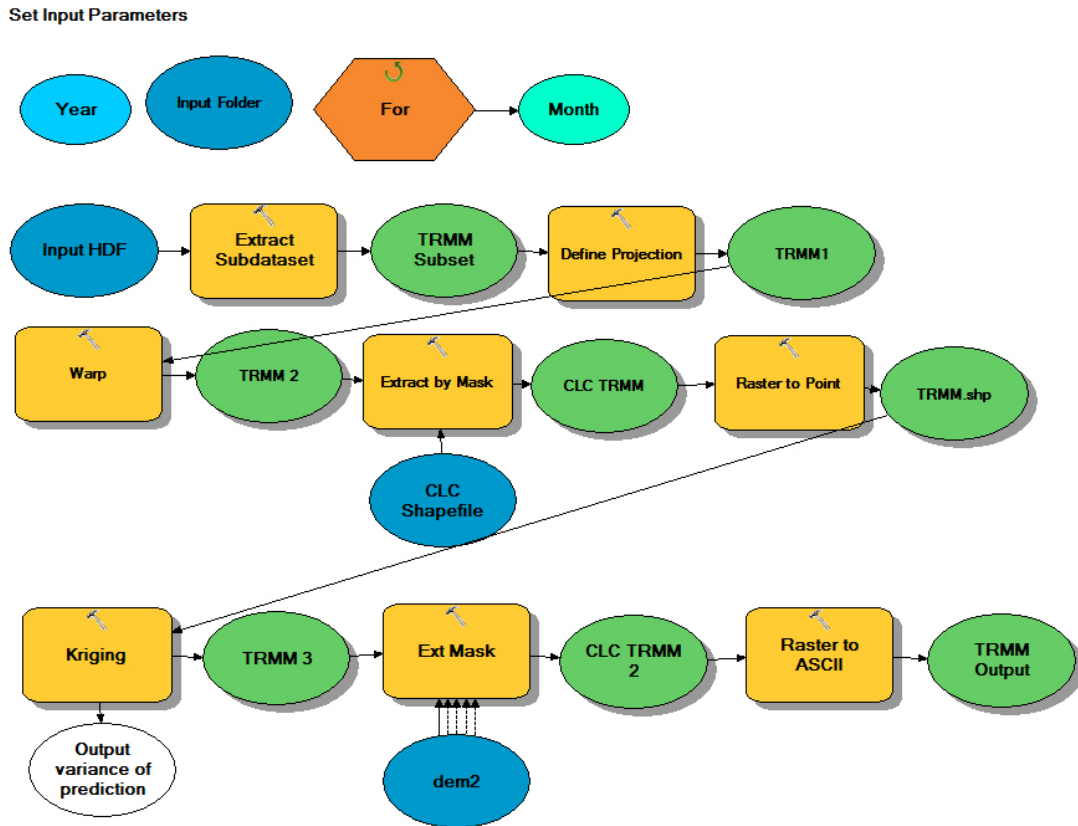


Figure 6. GIS preprocessing model for precipitation input rasters for WetSpass-M.

The data were first imported into ArcMap using the Extract Subdataset tool. The data were then georeferenced to the WGS 1984 projection and the data were rotated and moved to the correct latitude and longitudinal coordinates using the warp tool. Due to the large size of the raster, a subset of the data were extracted and converted to a point-type shapefile. The data was re-sampled to a 2 km by 2km resolution to compare to data from Babamaji (2014) and used for inputs. This was accomplished using kriging with an exponential semi-variogram. The study area raster was then extracted from the kriged

dataset using the environmental properties snap to raster and extract by mask. This was vital, because the number of cells, size, and location of cells needed to match exactly for each input raster used in WetSpass-M. Finally, the data was exported to an ASCII filetype, which is the required format for WetSpass-M to process the raster input data.

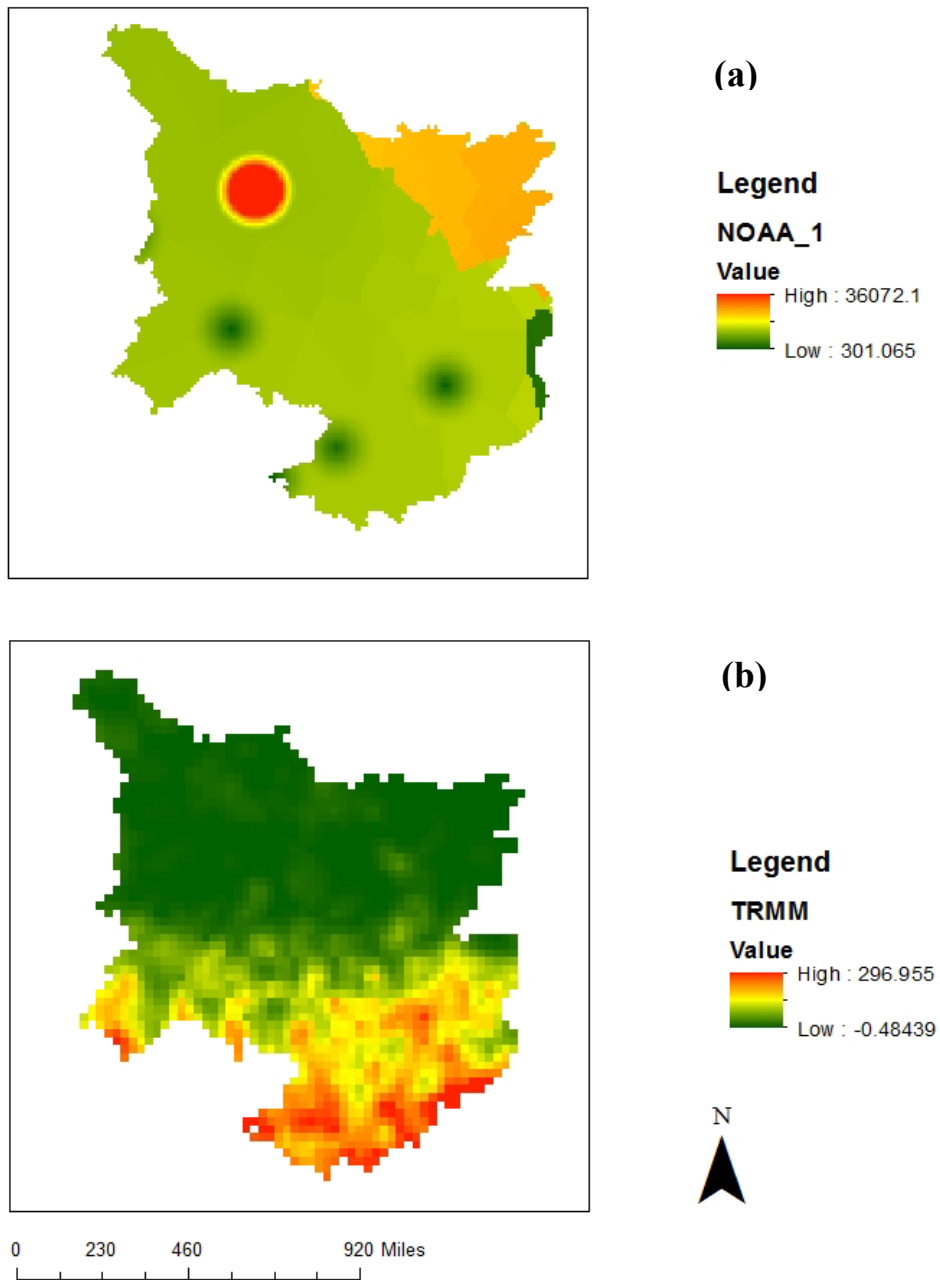


Figure 7. Comparison of February 2006 precipitation data. (a) NOAA NCEI stations with faulty data entry in the red area and poor distribution. (b) TRMM 3B31 at 1 km x 1 km resolution.

4.2 Soil

Soil data was extracted from the United Nation's Food and Agriculture Organization (FAO) Harmonized World Soil Database (HWSD). The HWSD was developed in response to a need for a refined dataset for modeling land use and land cover changes addressed in the 1997 International Institute for Applied Systems Analysis (IIASA) Interim Report. A number of partners including: ISRIC-World Soil Information, European Soil Bureau Network, and the Institute of Soil Science, Chinese Academy of Sciences collaborated in an effort to digitally catalog global soil distribution. HWSD was released in 2008 and is a 30 arc-second raster database with over 16,000 different soil mapping units that combine existing regional and national updates of soil information worldwide (FAO/IIASA/ISRIC/ISS-CAS/JRC 2009). The HWSD raster was imported into ArcGIS (Figure 8) and a ASCII subset was created for the study area for use by WetSpas-M look-up tables.

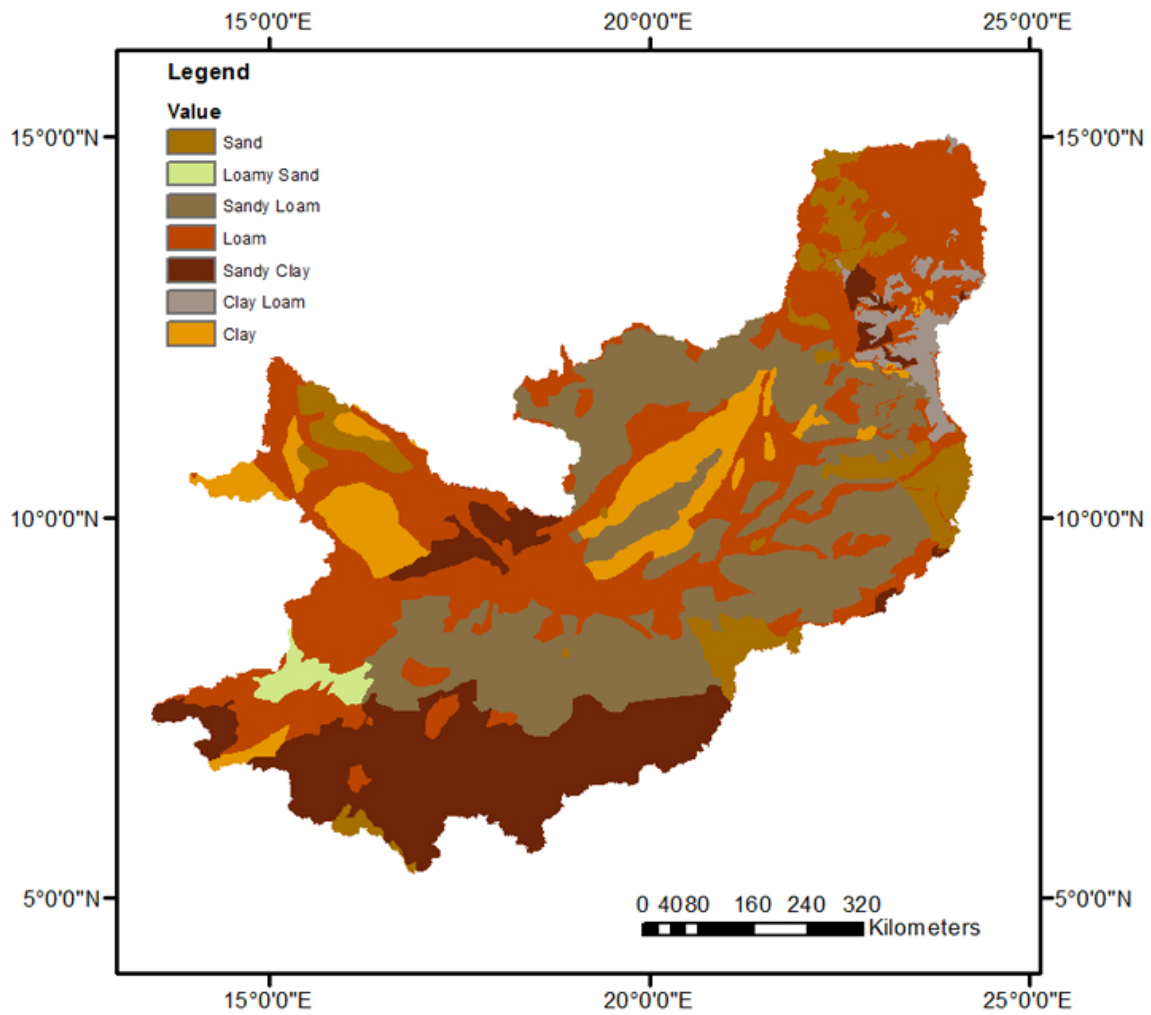


Figure 8. Soil map of Chari-Logone catchment using data from the Harmonized World Soil Database.

4.3 Land Cover

Land cover data were derived from MODIS MCD12Q1 Collection 6 data. This Level 3 dataset is a land classification raster created from an algorithm combining data from the Moderate Resolution Imaging Spectrometer (MODIS) instrument onboard NASA's Terra and Aqua satellites. The satellites were launched December 1999 and May 2002,

respectively. An advantage of MODIS is its ability to capture images every 1-2 days with a 2,330 km wide swath. Thirty-six discrete spectral bands ranging in wavelengths from 0.4 μm to 14.4 μm (Friedl et al., 2002; Friedl et al., 2010). MODIS data has widely been used and validated in a number of studies of Africa (Al-Hamdan et al., 2017; Gessner, Bliefernicht, Rahmann, & Dech, 2012; Ichoku et al., 2016; Vintrou et al., 2012). MCD12Q1 is available yearly at a 1 km x 1 km resolution. The yearly availability of MCD12Q1 makes it preferable in this study over Globcover, which has shown better performance in Africa, but only provides data from December, 2004 - June, 2006 and January - December 2009 (Yang, Xiao, Feng, & Li, 2017).

The MCD12Q1 data is divided into eighteen distinct land classifications, which were converted into another set of classifications required by WetSpas-M. Of the eighteen MODIS classifications only ten were found in the study area. A model was built in ArcGIS to convert the numbers signifying those ten MODIS classes into eight WetSpas-M classes (Table 1).

Table 1. Conversion table of MODIS land cover class values to WetSpass-M class values.

MODIS		WetSpass-M	
Label	Number	Label	Number
Rainfed Cropland	12,14	Agriculture	21
Mosaic Cropland	12,14	Agriculture	21
Mosaic vegetation	12,14	Reference Grassland	307
Forest	6,7	Mixed forest	33
Shrubland	6,7	Shrub	36
Grassland	9,10	Reference Grassland	307
Sparse Vegetation	9,10	Reference Grassland	307
Vegetation regularly flooded	11	Mud flat/Salt marsh	44
Urban area	13	City Centre build-up	1
Bareland	15,16	Excavation(baresoil)	7
Water bodies	0	Lake	52

4.3.1 Non-Burning Land Use Classification

The Table to Table tool converted the CSV format table into a database file which was then joined to the MODIS Raster by the Build Attribute Table tool and the Join Field tool. The Lookup tool was then used to convert the raster values from MODIS to WetSpass-M codes (Figure 10). The primary land use types in the catchment were found to be grassland, cropland, and savanna (Figure 11).

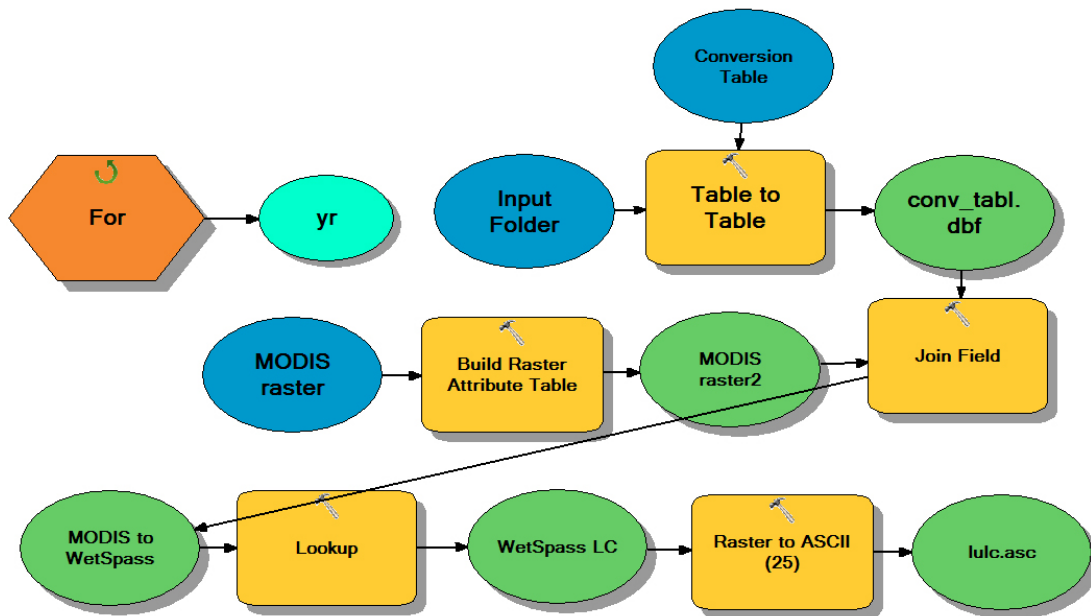


Figure 9. ArcGIS model for processing land cover inputs into WetSpass-M.

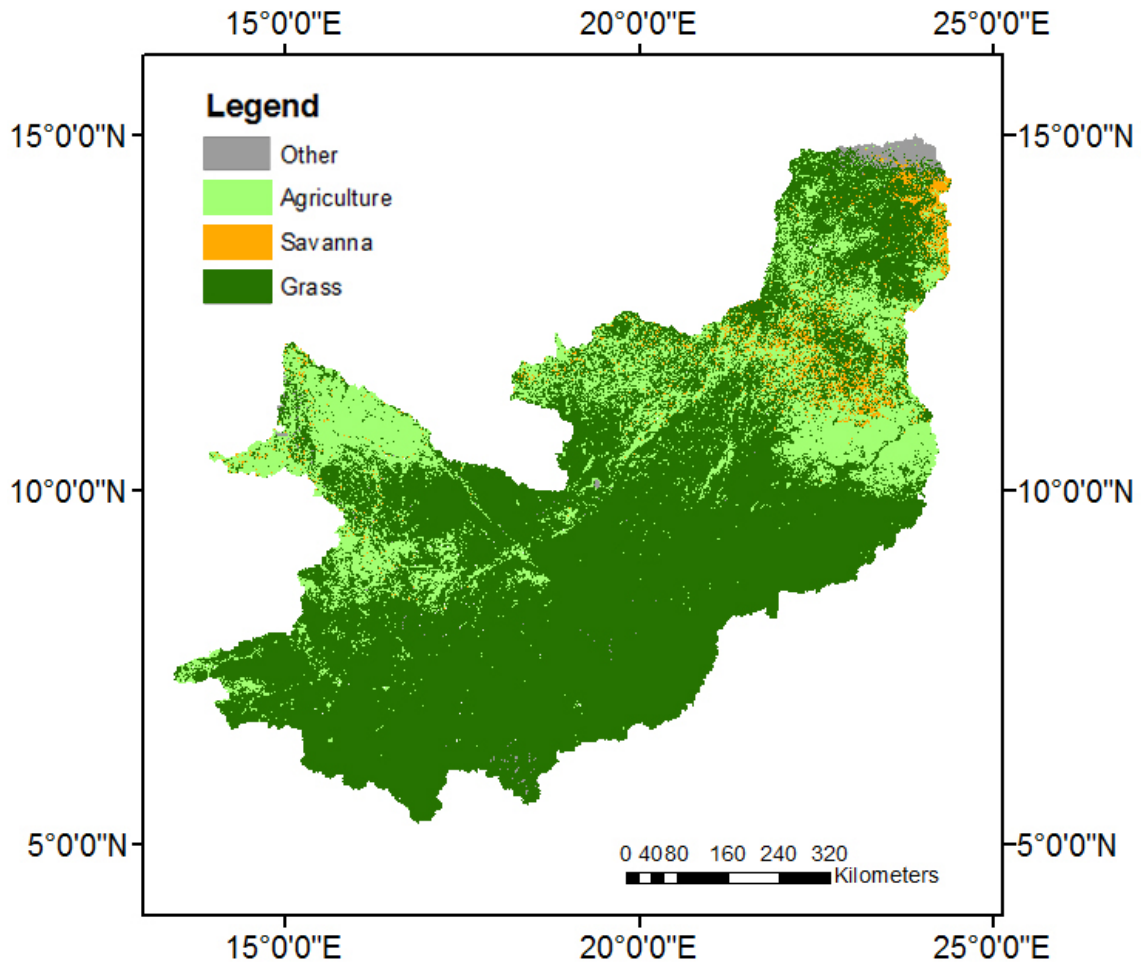


Figure 10. Land cover map of Chari-Logone catchment based on modified MODIS MDC12Q1 (Type1) land cover.

4.3.2 Burned Land Use Classification

To consider the effect of burning on land cover, two different land cover datasets were created, one considering burning and one without burning. The land cover dataset without burning used the methodology previously described. The dataset considering burning merged the exported land cover raster and was combined with fire counts derived from MOD14/MYD14 Collection 5 fire data. MOD14 data is derived from a fire detection algorithm which takes the two 4- μ m channels, numbered 21 and 22. Classification of a

fire pixel requires absolute detection of the fire, if the fire is strong enough, and on detection relative to the thermal emission of surrounding pixels to detect weaker fires (Justice et al., 2002; Giglio, Descloitres, Justice, & Kaufman., 2003). A pixel that is flagged as fire may be referred to as a "count". As MODIS runs along its orbit of the earth, a scan mirror along a track motion generates a simple rectangular array of pixels. The actual viewing geometry of MODIS was designed so that at nadir (the point directly below the satellite) pixel dimensions are 1x1 km. As the scan angle increases from nadir the pixel dimension grows until a pixel is approximately 4.8 x 2 km at either edge of the scan. This distortion is due to the curvature of the earth. The bowtie-shaped area in the scanned swath of ground overlaps with the swath above and below it. Because of this overlap, the same feature on the earth may appear in several scan lines of a MODIS scene if it occurs in a region seen near either edge of the swath (Figure 11). However, this is the way the instrument was designed and not a flaw in the data (Masuoka, Fleig, Wolfe, & Patt., 1998). Level 2 and Level 3 data products available from MODIS already have the bow-tie effect removed. However, since this study used Level 1 data, it was necessary to excluded the duplicate fire detections found in MOD14 using a custom algorithm as detailed by Polivka, Wang, Ellison, Hyer, & Ichoku. (2016).

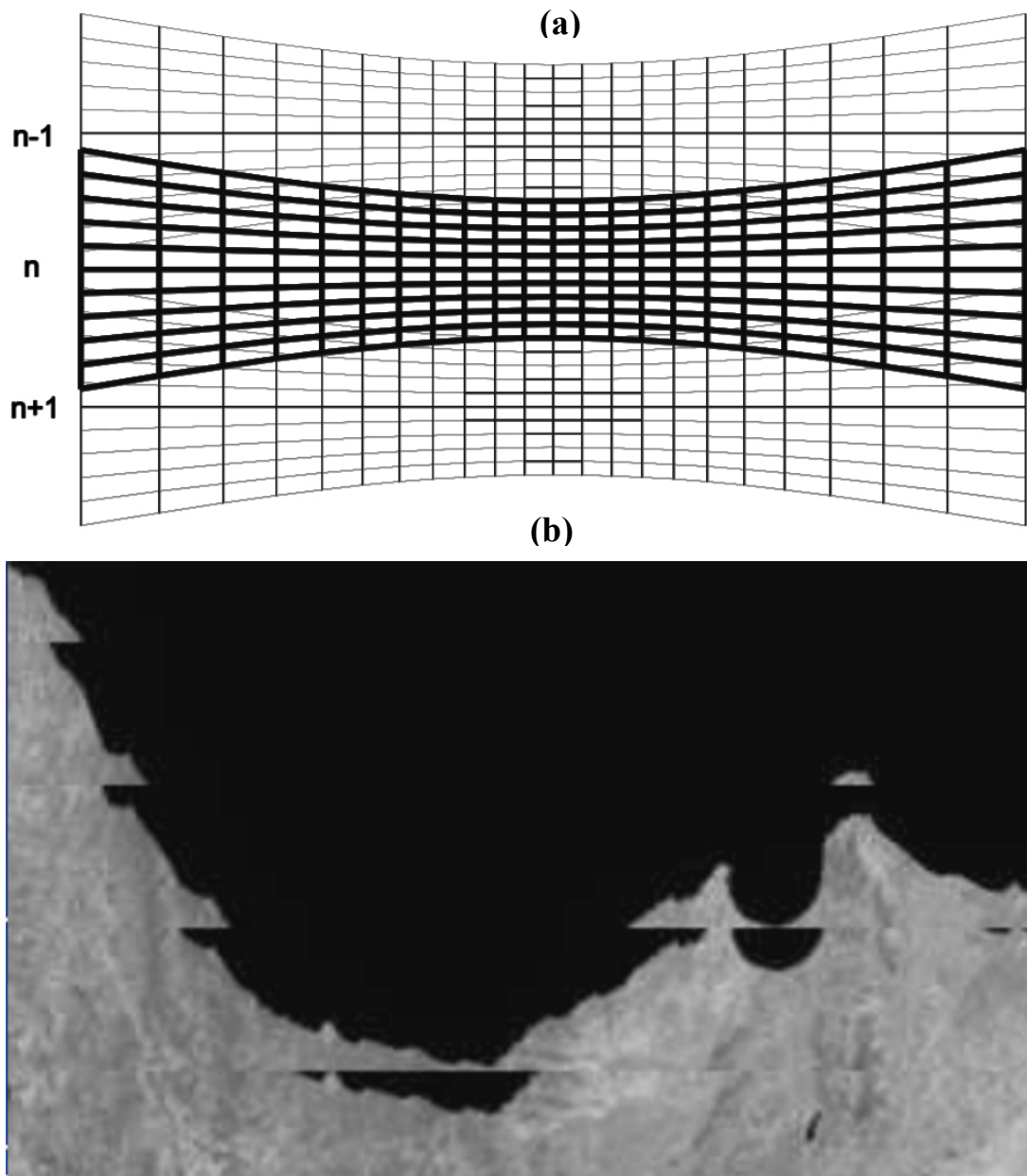


Figure 11. (a) Rectangular of array of data capture from MODIS satellite in bowtie shape.

(b) duplication of scenes due to scan line stack caused by bowtie-effect (Maier et al., 2004).

Once the duplicates were removed, the data was fitted onto a 2 x 2 km grid in order to match the resolution of other input data used in the model (Figures 12 and 13). For each grid cell, Terra/Day, Terra/Night, Aqua/Day, or Aqua/Night settings were selected based on which had the most fire detected; this value was then used for the day. Each daily total was then summed in order to get a monthly value per grid cell. Though the monthly value represents one overpass per day, the data is quantitatively representative of the diurnal burn pattern, but does provide statistically qualitative information. The fire data were then overlaid onto the land cover map using GIS to simulate which vegetated areas were likely affected by burning (Figure 14).

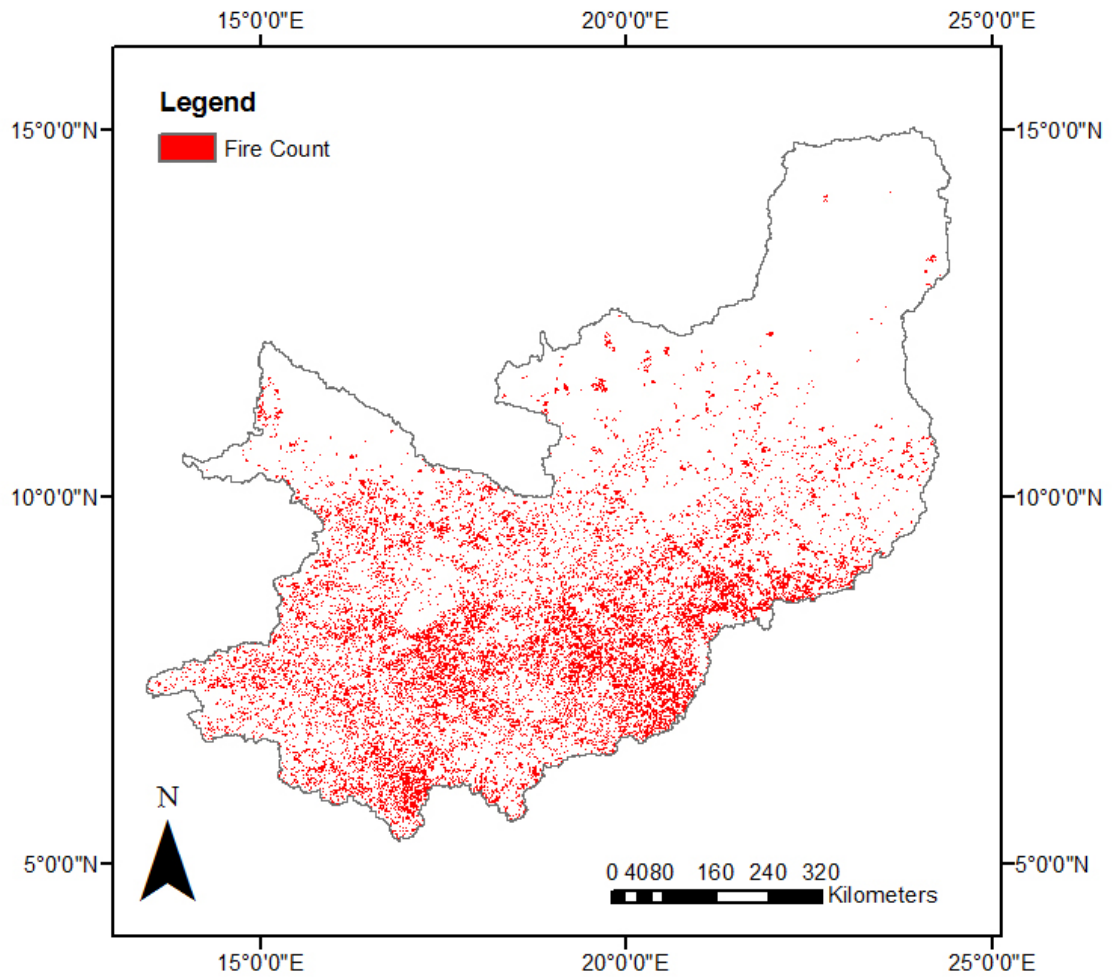


Figure 12. January 2010 fire counts from MOD14.

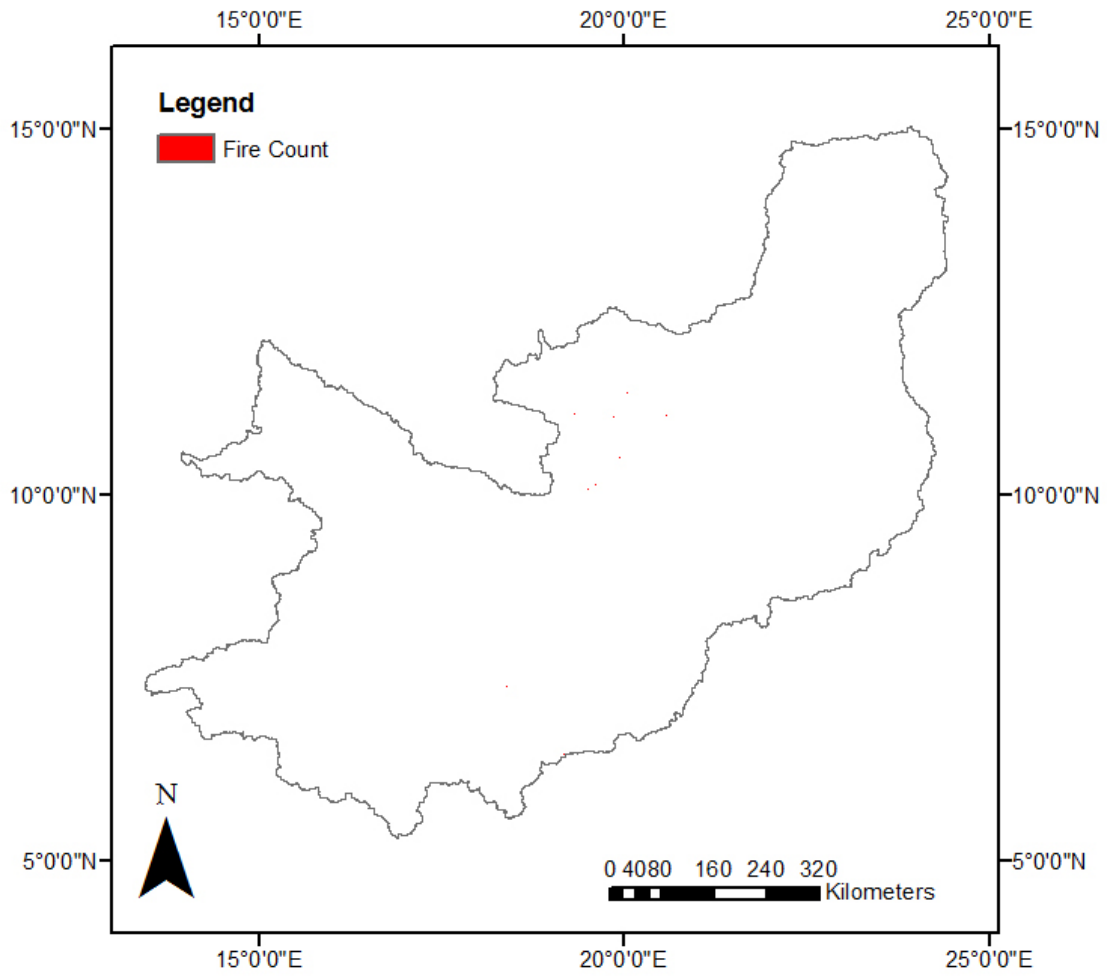


Figure 13. August 2010 fire counts from MOD14.

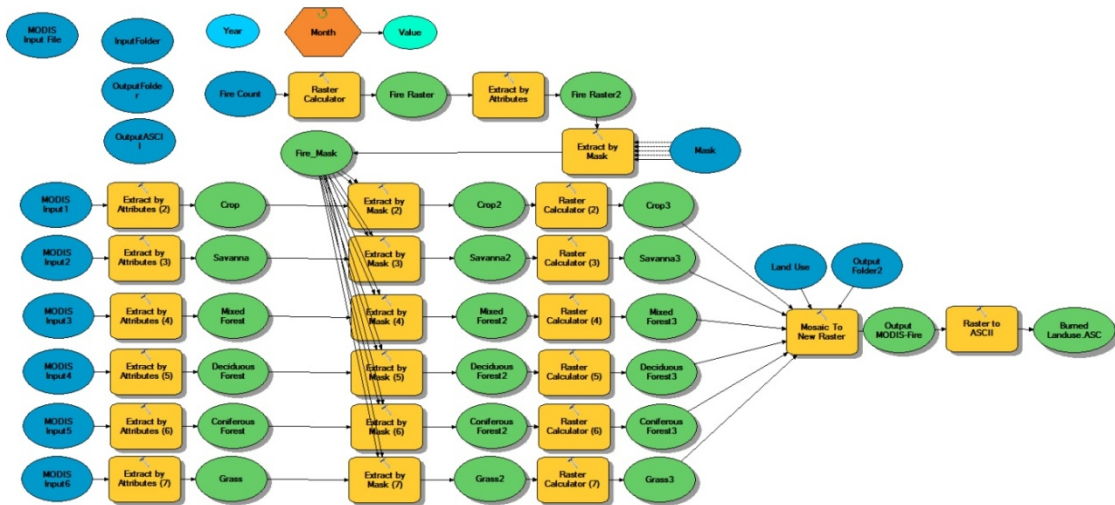


Figure 14. GIS model for creating land cover rasters considering burning for WetSpass-M input.

Since the land cover data were yearly and fire data were monthly, output land cover considering burning was calculated monthly. A GIS model was built, which first extracted the fire count for the desired month and then created a raster of only pixels detecting fire was created using the Raster Calculator tool. Specific land cover types were extracted from the previously created yearly land cover data used in the non-burning WetSpass-M model. The extracted land cover classes were: cropland, savanna, mixed forest, deciduous forest, coniferous forest, and grassland (Figure 15). Each land cover area was then used as a mask to extract only those areas which experienced burning. For example, a new raster for savanna was created only showing those areas in the savanna in which fire was detected for a particular month. Each of the newly created land cover rasters was then assigned a number corresponding to a WetSpass code used in the look-up table. The burned areas were merged with the other land cover types such as urban,

bare soil, etc. and new classes were assigned to vegetated areas shown as burned: burned coniferous, burned deciduous, burned mixed forest, burned savannah, and burned grassland (Figure 16). The land cover values were then used by WetSpass-M to assign land use parameters by means of a lookup table used in water balance calculation.

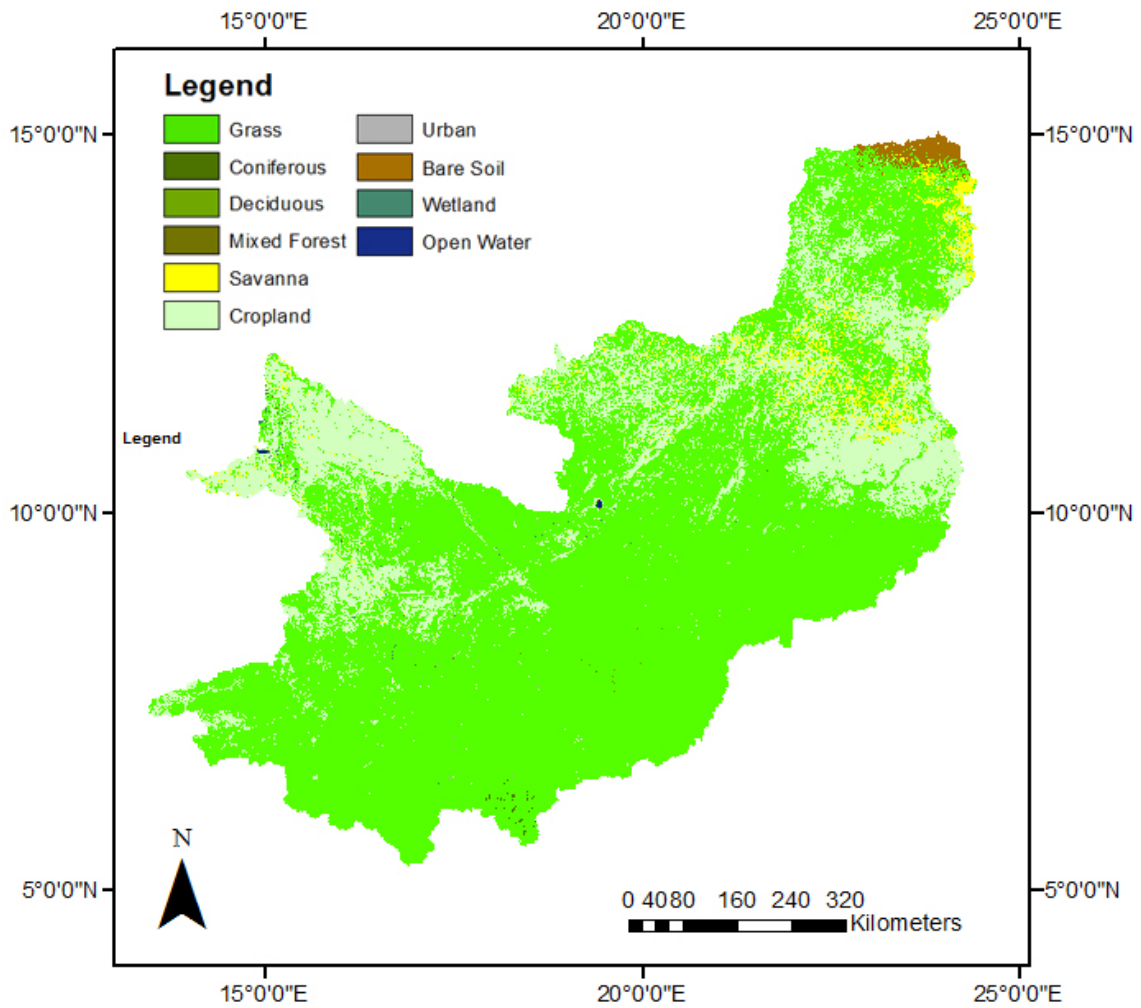


Figure 15. 2010 map showing WetSpass-M land use classifications derived from MODISMDC12Q1.

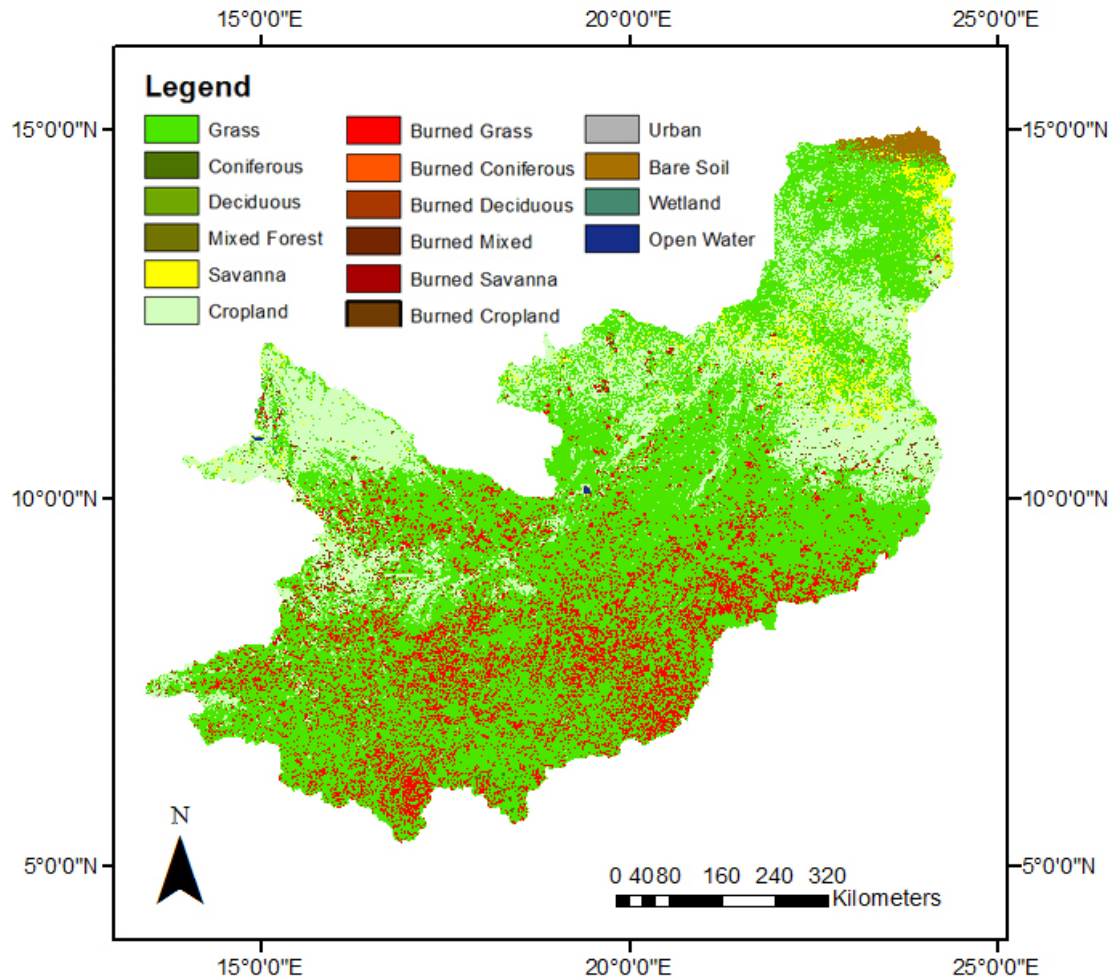


Figure 16. January 2010 map showing WetSpas-M land use classifications derived from MODIS MDC12Q1 and MOD14.

4.3.3 Land Cover Look-up Tables

For this study, additional land cover types were included in the land use look-up table to account for burning (Appendix A). For example, LAI (the quantity of leaf coverage compared to ground surface area) changes to the look-up table parameters were calculated using the same method employed by DeSales et al. (2015) with the modification of the equation:

$$VC = VC_u[1 - FBA \times (1 - SR)] \quad (3)$$

where VC is the burned vegetation cover, VC_u is the original (unburned) vegetation cover, FBA is the fractional burned area, and SR is the survival rate. Effected land cover parameters include LAI, vegetated area, burned area, impervious area, open water area, root depth, minimum stomata opening, vegetative height, Manning coefficient, land factor, and aerodynamic resistance. LAI is a quantity measuring the leaf area per unit of ground surface area. LAI modifies the amount of water from precipitation and heat fluxes, affecting ET and runoff. Minimum stomata opening refers to the minimum size of stomata for that land cover type. Stomata, which are the pores on leaves used for gas exchange, have been shown to change size with temperature depending on water availability (Schulze & Küppers, 1979). Burning also reduces vegetative height as land is cleared of vegetation, and thus increasing wind speed. Increased wind speed reduces sensible heat, increasing leaf temperature and stomatal resistance, thus increasing transpiration. Conversely, decreased vegetative height tends to decrease aerodynamic resistance, also known as drag. Aerodynamic resistance is calculated for the WetSpas-M table using:

$$r_a = \frac{1}{K^2 U_a Z_a} \left(\ln \left(\frac{Z_a - Z_d}{Z_0} \right) \right)^2 \quad (4)$$

where r_a is the aerodynamic resistance, K is the von Karman constant (0.41), U_a is the wind speed at elevation Z_a , Z_d is the zero displacement elevation, and Z_0 is the aerodynamic roughness height of surface (Abdollahi, 2015). Decreased aerodynamic resistance has the effect of decreasing ET (Li & Lawrence, 2018).

4.3.4 Land Use in the CLC

Analysis of land use model inputs for the CLC show the dominant classes to be grassland (74.88%), cropland (21.81%), and savanna (1.90%). Coniferous, deciduous, and mixed forest combined only make up 0.12%, with wetland covering 0.2%. Non-vegetative cover are open water (0.28%), urban build-up (0.18%), and bare soil (0.93%). Burning within the dominant land cover types show grassland to have the highest fire detection with an average of 5%-20% of grassland showing fire during the dry season. Grassland fires may be due to controlled burning or wildfires, but that they make up such a large portion of the catchment is significant. Peak burning appears to occur from November through January for all classes with little to no burning occurring May through July.

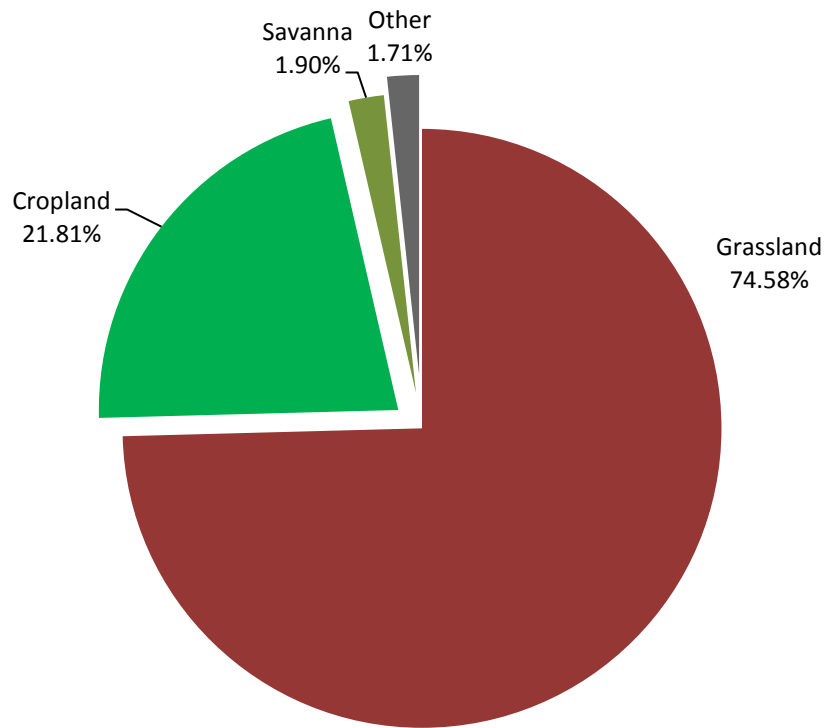


Figure 17. Distribution of land cover percentages in the Chari-Logone catchment. Grassland is by far the greatest land cover type followed by cropland. All other land cover types such as forest, bare soil, wetland, urban, and open water are combined into the category "other". Data source is MDC12Q1.

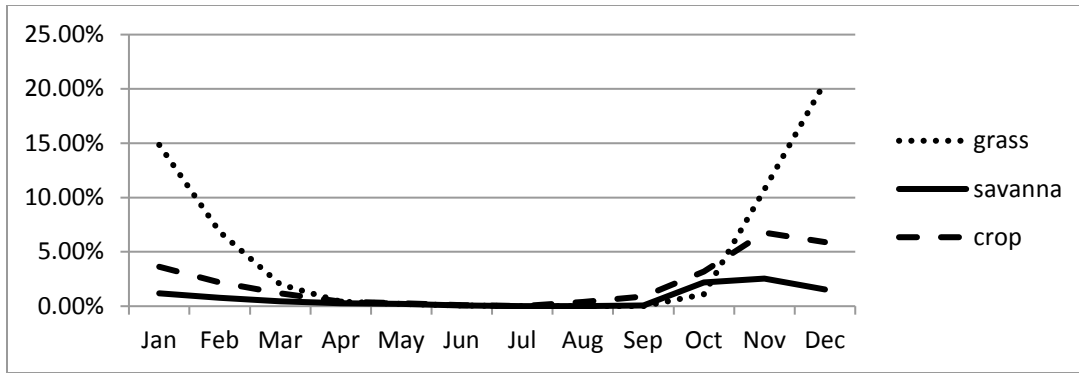


Figure 18. Average percent of monthly burning for major land cover types from 2003-2011 taken from MOD14.

4.4 Temperature

Temperature data was extracted from the MOD11C3 Version 5 monthly daytime CMG land-surface temperature product from MODIS Terra. MOD11C3 is derived from the MOD11C1 daily global product, taking daily clear sky land surface temperature values and averaging them for a month at 0.05 degree resolution (~5.56 km). Validation of MODIS land surface temperature has been well researched (Bosilovich, 2006; Coll, Wan, & Galve, 2009; Wan & Li, 2010). Hulley and Hook (2009) show the high degree of MOD11C1 accuracy in Africa by comparing the data to *in situ* measurements taken in Namibia, Botswana, and South Africa. MOD11C1 Version 5 showed a mere 1.93% combined mean temperature difference to ground measurements.

An ArcGIS model (Figure 19) was built to process the MOD11C3 data by first importing and extracting the LST_Day_CMGDay Land Surface Temperature layer from the NetCDF type file. The Raster Calculator tool then converted the temperature from degrees Kelvin to Celsius degrees. The land surface temperature raster was then extracted

for only the catchment and converted to ASCII format for use in WetSpass-M (Figure 20). Analysis of land surface temperature shows a decrease in temperature during the wet season due to the cooling effect of precipitation over land (Figure 22).

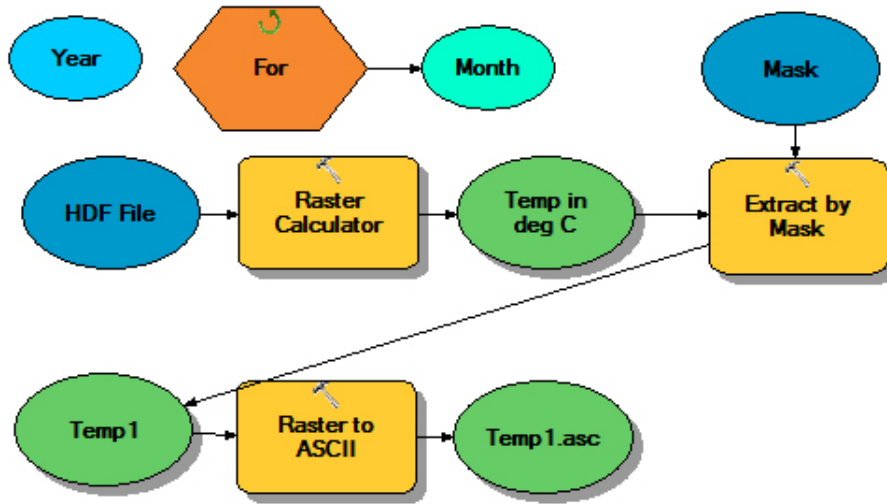


Figure 19. ArcGIS model used to process temperature raster inputs.

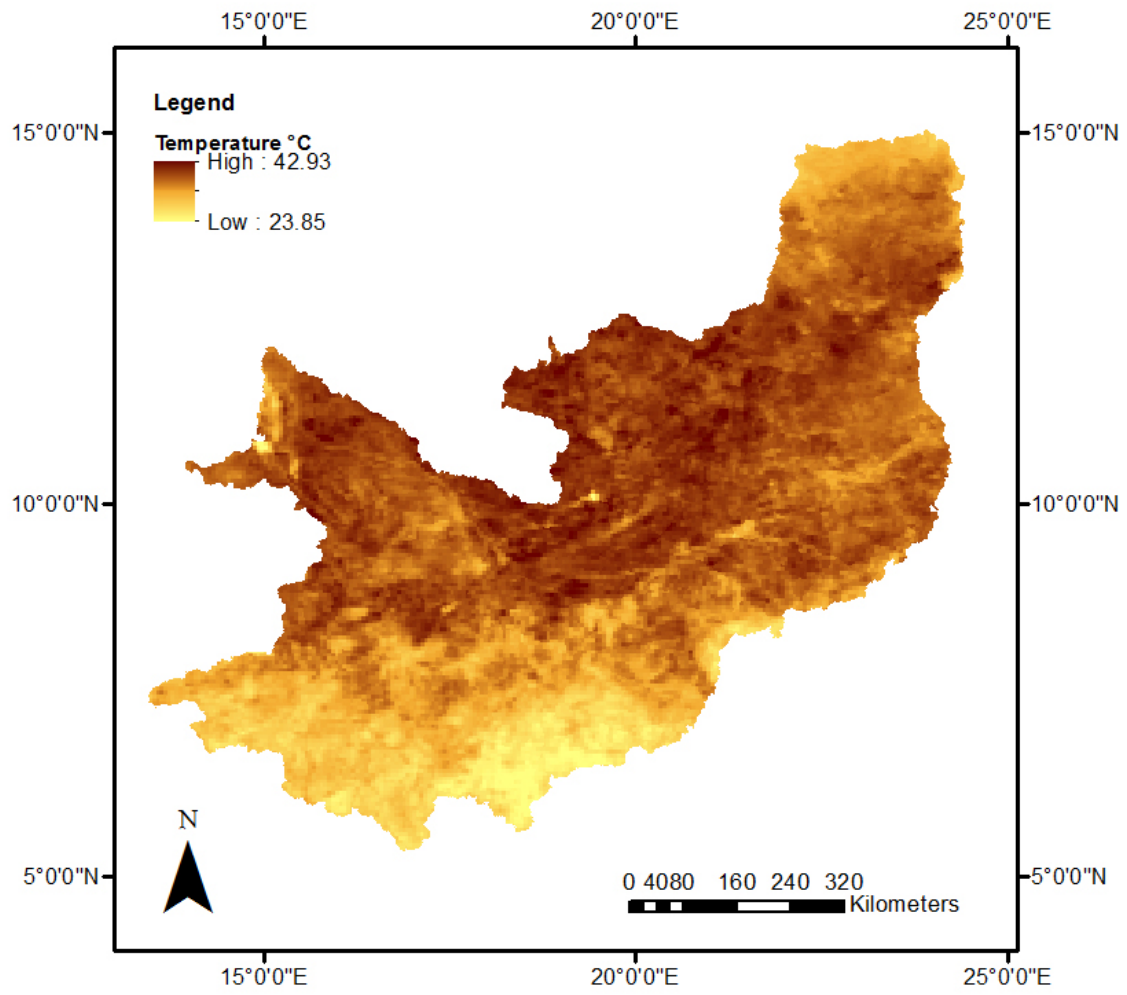


Figure 20. January 2010 land surface temperature model input.

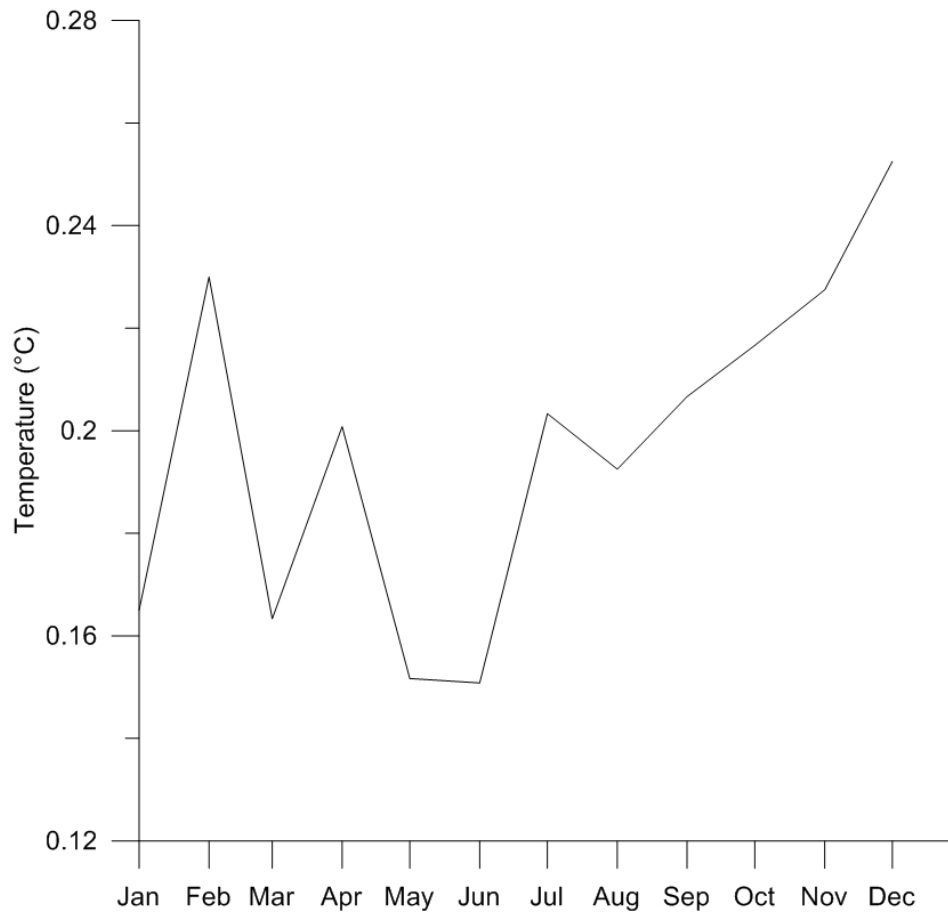


Figure 21. Monthly temperature anomalies from 2003-2011 averages.

4.5 Wind Speed

Currently there are not wind speed measurements or products available directly from satellites. Global climate models, such as the Global Forecast System (GFS) or Modern-Era Retrospective analysis for Research and Applications (MERRA), have the capability to calculate wind speed at various atmospheric layers. Unfortunately, GFS has a relatively low resolution of 28 km, which is far too coarse for this study. Custom climate models such as a Weather Research and Forecasting (WRF) model could be built for the study area. However, this was beyond the scope of the study and, even then, such models

have difficulty accounting for the complex terrain when calculating near surface winds at a desired resolution (Engelstaedter & Washington, 2014; Mughal et al., 2017).

For these reasons, station data were used for wind speed despite issues with data continuity. NOAA does not provide monthly wind speed averages, so daily records from NCEI Global Summaries of the Day were used and averaged monthly (Appendix B). The average wind speed values were also converted from 0.1 knots to m/s. The records contained station identifier and wind speed, but did not contain the stations geographic coordinates. To associate the station number with the correct geographic coordinates, a Python program was developed (Appendix C). Once the wind speed data was averaged, it was imported into ArcGIS as a shapefile and converted to a raster using kriging (Figure 22). The data was then processed and converted into the proper format for input into WetSpass-M.

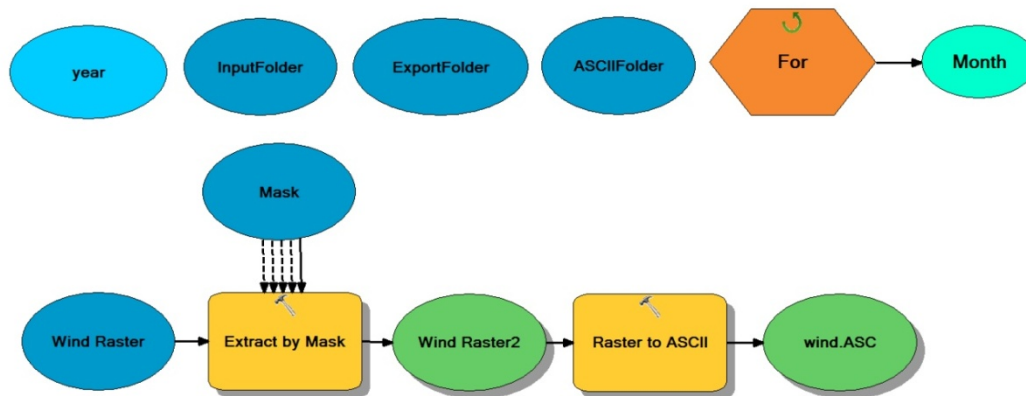


Figure 22. ArcGIS model used to process monthly averaged winds from NOAA NCEI climate stations.

4.6 PET

Another important input into the model is PET as it is the maximum evaporation and transpiration that could occur assuming sufficient water. As noted earlier, burning has a significant impact on surface albedo change. This change in albedo affects the energy balance and therefore should not be overlooked when calculating PET. Two PET datasets were created for use for the two WetSpass-M models. Albedo values considering burned and non-burned vegetative classes were derived from Gatebe et al. (2014) and those of non-vegetative areas are taken from Yu and Lu (2014) (Appendices D & E). The spatial distribution of albedo was assigned using the modified MDC12Q1 (Type1) yearly land cover data showing burned areas.

To consider the effect of albedo change on PET, a simplified penman equation was used following the method outlined by Valiantzas(2006):

$$E_{PEN} \approx 0.051(1 - \alpha)R_S\sqrt{T + 9.5} - 2.4\left(\frac{R_S}{R_A}\right)^2 + 0.052(T + 20)\left(1 - \frac{RH}{100}\right)(a_u - 0.38 + 0.54u) \quad (5)$$

where E_{PEN} is the Penman potential evapotranspiration, α is the albedo, R_s is the solar radiation, T is the surface temperature, R_a is the extraterrestrial radiation, RH is the relative humidity, a_u is a wind function coefficient of 1, and u is the wind speed. The wind coefficient of 1, was used originally used by Penman (1963). Since no solar radiation is available from regional station data, it is estimated from measured sunshine hours using the equation:

$$R_S = R_A \times \left(0.5 + 0.25 \times \frac{n}{N}\right) \quad (6)$$

where R_s is the solar radiation, R_a is the extraterrestrial radiation, n is the measured bright sunshine hours per day, and N is the maximum possible duration of daylight which is derived from the latitude of the site and the number of Julian months are given (Shuttleworth, 1993; Allen, Smith, Pereira, & Perrier, 1994). R_a is calculated using:

$$R_A = 37.59d_r[\omega_s \sin(\phi) \sin(\delta) + \sin(\omega_s)\cos(\phi)\cos(\delta)] \quad (7)$$

where d_r is the relative distance between the sun and the earth, ϕ is the radians, and δ is the solar declination. Maximum possible duration of daylight is calculated using the equation:

$$N = \frac{24}{\pi} \omega_s \quad (8)$$

where ω_s is the sunset hour angle in radians and $\omega_s = \arccos(-\tan(\phi) \tan(\delta))$, where δ is the solar declination. The variable δ is determined using:

$$\delta = 0.409 \sin\left(\left(\frac{2\pi}{365}\right)J - 1.39\right) \quad (9)$$

where J is the Julian day corresponding to the respective month (Shuttleworth, 1993; Allen et al., 1994). Relative humidity was calculated using the equation:

$$RH = 100 \left(\frac{e_a}{e^\circ(T)} \right) \quad (10)$$

where $e^\circ(T)$ is the saturation vapor pressure (kPa) and e_a is the actual vapor pressure.

Climate station data from NCEI Global Summaries of the Month were used to calculate solar radiation, extraterrestrial radiation, and relative humidity and these values were used to create raster datasets in ArcGIS (Appendix F). The data were imported into GIS and a model was used to calculate the two PET datasets and export them for use as WetSpas-M inputs (Figure 22).

PET was validated by comparing the calculated PET to Consultative Group for International Agricultural Research (CGIAR-CSI) PET, which averages PET

observations from 1950 - 2000 (Zomer et al., 2007; Zomer, Trabucco, Bossio, van Straaten, & Verchot, 2008). Calculated PET with albedo compared very well against the CGIAR PET and was used (Figures 24, 25, 26, & 27).

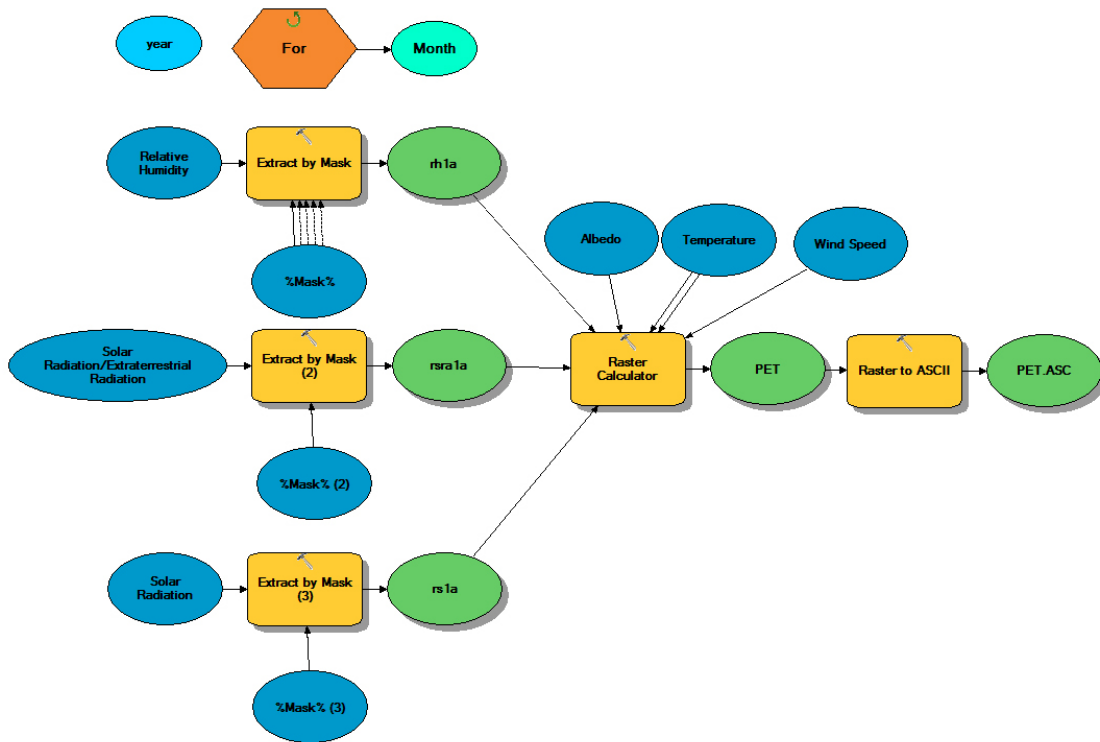


Figure 23. ArcGIS model used to create PET considering burning and non-burning scenarios for WetSpas-M input.

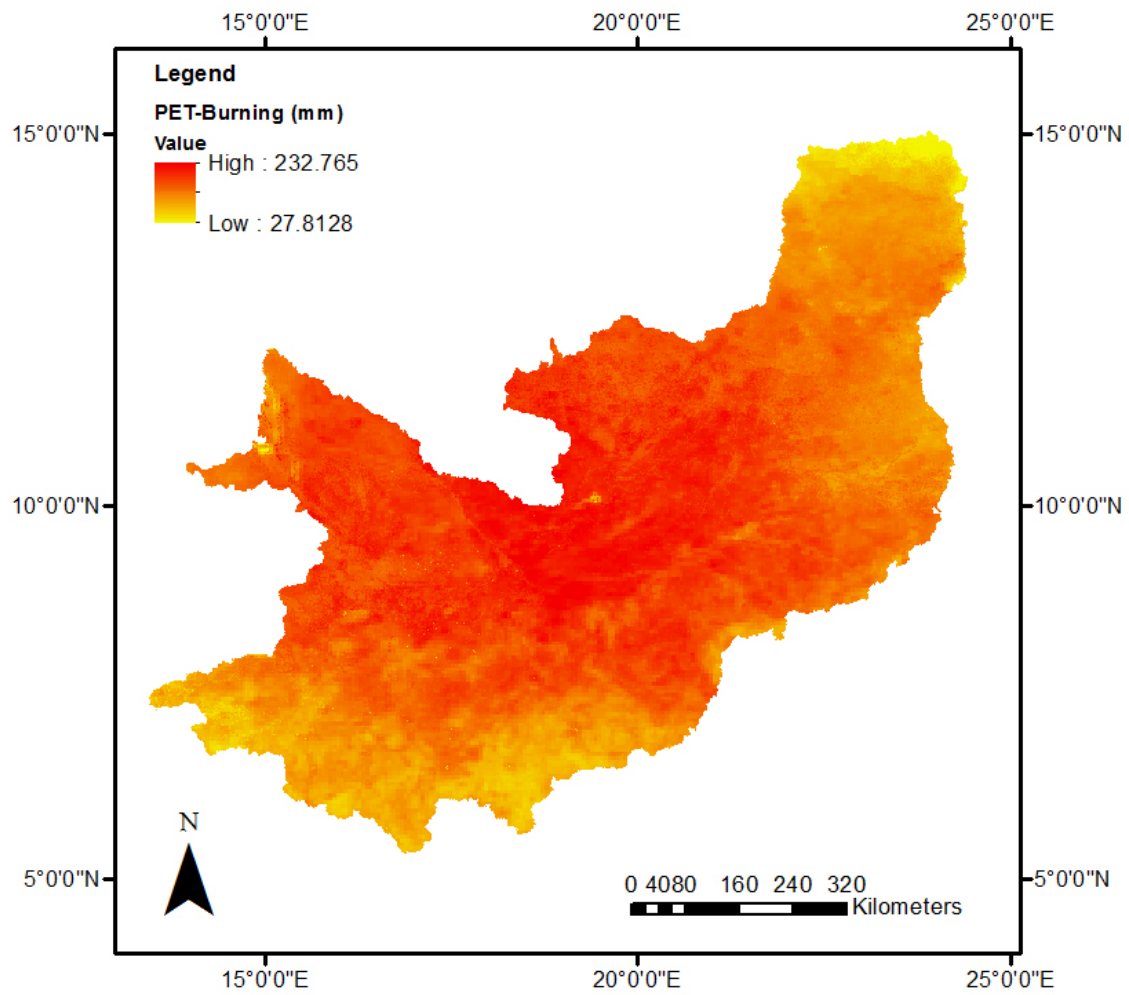


Figure 24. PET considering burning for January 2010.

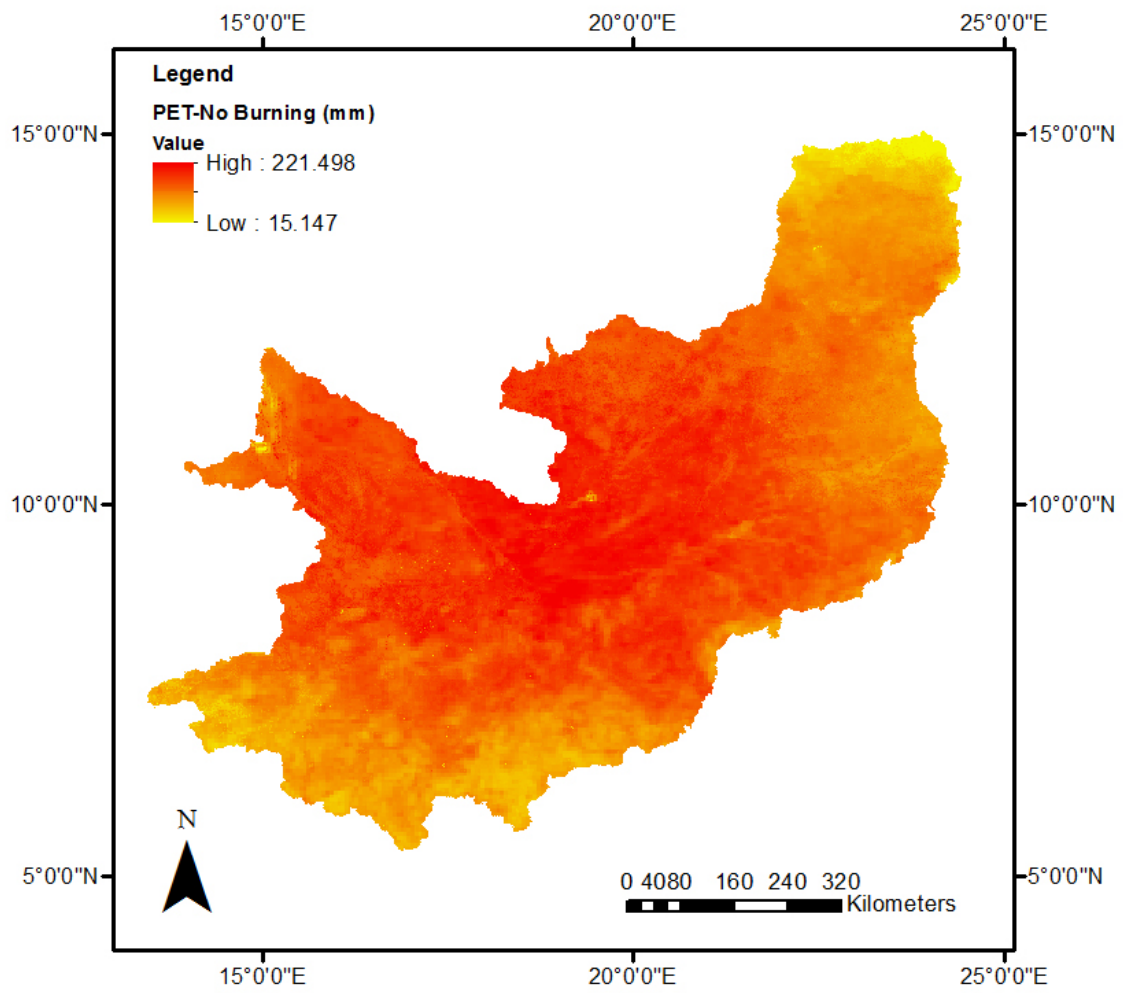


Figure 25. PET not considering burning for January 2010.

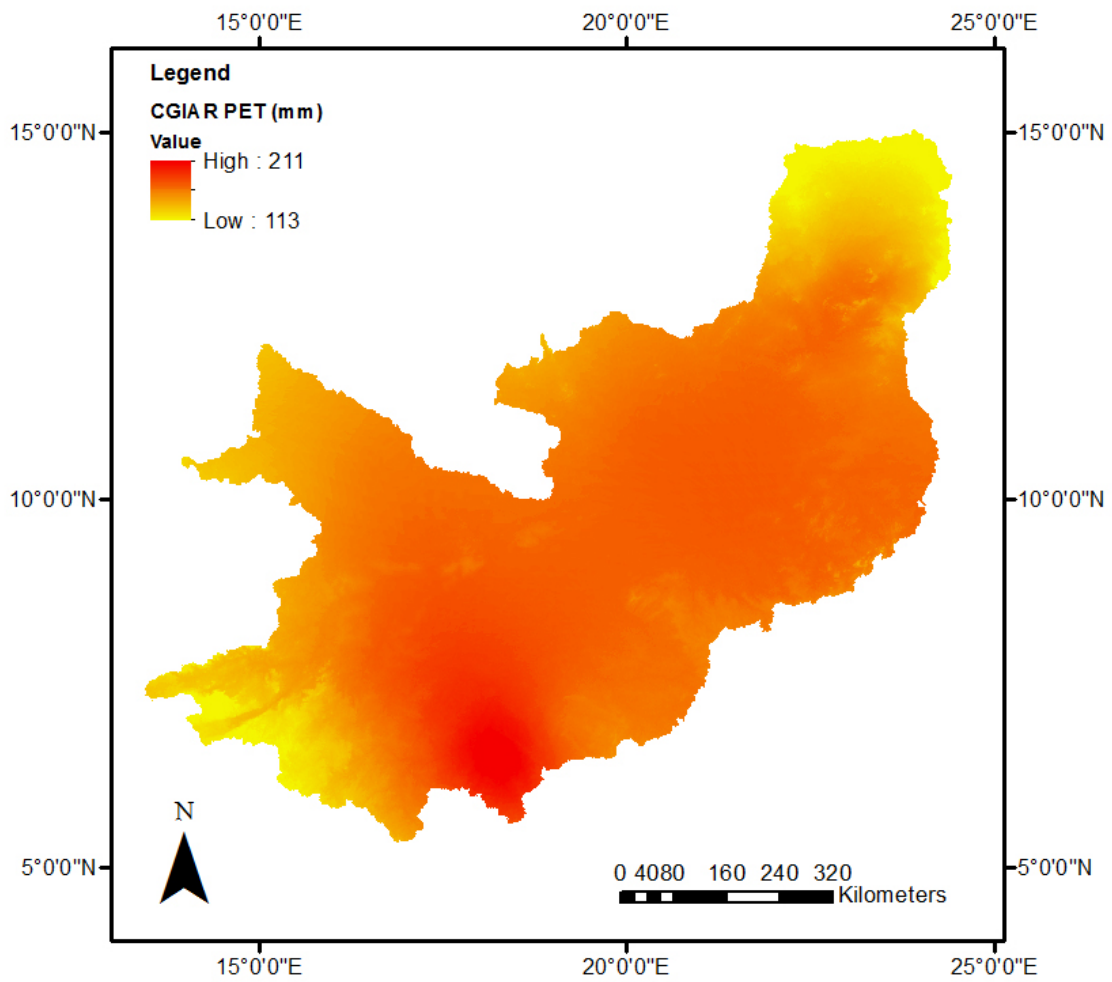


Figure 26. CGIAR 1950 - 2000 monthly averaged PET for January.

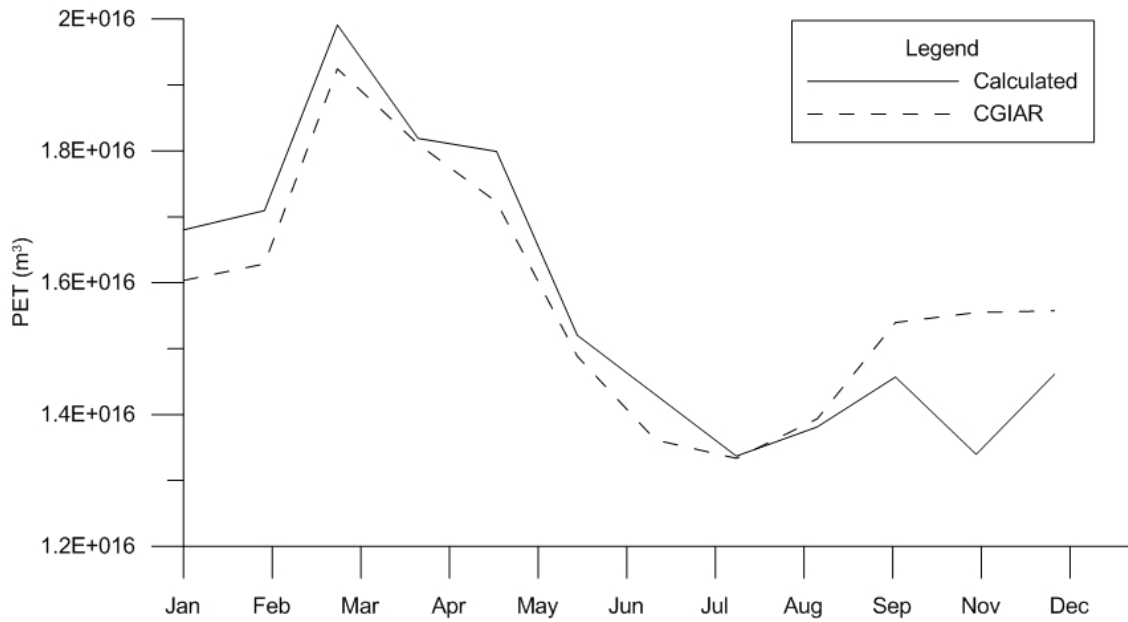


Figure 27. Comparison of averaged PET by month, plotting the modified Penman equation against CGIAR data.

4.7 Elevation

Elevation from a digital elevation model (DEM) was provided by the Shuttle Radar Topography Mission (SRTM). The Shuttle Radar Topography Mission (SRTM) is an international project coordinated by the National Imagery and Mapping Agency (NIMA) and NASA (van Zyl, 2001). The primary objective of the mission was the acquisition a complete high-resolution digital topographic database of the Earth. SRTM flew onboard the Space Shuttle Endeavour consisted of a specially modified radar system and had an 11-day mission in February of 2000. The digital topographic map products were designed to meet Interferometric Terrain Height Data (ITHD) specifications: with 30 m x 30 m spatial sampling and absolute vertical height accuracy (90% linear error) of 16 m. The absolute horizontal accuracy (90% circular error) is 20 m. The SRTM resolution used in

this study is 90 m x 90 m (Sun, Ranson, Kharuk, & Kovacs., 2003) (Figure 29). Slope was calculated using the elevation input by the WetSpass-M program.

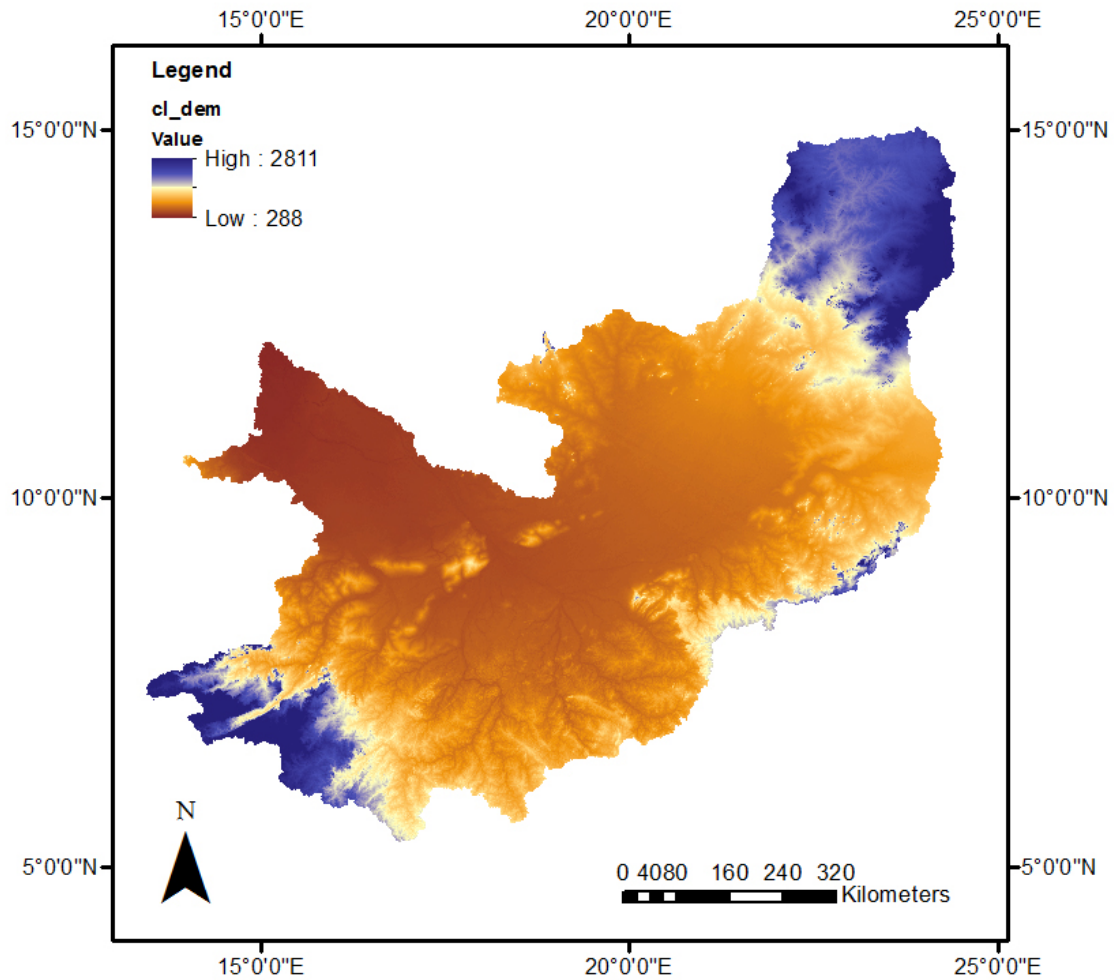


Figure 28. Chari-Logone elevation from SRTM DEM.

4.8 Groundwater

A groundwater raster dataset was generated using 2009 measurements taken from a collaborative study in the Lake Chad Basin by the University of Missouri, Kansas City and NASA Goddard Space Flight Center and BGR (2010). The data were imported into

ArcGIS and converted to shapefile points and converted to raster using kriging. This same data was used by Babamaji (2013) (Figure 30).

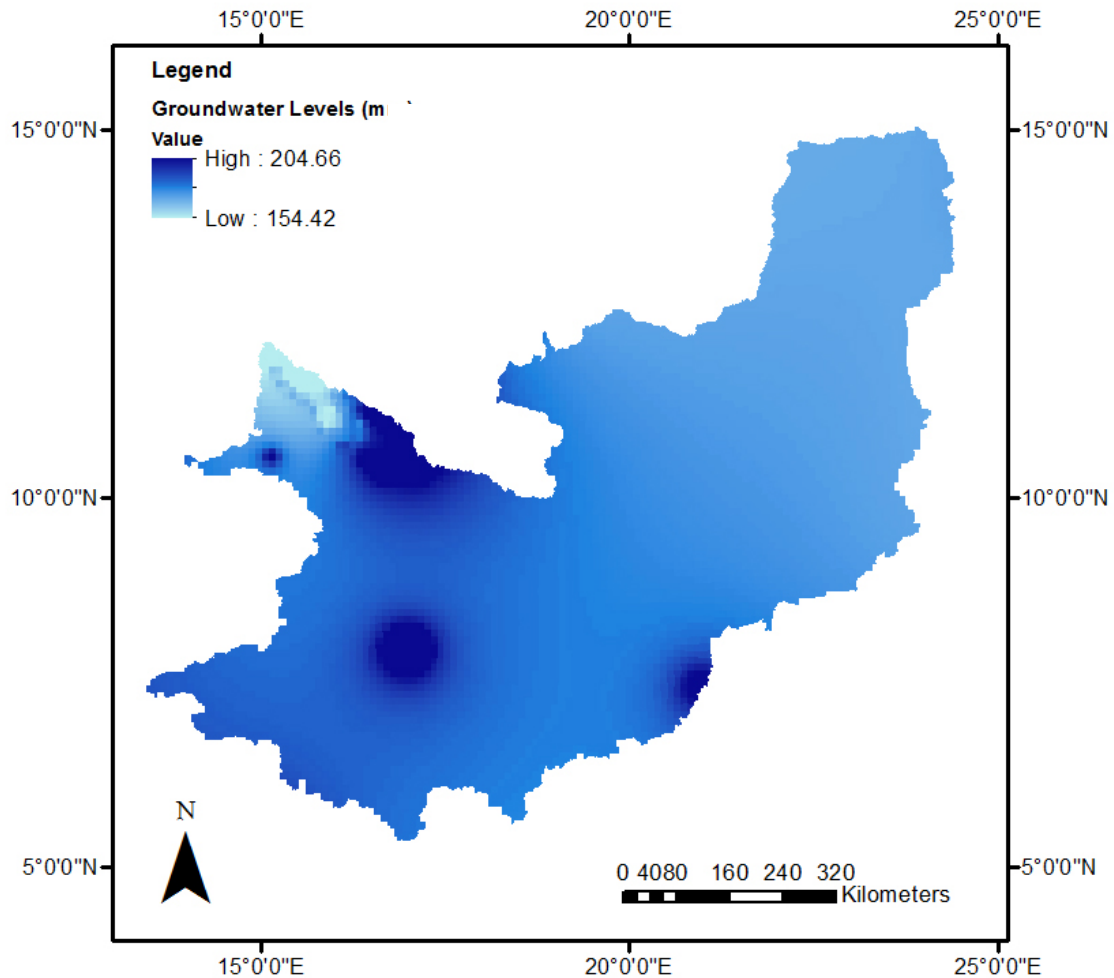


Figure 30. Map of groundwater levels used for input into GIS.

4.9 Processing Results

A tool was developed (Appendix G) to convert the WetSpass-M outputs from ASCII format into GeoTIFF rasters. An ArcGIS model was created to extract the WetSpass-M outputs by land use type. It was desired to convert the WetSpass-M outputs from millimeters into cubic meters. Currently, no tool exists in ArcGIS to calculate raster

summations into a table format. Therefore, a program was written which summed each output raster, organized it by class and water balance parameter, and exported it into a text document for analysis (Appendix H).

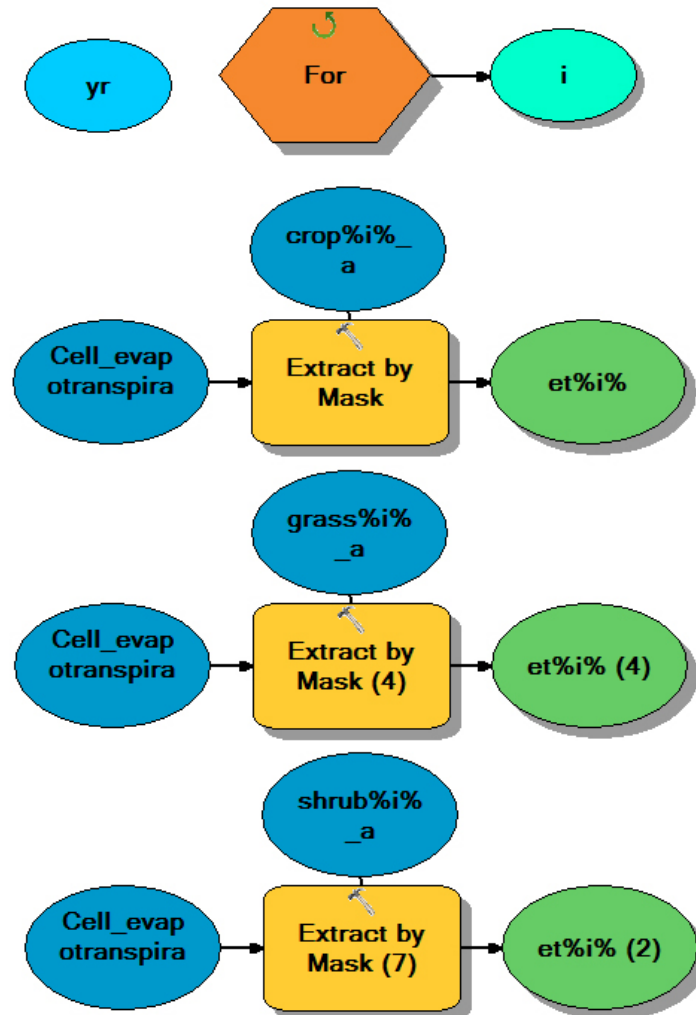


Figure 31. GIS model for extracting WetSpass-M outputs by vegetative class.

4.10 Groundwater Model

A groundwater model was created to study how outputs from the WetSpass-M ET parameter affected changes in groundwater level. If results were favorable, study of

groundwater interactions with Lake Chad could be performed to see how groundwater flux considering burning affects correlates with lake level change. Additionally, if a model could be developed that predicted monthly groundwater levels, this could be used to mitigate sanitation issues in shallow water wells, especially in Cameroon.

4.10.1 Need for Groundwater Prediction

Inadequate waste treatment leaching into uppermost aquifer have caused serious problems in the poor and rural areas of Cameroon and has been linked to outbreaks of cholera. The worst outbreak since 1971 occurred from 2009 to 2011. The cases were first reported in the Extrême Nord region of Cameroon near Lake Chad. The cholera fatality rate (CFR) was 13% and more than 60% of those deaths occurred in the community. The epidemic spread to the neighboring country of Nigeria in the Adamawa, Borno, and Taraba states. The cholera outbreak continued to spread in the affected areas of Extrême Nord and Nord where less than 25% of the population have access to potable water and less than 5% of the population use latrines. At the end of 2011, 9 out of 10 regions in Cameroon reported 22,762 cholera cases with 786 deaths (Figure 32). The issue was so severe that a transborder meeting between the countries of Niger, Nigeria, Chad, and Cameroon took place with the aim to coordinate cholera containment and prevention across borders (WHO, 2012).

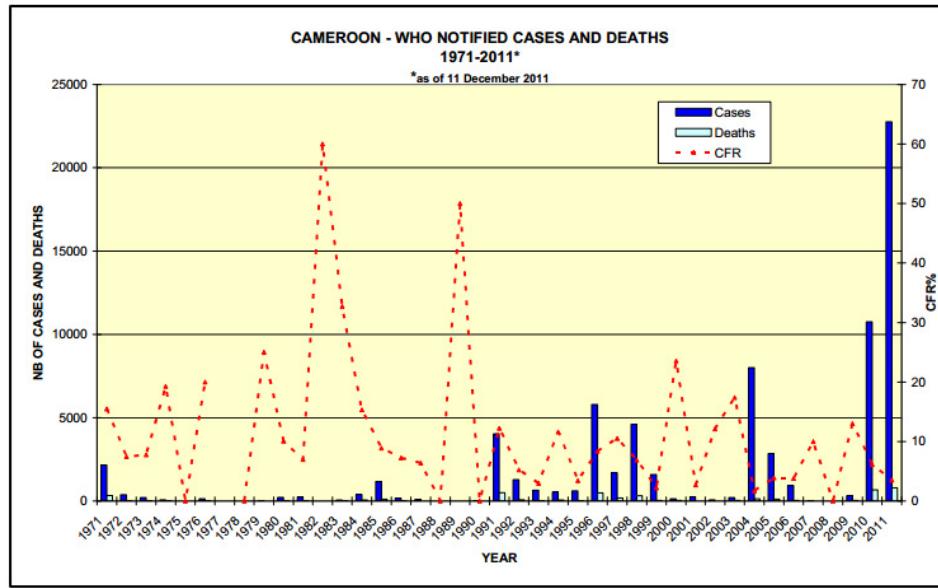


Figure 32. Cholera cases, deaths, and cholera fatality rate (CFR) from 1971-2011 (WHO, 2012).

4.10.2 Study Area Geology

The geology of the Chari-Logone Catchment has high variability with portions from the Precambrian, Silurian, Devonian, Cretaceous, Pleistocene, Tertiary, and Quaternary periods (Figures 33 & 34). The Graben region, where the Logone and Chari Rivers converge, feature continental Cretaceous sands and red to grey clays. The Continental Terminal portion of Graben stratigraphy is composed of Paleogene formations with sandy clays, clayey sandstones, and heterogeneous sandy sediments. Deposits of sand, clayey lacustrine material, and intercalated sand comprise the Pliocene section. Pliocene clays are covered by Pleistocene clays, diatomites, sandstone, and sand. The large amounts of Quaternary deposits are comprised of kaolinite or neo-formation clays, fluvio lacustrine, aeolian, and fluvio-deltaic material. The basement rock is

comprised of gneiss and granitic material (Candela, Elorza, Tamoh, Jiménez-Martínez, & Aureli, 2014).

The catchment contains three major aquifers. The uppermost, and the one most utilized for groundwater use, is located in the Quaternary deposits. The Quaternary aquifer is unconfined and many of the hand dug wells are for drinking water and domestic use. The second aquifer at a depth of 150 and 400 m is confined and comprised of Pliocene deposits. The deepest aquifer located in Continental Terminal material and is largely unexplored due to a depth of over 700 m (Kindler, Warshall, Arnould, Hutchinson, & Varady., 1990).

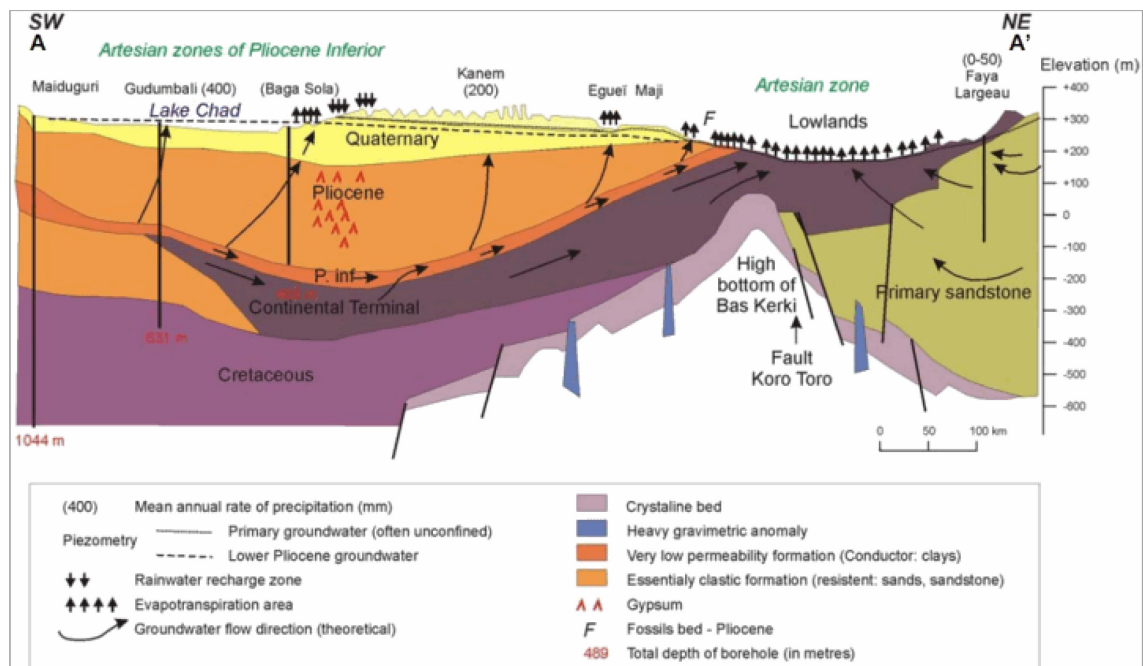


Figure 33. Cross-section of Lake Chad Basin geology (Schneider, 1991).

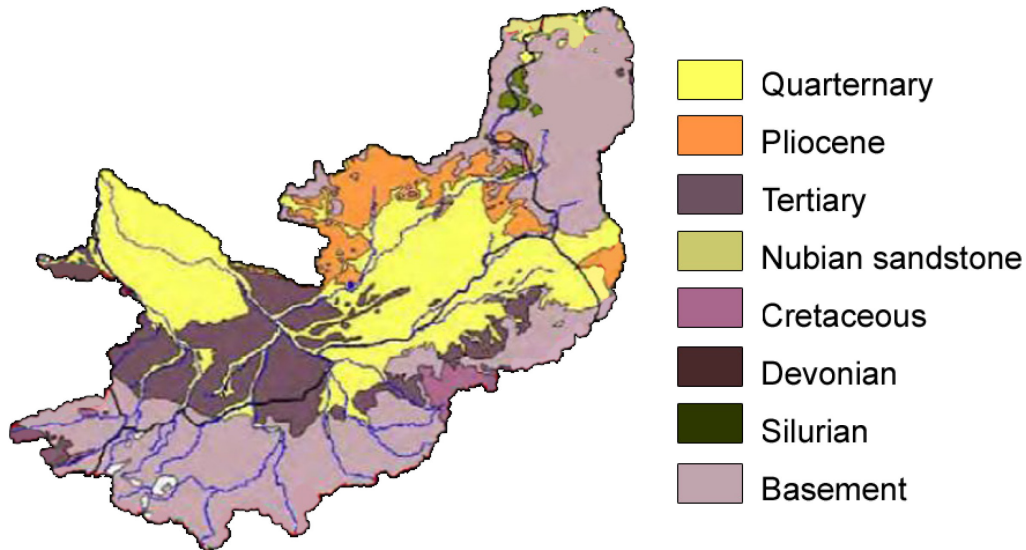
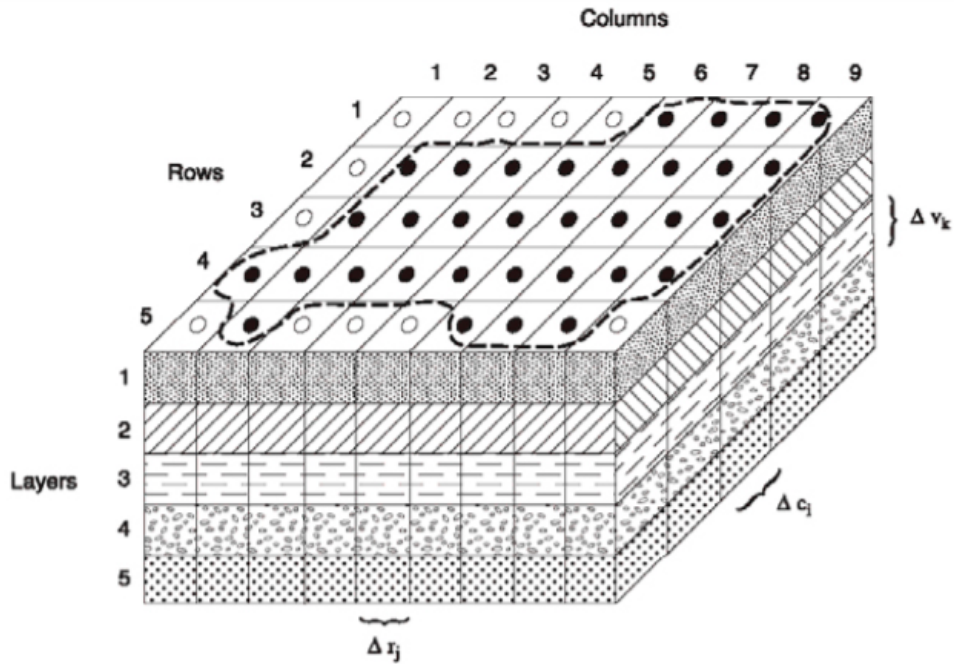


Figure 34. Geology of Chari-Logone Catchment. Based on BGR (2010).

4.10.3 Processing MODFLOW Description

The model was developed using Processing MODFLOW (PMWIN), which is a simulation software designed to simulate groundwater flow and transport processes using the U.S. Geological Survey's (USGS) three-dimensional finite difference groundwater model, MODFLOW. In MODFLOW, the aquifer may be converted to a three-dimensional grid made up of cells. The cells are stacked in three dimensions: horizontally, laterally, and vertically. Within each cell a "node", a point at which head (groundwater level) is to be calculated. Due to the complex nature of modeling groundwater through porous earth material, many parameters such as hydraulic conductivity, potentiometric head, volumetric flux, specific storage, and time, need to be considered. Finite difference models allow for faster computation of the partial

differential equations necessary to take these parameters into consideration (Harbaugh, 2005).



EXPLANATION

- AQUIFER BOUNDARY
- ACTIVE CELL
- INACTIVE CELL
- Δr_j DIMENSION OF CELL ALONG THE ROW DIRECTION—
Subscript (j) indicates the number of the column
- Δc_l DIMENSION OF CELL ALONG THE COLUMN DIRECTION—
Subscript (l) indicates the number of the row
- Δv_k DIMENSION OF CELL ALONG THE VERTICAL DIRECTION—
Subscript (k) indicates the number of the layer

Figure 35. Schematic of a finite difference grid based on. Note the nodes in the center of each cell (Harbaugh, 2005).

4.10.4 Groundwater Model Parameters

The model considered only the uppermost Quaternary aquifer since there was insufficient data available to consider the lower two aquifers. A 64 x 64 km grid was created with a pixel resolution of 23.8 x 23.8 km (Figure 36). The large cell size was due to computational constraints of PMWIN.

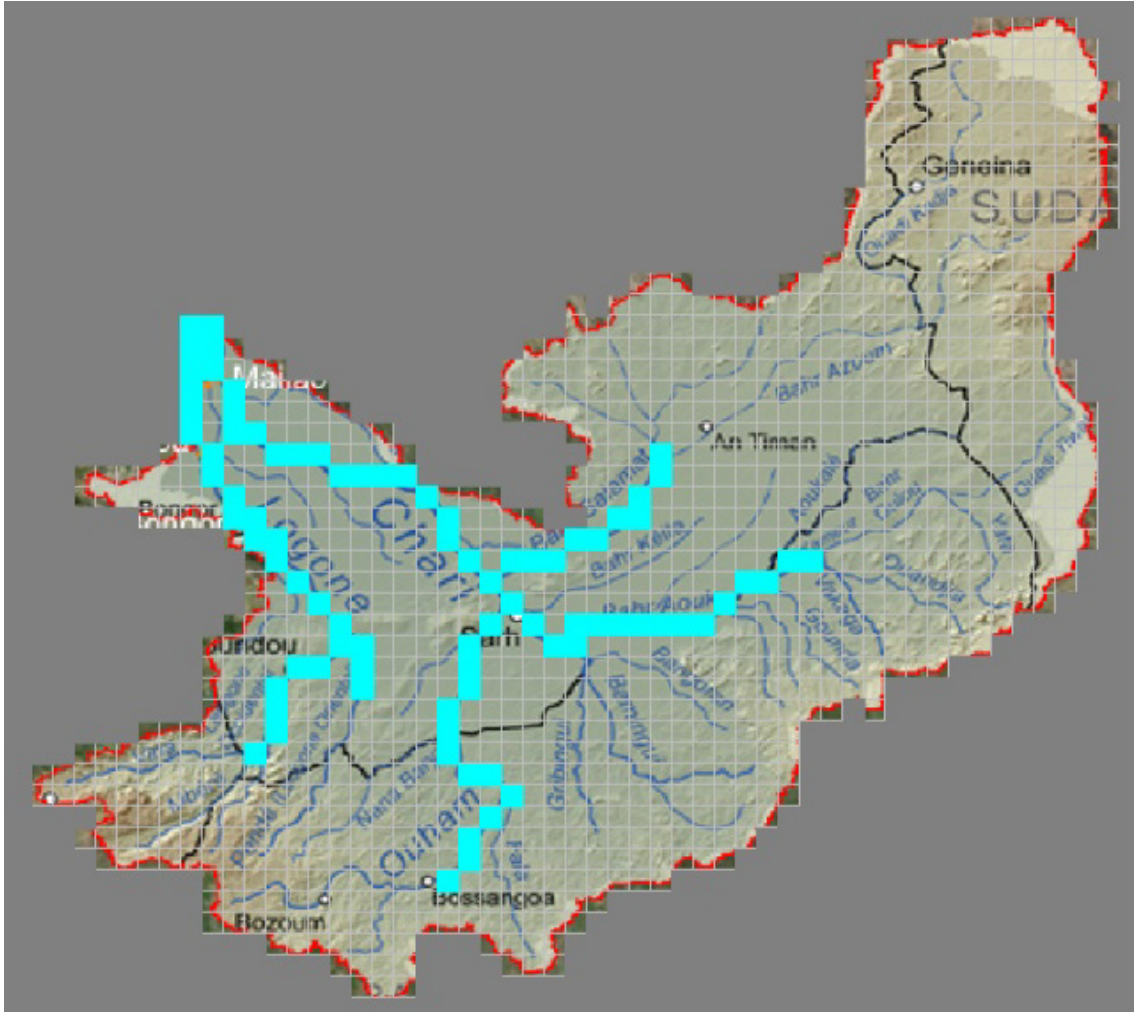


Figure 36. Groundwater Model Grid in PMWIN.

The top of the layer of the model, designating the ground surface, was interpolated from SRTM DEM data which was processed using GIS, resampling the data

and converting the image to shapefile points, and exporting the attribute table to excel. The data was then imported into PMWIN, where the points were interpolated using kriging and a Gaussian semivariogram. The bottom of the layers was calculated by subtracting 50 m from each cell of the top layer of the model since the average aquifer thickness is 50 m. The unit of time used in the model was days. Initial hydraulic heads were interpolated from a digitized map from BGR (2010) (Figure 37). Initial hydraulic heads are the height of the water table during model initialization. Since the map extent only covered the northwestern portion of the catchment where the Chari and Logone rivers converge, all other heads were assumed to be the elevation minus 20 m, as 20 m is the average recorded depth to groundwater for the basin. Hydraulic conductivity and transmissivity was interpolated from Candella et al. (2014). Hydraulic conductivity is a measure of how easily flow moves through a porous medium. Gravel, for example, will have larger conductivity values than clay due to the greater porosity of gravel. Transmissivity is similar to hydraulic conductivity, except it applies to the transmission of water across an aquifer's vertical thickness. Effective porosity, the ratio of the total connected space between sediment to the total amount of sediment, was assumed to be 0.33.

River discharge was simulated using the PMWIN river package. River properties for the Chari and Logone Rivers, such as depth and width, from station data were used (BGR, 2013) (Appendix I). Hydraulic conductance of the riverbed was calculated using:

$$C_{RIV} = \frac{K \times L \times W}{M} \quad (11)$$

where K is the hydraulic conductivity (m^2/day), L is the length of the river within a cell, W is the river width, and M is the riverbed thickness. River gradient was calculated using:

$$i = \frac{h_2 - h_1}{\Delta L} \quad (12)$$

where h_1 is the upriver head, h_2 is the downriver head, and ΔL is the river length in a cell. Recharge is interpolated from monthly WetSpas-M outputs (Schwartz & Zhang, 2003). Once a forward model was run, calibration was performed using inverse modeling. Forward modeling takes parameters and calculates hydraulic head. Reverse modeling takes the hydraulic head of the model and calculates certain parameters. The PEST inverse modeling package was used by utilizing variant effective porosity according to basin geology. 1000 iterations were performed to find the effective porosity values that most closely fit observed hydraulic heads. The hydraulic head values were taken from a map of the northwest catchment (LCBC, 1966). The heads were then digitized in GIS and imported into PMWIN.

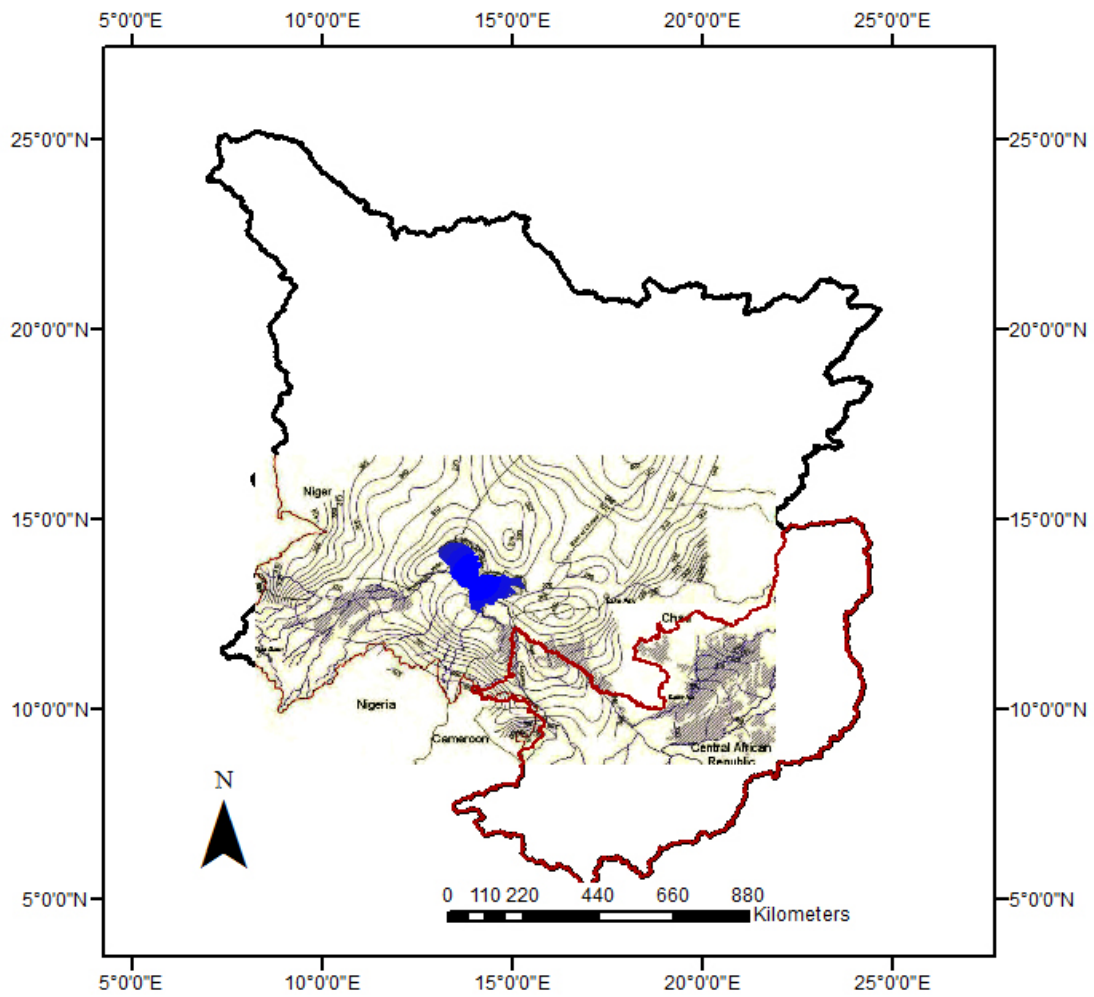


Figure 37. Hydraulic head map (LCBC, 1966) used in study overlaid on map of Chari-Logone Catchment and Lake Chad Basin areas.

CHAPTER 5

RESULTS

5.1 Water Balance Model Validation

Logone River discharge measurements acquired at the Bongor Station (Figure 37) during 2003 to 2007 (Seeber, 2013) were compared to runoff outputs from Wetspass-M. This was done by extracting only the runoff in the basin area discharging to Bongor Station. Flow direction of the CLC was calculated from the DEM and a mask of the flow leading to the station creating a mask by selecting sub-basins of the CLC. These sub-basins were used to create a mask for the WetSpas-M runoff (Figure 38).

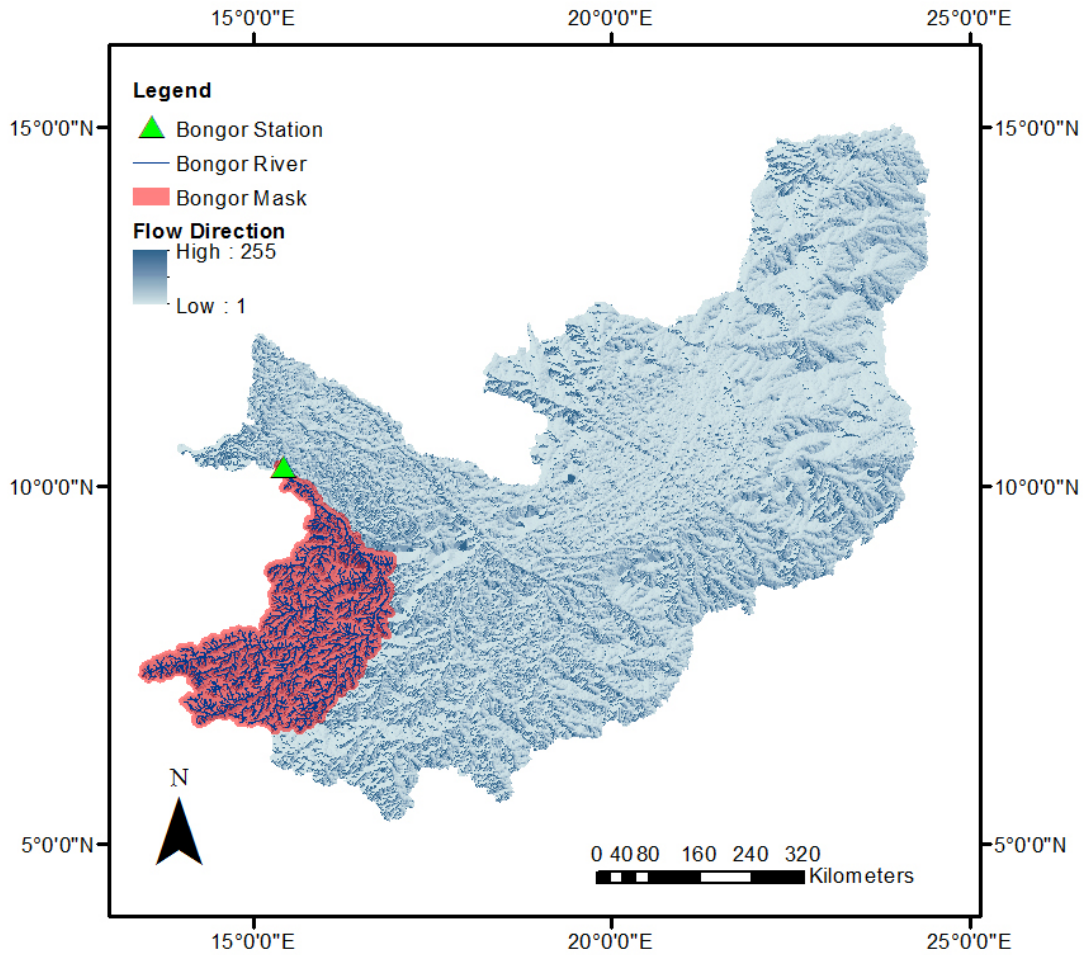


Figure 38. Flow map of Chari-Logone Catchment showing sub-basin used for discharge comparison.

Initially, global parameters for the model were set to default: "a" interception at 4.5, alpha coefficient at 1.5, LP coefficient at 0.85, and an average of 4. Rainy day per month values were also set to model default values. The result was poor with runoff rates being greatly overestimated (Figure 39).

The number of rainy days per month is a required input table into the model and greatly effects recharge estimation. Ground station data from NOAA GHCN Daily for the

N'Djamena, Chad station were used to roughly estimate the number of these rainy days. This station was chosen as it had the most daily data records from 2003 to 2011 as compared to other stations within the study area. The major drawback of the ground station data is only a few days per month were recorded in 2003 severely limiting accuracy and requiring monthly averages from following years for 2003.

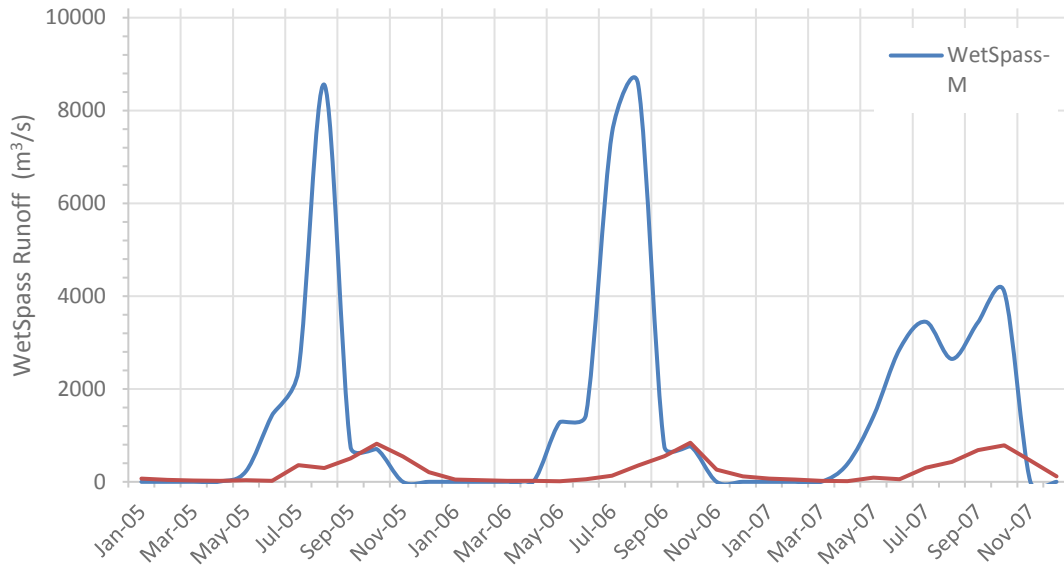


Figure 39. 2005-2007 calculated discharge not considering rainy days per month and using default WetSpas-M settings compared to measurements from Bongor station.

To correct this inaccuracy, rainy days per month from N'Djamena station were used and many iterations of the model were run to find the best global for the study area: "a" interception at 5.8, alfa coefficient at 2.4, LP coefficient at 6.5, and an average of 4. Additionally, Surface water interaction parameters were added with an "x" coefficient of 0.5, beta coefficient of 0.75, and a contribution factor of 0.5. The results based on these settings matched much better with the station measurements.

A Nash-Sutcliffe Efficiency (NSE) of 0.57 was found for the data sets, indicating that the model did well in calculating hydrological parameters (Figure 40), where a value between 0 and 1 is considered good with 1 being the optimal value (Moriassi et al., 2007). An r^2 value of 0.68 (Figure 41) found between the measured and calculated values was also satisfactory. Calculated runoff might have given a better agreement, but there

was significantly less meteorological station data available, and only for 2003, thereby limiting the model only to that year.

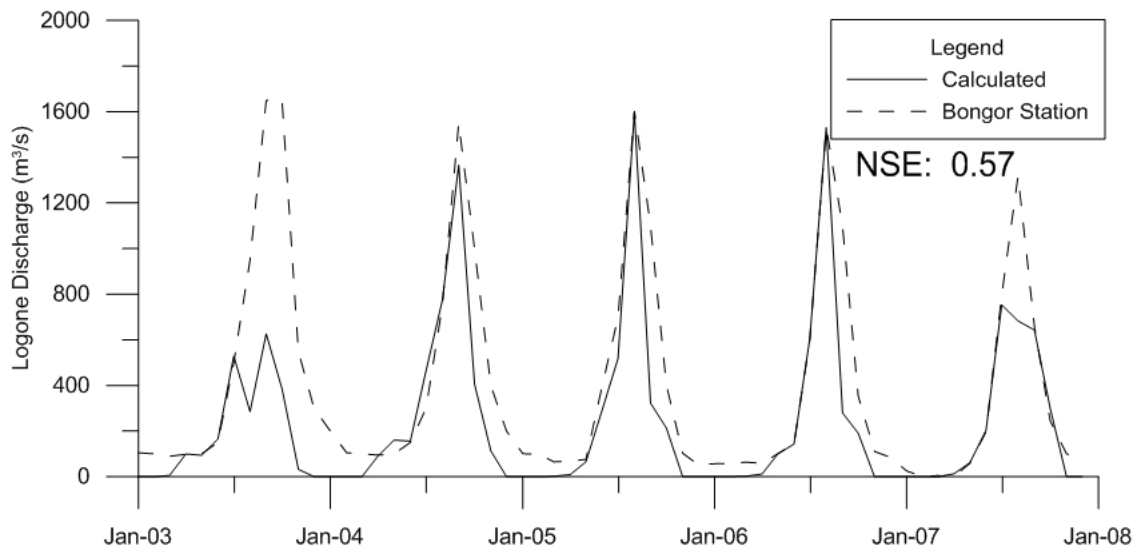


Figure 40. 2003-2007 calculated discharge considering rainy days per month and using site specific WetSpas-M settings compared to measurements from Bongor station.

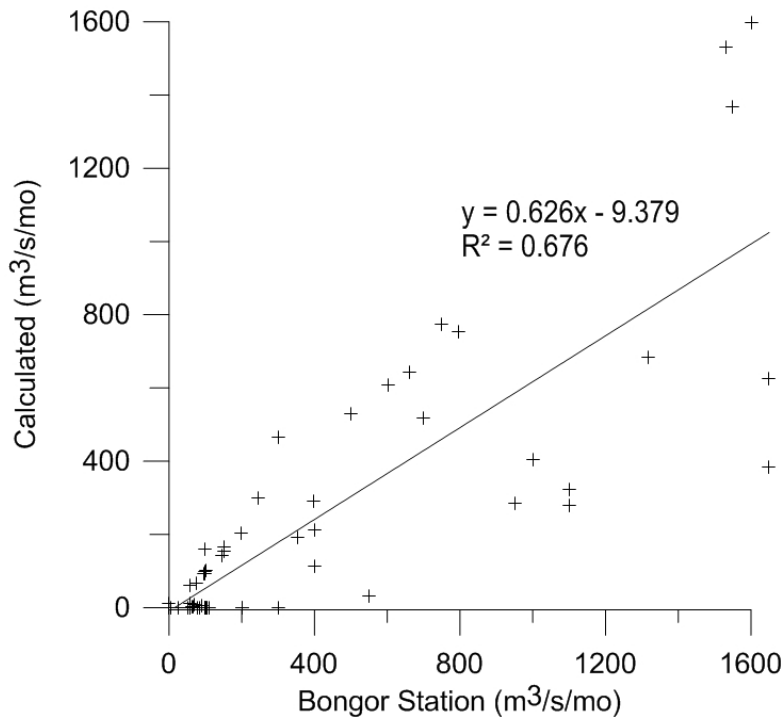


Figure 41. Scatter plot of monthly discharge data from Bongor station compared to model outputs considering burning.

5.2 Analysis of CLC Water Balance

Analysis of the model results considering albedo change from burning shows the majority of precipitation being distributed to ET and recharge (Figure 42). Precipitation peaks during the wet season month of July, whereas PET is at its lowest during that time. The majority of available water from precipitation are lost to ET and groundwater recharge, leaving a smaller portion available for surface runoff.

To take the amount of monthly fire distribution into account, MODIS MOD14/MYD14 fire count was compared to water cycle indicators using general linear least squares regression analysis (Figure 43). Correlation between annual burning changes to water balance parameters are negative. This matches findings by Ichoku et al.

(2016) and supports the idea that that with increased severity of fire, there is a severe decrease in hydrologic parameters including precipitation. To minimize the effects of quantitative biases and uncertainties, correlations between fire count and water-cycle parameters were calculated for the dry season and wet season. Both seasons showed a consistent negative correlation between fire count and water-cycle parameters. The dry season findings differ from what was found in the Ichoku et al. (2016) study. However, it should be noted that the study area of the entire North Central block included significant wetland converted to agriculture, especially near the LCB. The CLC has very little wetland making up a mere 0.2% of total land coverage; the majority of the wetlands of the LCB lie to the northwest of this area. Therefore, it is reasonable to presume that changes due to wetland conversion to cropland mentioned by Ichoku et al. (2016) would not be observed since the land cover is different in this regard. Results from a scatterplot of fire count against precipitation for the CLC shows that burning has an inverse relationship with precipitation (Figure 44). The results look remarkably similar to those found by Ichoku et al. (2016) and further emphasize the complex relationship between burning and monsoonal rainfall.

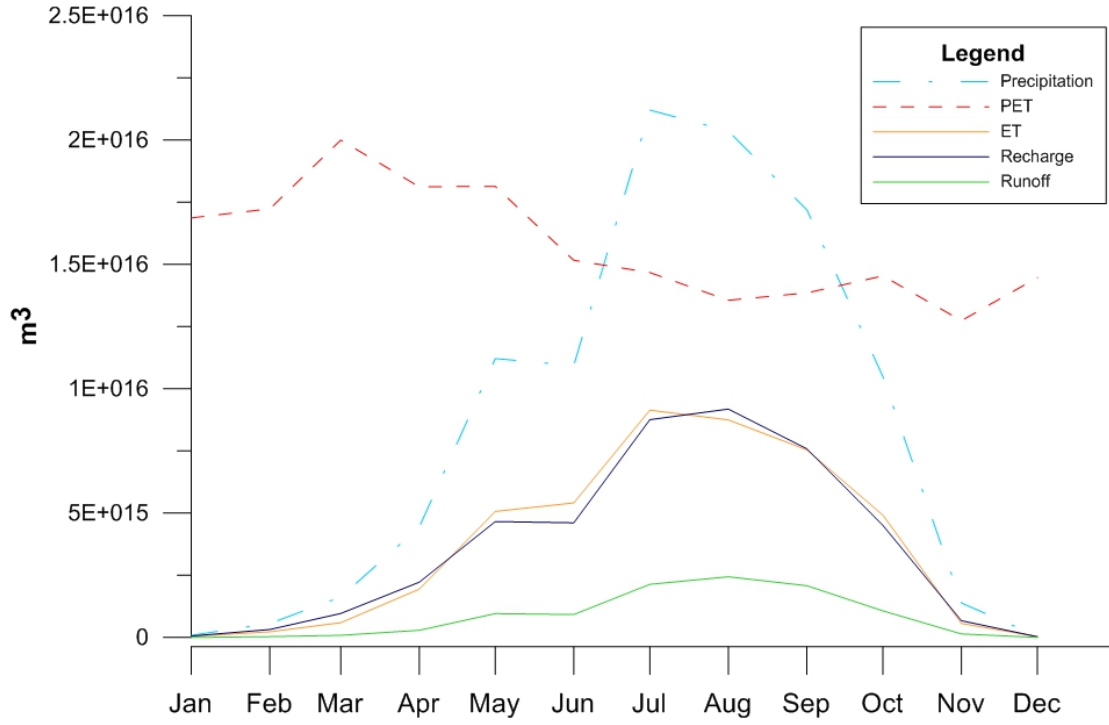


Figure 42. Averaged water balance output parameters from burning model compared to calculated PET considering albedo change from burning.

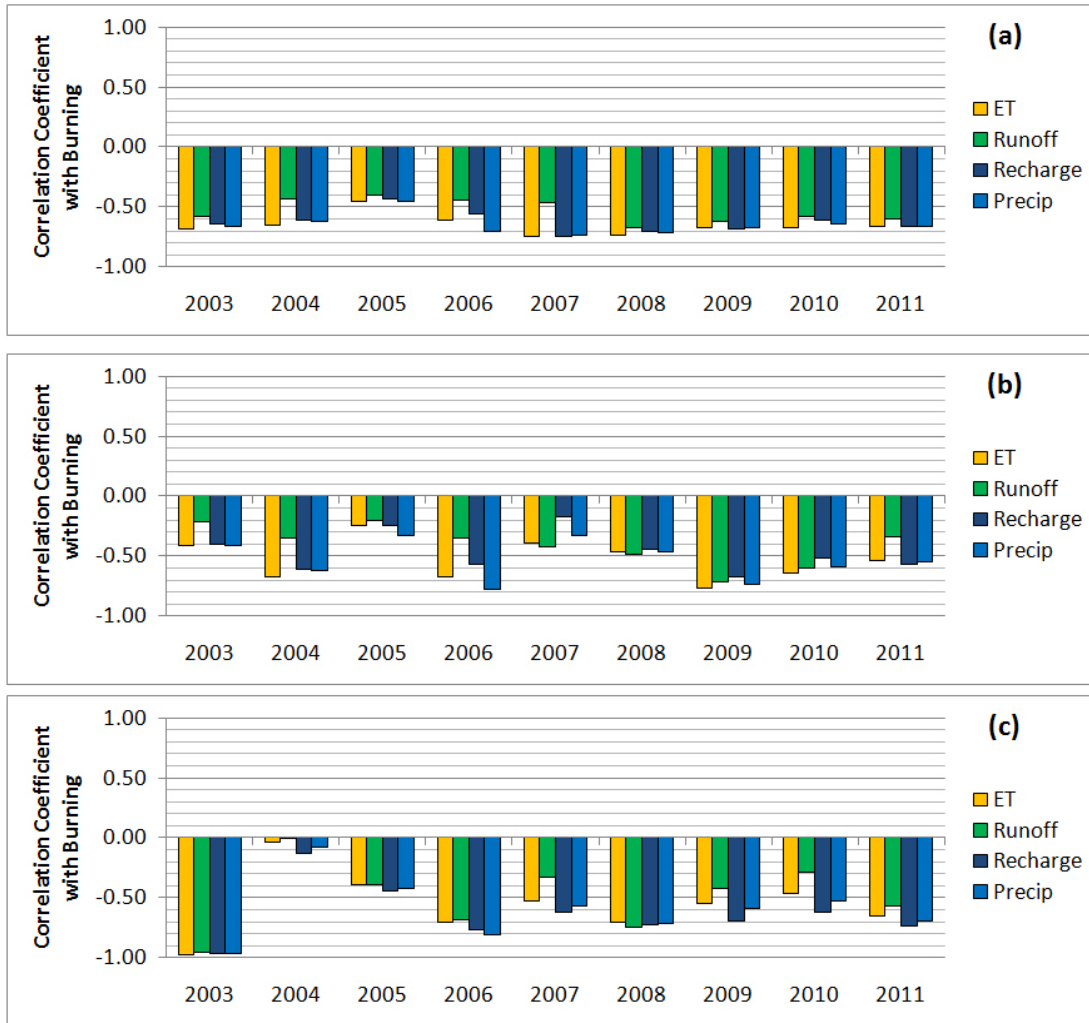


Figure 43. Correlation coefficients between biomass burning count (each count being 2km x 2km pixel) from MOD14/MYD14 Collection 5 compared to water balance model outputs considering burning based on different time periods: (a) integration or averaging through the full-year cycle and, (b) integration or averaging through only the dry season (November–March), (c) integration or averaging through only the wet season (April–October).

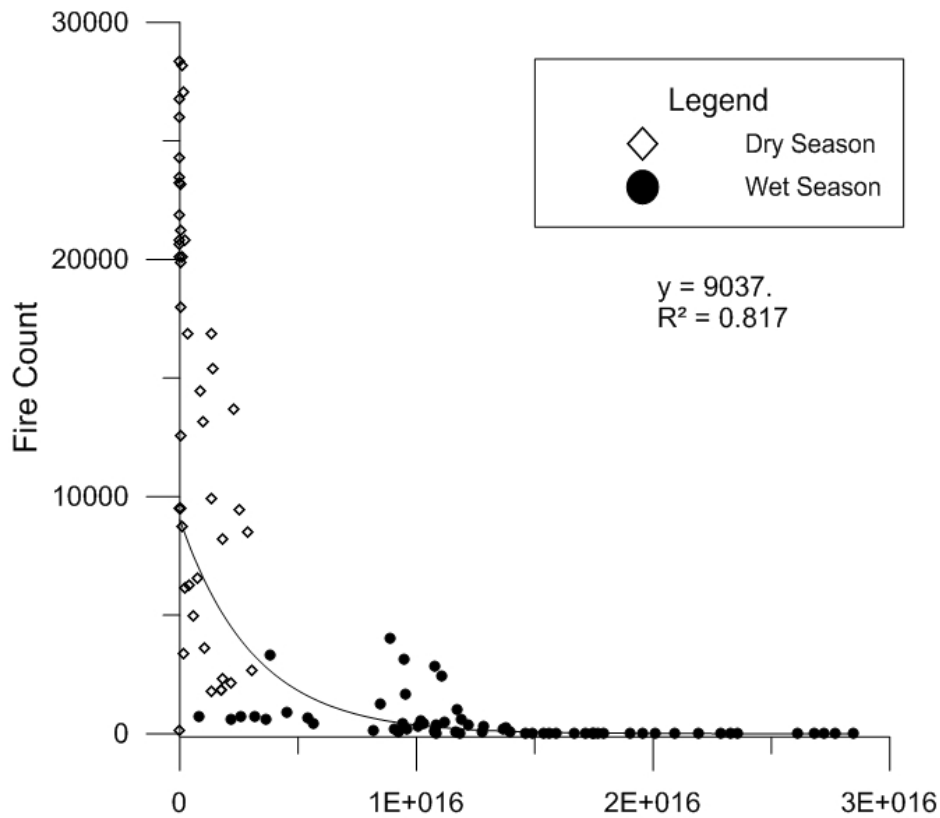
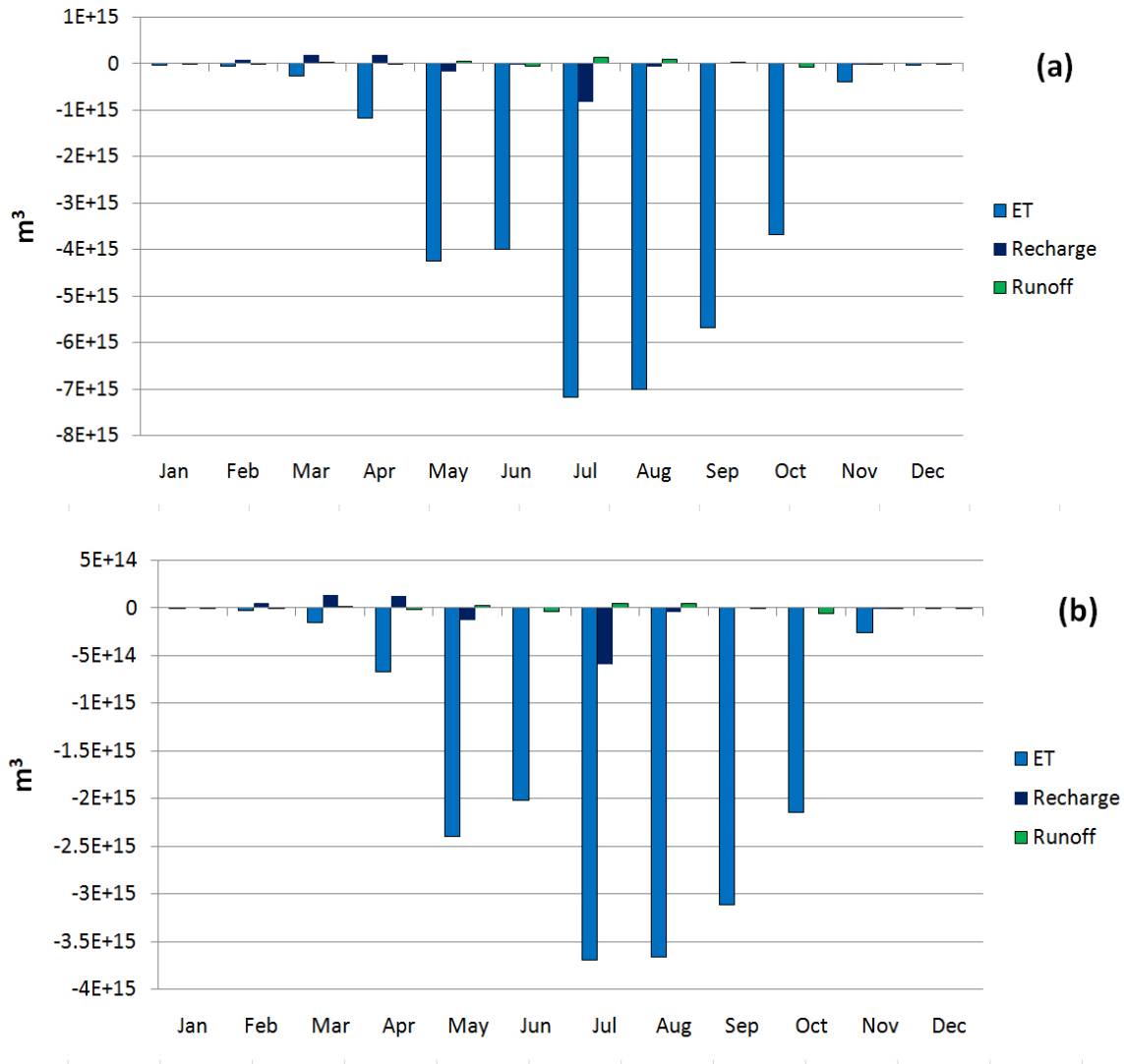


Figure 44. Scatter plot of monthly biomass burning count against precipitation from TRMM showing the demarcation between the monsoonal season (May–October) and dry season (November–March) season.

5.3 Analysis of Water Balance by Land Cover Type

To get a more detailed understanding of fire effect in the catchment, an investigation of the effect of fire by land cover type was performed by extracting the water balance outputs from vegetative land-cover classes. Particular attention was paid to primary grass, savanna, and cropland. All three land cover types show a similar reaction to the combined land cover analysis with a dramatic reduction in ET and irregular monthly change of runoff and recharge. Burning impact on hydrological parameters was determined by

averaging the monthly difference of no burning from burning outputs for 2003 to 2011. While recharge and runoff show alternating increase and decrease, ET shows steady decrease during the wet season due to burning (Oliver and Singels, 2012). Notaro, Wyrwoll, and Chen (2011) found that ET was especially reduced by burning during the early monsoonal season (Figure 45).



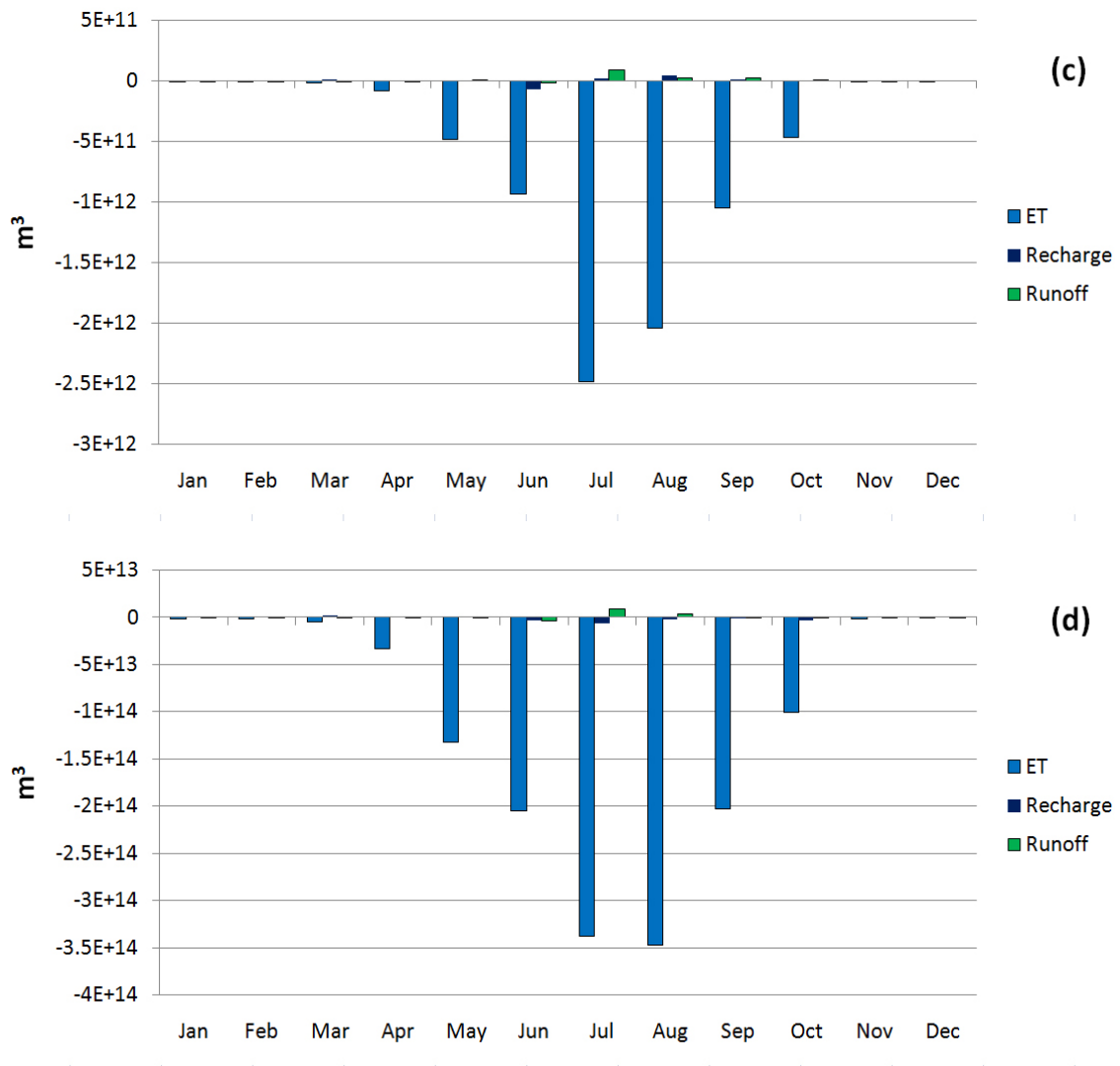


Figure 45. Average output difference from model considering minus model not considering burning. From top to bottom (a) shows burning difference for all three land classes, (b) grassland only, (c) savannah only, (d) cropland only.

5.4 Groundwater Model Results

Groundwater levels from the PMWIN groundwater model showed very good results matching very well with historical water levels records from the Lake Chad Basin Commission (LCBC, 1966) (Figure 46 & 47). With the groundwater model validated, ET from WetSpas-M could then be used as an input into the groundwater model. ET from winter month outputs revealed a reasonable change allowing for the production of potentiality maps. These potentiality maps could be used to show the effect of burning on groundwater levels. Unfortunately, when ET from wet season months were used as model inputs, the model greatly exaggerated the rise of groundwater level indicating large portions of the CLC would be flooded. This may be related to the way WetSpas-M considers water balance especially regarding groundwater recharge. Since WetSpas-M does not consider the portion of recharge that is contributed to the water table, the specific ET calculations considered in WetSpas-M may not be appropriate for ET calculation used for groundwater model input.

Comparison of Calculated and Observed Heads

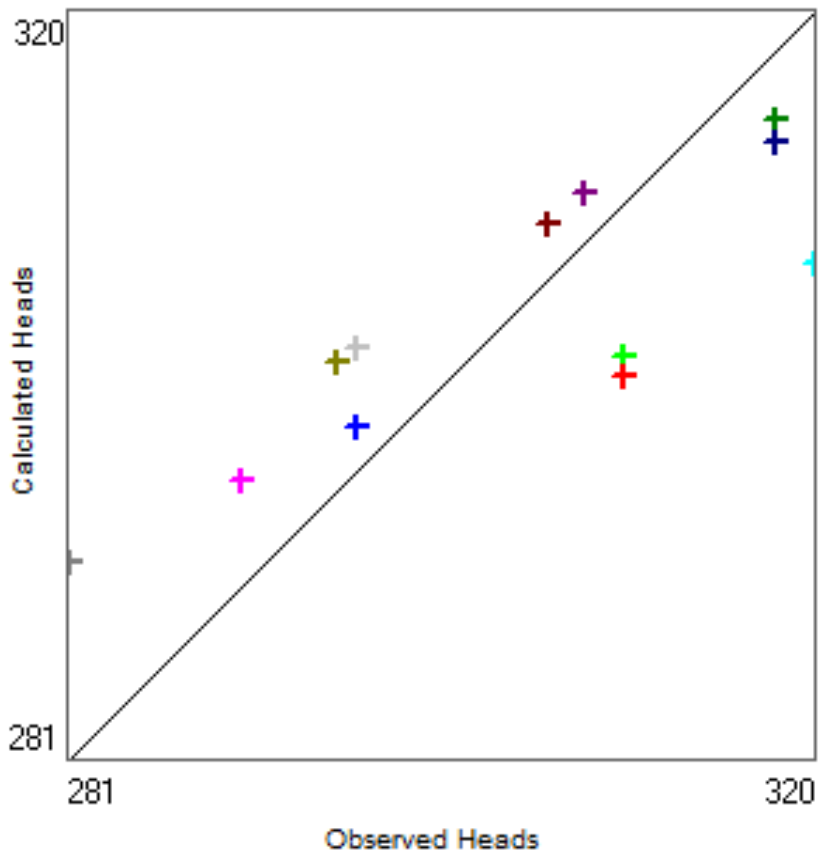


Figure 46. Scatterplot of well observations to groundwater model calculated heads not considering ET.

Comparison of Calculated and Observed Heads

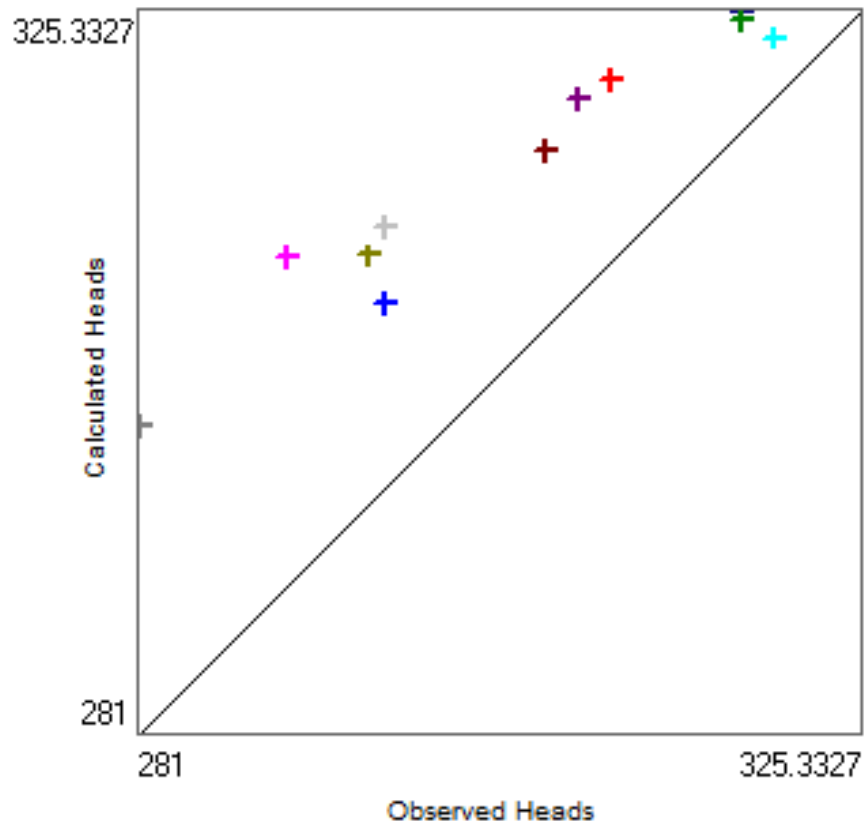


Figure 47. Scatterplot of well observations to groundwater model calculated heads considering January 2009 ET data from WetSpas-M outputs.

CHAPTER 6

CONCLUSION

When comparing model simulations with and without fire activity considerations, a clear pattern of decreased ET is observed. However, lower ET may limit the water available for precipitation and could have significant meteorological impacts on agriculture, though more study in this area is needed.

Burning seems to have a similar impact on the primary land cover types of the CLC, suggesting that vegetation type may not have a significant impact due to burning on hydrological parameters. Through analysis of the seasonal effect of burning, seasonal variation does not seem to have a major impact in relation to burning and water balance. This is inconclusive considering the low amount of burning during the wet season when more precipitation is available. Further research detailing the groundwater recharge along the Chari and Logone rivers would be beneficial to understanding the hydrology of the CLC in relation to fire, but would probably need more field data such as increased rainfall and wind stations as well as groundwater measurements. The distribution of these measurements increasing in number near the confluence of the Chari and Logone Rivers and near their discharge to Lake Chad. If more burning to non-burning albedo comparison data becomes available, a lengthening the study period could be performed, allowing for better analysis of the effect of land cover change on burning in the CLC.

The ability of WetSpas-M to approximate discharge found *in situ* shows great promise using it to calculate hydrological parameters despite severe lack of data. By the use of satellite data, in lieu of meteorological station records, temporal and spatial limitations may be mitigated. Development of a system to incorporate albedo into PET

calculations at a relatively high resolution may prove useful for future studies examining the impact of burning on albedo and land cover type.

APPENDIX

Appendix A.

WetSpass-M Land Use Look-up Table

LUSE_TYPE	RUNOFF_VEG	VEG_AR EA	BARE_ARE A	IMP_ARE A	OPENW_ AREA	ROOT_ DEPTH	LAI	MIN_ST OM	VEG_HE IGH T	nManin g	LandFac tor	Aerody n Resist ance
city center build up	grass	0.200	0.000	0.800	0.000	0.300	2.000	100.000	0.120	0.030	0.667	212.014
build up	grass	0.500	0.000	0.500	0.000	0.300	2.000	100.000	0.120	0.040	0.500	212.014
industry	grass	0.400	0.000	0.600	0.000	0.300	2.000	100.000	0.120	0.035	0.571	212.014
infrastructure	grass	0.600	0.100	0.300	0.000	0.300	2.000	100.000	0.120	0.040	0.500	212.014
sea harbour	grass	0.600	0.100	0.300	0.000	0.300	2.000	100.000	0.120	0.045	0.444	212.014
airport	grass	0.200	0.000	0.800	0.000	0.300	2.000	100.000	0.120	0.030	0.667	212.014
excavation	bare soil	0.000	1.000	0.000	0.000	0.050	0.000	110.000	0.001	0.090	0.222	692.160
open build up	grass	0.600	0.100	0.300	0.000	0.300	2.000	100.000	0.120	0.045	0.444	212.014
agriculture	crop	0.800	0.200	0.000	0.000	0.400	4.000	180.000	0.600	0.037	0.541	115.013
meadow	grass	1.000	0.000	0.000	0.000	0.300	2.000	100.000	0.200	0.070	0.286	177.468
maize and tuberous p	crop	0.800	0.200	0.000	0.000	0.300	4.000	180.000	1.500	0.050	0.400	76.024
wet meadow	grass	1.000	0.000	0.000	0.000	0.300	2.000	100.000	0.300	0.055	0.364	152.495
orchard	forest	0.800	0.200	0.000	0.000	0.800	6.000	150.000	3.000	0.050	0.400	54.699
deciduous forest	forest	1.000	0.000	0.000	0.000	2.000	5.000	250.000	18.000	0.100	0.200	27.196
coniferous forest	forest	1.000	0.000	0.000	0.000	2.000	6.000	500.000	15.000	0.100	0.200	28.631
mixed forest	forest	1.000	0.000	0.000	0.000	2.000	5.000	375.000	16.000	0.100	0.200	28.098
heather	grass	1.000	0.000	0.000	0.000	0.200	6.000	110.000	0.750	0.050	0.400	104.390
shrub	grass	1.000	0.000	0.000	0.000	0.600	6.000	110.000	2.000	0.050	0.400	66.329
beach/dune	bare soil	0.300	0.700	0.000	0.000	0.500	2.000	110.000	1.000	0.040	0.500	91.761
mud flat/salt marsh	open water	0.400	0.200	0.000	0.400	0.300	2.000	110.000	0.500	0.035	0.571	124.221
navigable river	open water	0.000	0.000	0.000	1.000	0.050	0.000	110.000	0.000	0.020	1.000	0.000
lake	open water	0.000	0.000	0.000	1.000	0.050	0.000	110.000	0.000	0.020	1.000	0.000
estuary	open water	0.000	0.000	0.000	1.000	0.050	0.000	110.000	0.000	0.020	1.000	0.000
sea	open water	0.000	0.000	0.000	1.000	0.050	0.000	110.000	0.000	0.020	1.000	0.000
unnavigable river	open water	0.000	0.000	0.000	1.000	0.050	0.000	110.000	0.000	0.020	1.000	0.000
burned grass	bare soil	0.000	1.000	0.000	0.000	0.300	0.000	140.000	0.120	0.020	0.571	212.014
burned coniferous	forest	0.750	0.250	0.000	0.000	2.000	5.000	500.000	15.000	0.020	0.200	28.631
burned deciduous	forest	0.750	0.250	0.000	0.000	2.000	5.000	250.000	18.000	0.020	0.200	27.196
burned mixed forest	forest	0.750	0.250	0.000	0.000	2.000	4.000	375.000	16.000	0.020	0.200	28.098
burned shrubland (savannah)	grass	0.150	0.850	0.000	0.000	0.600	5.000	110.000	2.000	0.020	0.400	66.329
burned cropland	bare soil	0.000	1.000	0.000	0.000	0.400	0.000	180.000	0.600	0.020	0.541	115.013
highway	grass	0.600	0.100	0.300	0.000	0.300	2.000	100.000	0.120	0.025	0.800	212.014

district road	grass	0.60 0	0.100	0.300	0.000	0.300	2.000	100.000	0.120	0.040	0.500	212.014
spruce	forest	1.00 0	0.000	0.000	0.000	2.000	12.00 0	320.000	13.000	0.400	0.050	29.919
pine	forest	1.00 0	0.000	0.000	0.000	2.000	6.000	550.000	15.000	0.400	0.050	28.631
beech	forest	1.00 0	0.000	0.000	0.000	2.000	6.000	320.000	20.000	0.400	0.050	26.463
birch	forest	1.00 0	0.000	0.000	0.000	2.000	5.000	320.000	16.000	0.400	0.050	28.098
oak	forest	1.00 0	0.000	0.000	0.000	2.000	4.000	150.000	17.000	0.400	0.050	27.622
poplar	forest	1.00 0	0.000	0.000	0.000	2.000	5.000	250.000	18.000	0.400	0.050	27.196
reference grass	grass	1.00 0	0.000	0.000	0.000	0.300	2.000	140.000	0.120	0.035	0.571	212.014

Appendix B.

NOAA NCEI Global Summaries of the Day Stations Used for

Averaging Monthly Wind Speed

Station	Latitude	Longitude	Station	Latitude	Longitude
622000	26.6	12.783	622120	25.146	10.143
647000	12.134	15.034	610900	13.779	8.984
629410	4.872	31.601	628090	11.333	27.817
627500	14	32.333	626000	21.817	31.483
606700	24.293	9.452	610800	13.503	7.127
627720	13.167	32.667	624140	23.964	32.82
628010	11.75	32.783	610960	13.233	11.983
622710	24.179	23.314	651250	9.25	7
646620	5.05	21.2	650460	12.048	8.525
627810	12.7	28.433	628100	11.138	29.701
622590	25.8	21.133	610240	16.967	7.967
628030	11.867	31.05	646550	6.533	21.983
624320	25.5	28.967	610450	13.983	10.3
646600	5.85	20.65	610850	13.373	12.627
651340	9.64	8.869	624030	26.2	32.75
626600	18.55	31.85	610490	14.25	13.117
650820	11.85	13.083	624350	25.45	30.533
628800	7.7	28.017	610910	12.983	8.933
651670	9.258	12.43	627700	13.483	22.45
627900	12.05	24.883	624050	25.671	32.707
628400	9.559	31.652	646010	5.967	15.633
610170	18.683	12.917	626500	19.154	30.43
650190	10.696	7.32	627210	15.589	32.553
606400	26.724	8.623	627600	13.615	25.325

Appendix C.

Python Program for Wind Speed Data

```
#Begin

#Import module

import csv

#File name

isd_name = 'isd-history'

#Import file and parse stations

with open(isd_name+'.csv') as f:

    reader = csv.reader(f, delimiter=',')

    next(f, None)    #Skip first line

    next(f, None)

    station_lat_lon = []

    for row in reader:

        sname = (row[0])

        lat = (row[1])

        lon = (row[2])

        station_lat_lon.append([sname,lat,lon])
```

```
#Match station lat/lon, format, and print list
x= 606400
for i in range(0,len(station_lat_lon)):
    if int(station_lat_lon[i][0]) == x:
        print(station_lat_lon[i][0],station_lat_lon[i][1],station_lat_lon[i][2])
```

Appendix D.

Albedo Table of Land Use Without Fire

Landcover Type	Jan	Feb	Mar	Apr	May	Jun	Jul	Aug	Sep	Oct	Nov	Dec
Water	0.080	0.080	0.080	0.080	0.080	0.080	0.080	0.080	0.080	0.080	0.080	0.080
Evergreen Needleleaf forest	0.123	0.127	0.140	0.140	0.138	0.148	0.140	0.138	0.140	0.130	0.130	0.120
Evergreen Broadleaf forest	0.123	0.127	0.140	0.140	0.138	0.148	0.140	0.138	0.140	0.130	0.130	0.120
Deciduous Needleleaf forest	0.123	0.127	0.140	0.140	0.138	0.148	0.140	0.138	0.140	0.130	0.130	0.120
Deciduous Broadleaf forest	0.123	0.127	0.140	0.140	0.138	0.148	0.140	0.138	0.140	0.130	0.130	0.120
Mixed forest	0.123	0.127	0.140	0.140	0.138	0.148	0.140	0.138	0.140	0.130	0.130	0.120
Closed shrublands	0.167	0.184	0.195	0.193	0.201	0.209	0.219	0.228	0.183	0.164	0.155	0.164
Open shrublands	0.167	0.184	0.195	0.193	0.201	0.209	0.219	0.228	0.183	0.164	0.155	0.164
Woody savannas	0.128	0.137	0.148	0.151	0.155	0.157	0.145	0.147	0.137	0.144	0.130	0.126
Savannas	0.135	0.147	0.159	0.160	0.162	0.158	0.151	0.143	0.135	0.147	0.130	0.130
Grassland	0.155	0.165	0.175	0.180	0.187	0.189	0.166	0.158	0.155	0.006	0.003	0.004
Wetlands	0.080	0.080	0.080	0.080	0.080	0.080	0.080	0.080	0.080	0.080	0.080	0.080
Croplands	0.155	0.164	0.170	0.172	0.167	0.170	0.157	0.144	0.146	0.160	0.148	0.152
Urban and built-up	0.250	0.250	0.250	0.250	0.250	0.250	0.250	0.250	0.250	0.250	0.250	0.250
Natural vegetation mosaic	0.155	0.162	0.171	0.178	0.178	0.174	0.157	0.161	0.152	0.157	0.151	0.155
Snow	0.850	0.850	0.850	0.850	0.850	0.850	0.850	0.850	0.850	0.850	0.850	0.850
Barren	0.175	0.175	0.175	0.175	0.175	0.175	0.175	0.175	0.175	0.175	0.175	0.175

Appendix E.

Albedo Table of Land Use Considering Fire

Landcover Type	Jan	Feb	Mar	Apr	May	Jun	Jul	Aug	Sep	Oct	Nov	Dec
Water	0.080	0.080	0.080	0.080	0.080	0.080	0.080	0.080	0.080	0.080	0.080	0.080
Evergreen Needleleaf forest	0.125	0.122	0.140	0.139	0.137	0.146	0.148	0.137	0.146	0.130	0.132	0.118
Evergreen Broadleaf forest	0.125	0.122	0.140	0.139	0.137	0.146	0.148	0.137	0.146	0.130	0.132	0.118
Deciduous Needleleaf forest	0.125	0.122	0.140	0.139	0.137	0.146	0.148	0.137	0.146	0.130	0.132	0.118
Deciduous Broadleaf forest	0.125	0.122	0.140	0.139	0.137	0.146	0.148	0.137	0.146	0.130	0.132	0.118
Mixed forest	0.125	0.122	0.140	0.139	0.137	0.146	0.148	0.137	0.146	0.130	0.132	0.118
Closed shrublands	0.167	0.184	0.195	0.194	0.201	0.217	0.229	0.222	0.181	0.163	0.157	0.163
Open shrublands	0.167	0.184	0.195	0.194	0.201	0.217	0.229	0.222	0.181	0.163	0.157	0.163
Woody savannas	0.127	0.134	0.147	0.151	0.155	0.159	0.149	0.147	0.140	0.147	0.132	0.124
Savannas	0.133	0.143	0.160	0.161	0.164	0.163	0.152	0.143	0.136	0.151	0.130	0.127
Grassland	0.154	0.165	0.175	0.182	0.185	0.193	0.168	0.162	0.154	0.005	0.003	0.003
Wetlands	0.080	0.080	0.080	0.080	0.080	0.080	0.080	0.080	0.080	0.080	0.080	0.080
Croplands	0.156	0.161	0.171	0.174	0.164	0.171	0.155	0.142	0.147	0.160	0.151	0.153
Urban and built-up	0.250	0.250	0.250	0.250	0.250	0.250	0.250	0.250	0.250	0.250	0.250	0.250
Natural vegetation mosaic	0.155	0.159	0.172	0.179	0.177	0.176	0.159	0.159	0.152	0.157	0.152	0.154
Snow	0.850	0.850	0.850	0.850	0.850	0.850	0.850	0.850	0.850	0.850	0.850	0.850
Barren	0.175	0.175	0.175	0.175	0.175	0.175	0.175	0.175	0.175	0.175	0.175	0.175

Appendix F.

NOAA NCEI Climate Stations Used for Relative Humidity and to

Calculate Extraterrestrial Radiation and Surface Radiation.

STATION	NAME	LATITUDE	LONGITUDE	ELEVATION
SU000062640	ABU HAMED, SU	19.533	33.317	312
NG000061024	AGADEV, NG	16.967	7.967	505
EG000062414	ASSWAN, EG	23.9667	32.7831	200
SUM00062680	ATBARA, SU	17.7	33.967	345
CT000004660	BAMBARI, CT	5.77	20.67	448
CT000004656	BANGASSOU, CT	4.73	22.83	500
CT000004600	BERBERATI, CT	4.22	15.78	583
NG000061017	BILMA, NG	18.683	12.917	357
NG000001075	BIRNI N KONNI, NG	13.8	5.25	272
GB000004510	BITAM, GB	2.08	11.48	599
BNM00065338	BOHICON, BN	7.167	2.067	167
CT000004610	BOSSANGO, CT	6.48	17.43	465
CT000004605	BOSSEMBELE, CT	5.27	17.63	674
CTM00064601	BOUAR, CT	5.967	15.633	1020
EG000062432	DAKHLA, EG	25.4831	29	107
UVM00065505	DEDOUGOU, UV	12.467	3.483	300
NGM00061085	DIFFA, NG	13.373	12.627	303

SU000062650	DONGOLA, SU	19.167	30.483	226
CM000004910	DOUALA, CM	4.02	9.72	13
SUM00062750	ED DUEIM, SU	14	32.333	378
SU000062771	EL OBEID, SU	13.167	30.233	574
CMM00064860	GAROUA, CM	9.336	13.37	242
NGM00061099	GAYA, NG	11.883	3.45	202
LYM00062212	GHAT, LY	25.146	10.143	699.8
NGM00061045	GOURE, NG	13.983	10.3	460
EG000062463	HURGUADA, EG	27.15	33.7167	16
AGM00060640	ILLIZI TAKHAMALT, AG	26.724	8.623	541.9
CF000064459	IMPFONDO, CF	1.617	18.067	327
BN000065306	KANDI, BN	11.133	2.933	292
EGM00062435	KHARGA, EG	25.45	30.533	73
SU000062721	KHARTOUM, SU	15.6	32.549	380
SUM00062772	KOSTI RABAK, SU	13.167	32.667	381
NGM00061091	MAGARIA, NG	12.983	8.933	403
NG000061096	MAINE SOROA, NG	13.233	11.983	337
GB000004556	MAKOKOU, GB	0.57	12.87	516
SU000062840	MALKAL, SU	9.55	31.65	388
NG000001080	MARADI, NG	13.47	7.08	388
ML000061250	MENAKA, ML	15.867	2.217	278

CTM00064665	MOBAYE, CT	4.317	21.183	406
CT000004654	N DELE, CT	8.4	20.65	510
NG000001049	N GUIGNI, NG	14.25	13.12	289
BN000005319	NATITINGOU, BN	10.32	1.48	460
CD000004700	NDJAMENA, CD	12.13	15.03	295
LYM00062200	OBARI, LY	26.6	12.783	463
CF000004458	OUESSO, CF	1.62	16.05	340
BNM00065330	PARAKOU, BN	9.35	2.617	393
CD000004750	SARH, CD	9.15	18.38	0
LY000062124	SEBHA, LY	27.02	14.45	432
SU000062762	SENNAR, SU	13.55	33.617	418
EGM00062403	SOUTH OF VALLEY UNIVERSITY, EG	26.2	32.75	96
TO000005380	TABLIGBO, TO	6.58	1.5	51
NG000061043	TAHOUA, NG	14.9	5.25	391
AG000060680	TAMANRASSET, AG	22.8	5.4331	1362
LYM00062259	TAZERBO, LY	25.8	21.133	261
NG000001036	TILLABERY, NG	14.22	1.45	209
AGM00060670	TISKA, AG	24.293	9.452	968
SUM00062751	WAD MEDANI, SU	14.4	33.483	408
CT000004661	YALINGA, CT	6.5	23.27	602

NG000001090	ZINDER, NG	13.8	9	489
-------------	------------	------	---	-----

Appendix G.

ASCII to Tiff Arcpy Tool

```
#-----  
# Ascii to tif for ArcGIS 10.x  
#  
# Python code by Forrest Black  
# Department of Geosciences, University of Missouri - Kansas City  
#  
# Date: 2.21.2016  
#  
#-----  
  
# Import system modules  
importarcgisscripting, os  
  
# Create the Geoprocessor object  
gp = arcgisscripting.create()  
  
importarcpy  
  
importos  
  
import glob  
  
# Path to ascii files_
```

```

filepath = r"G:\Thesis\Lake_Chad\WetSpass_albedo\NoFire\2003\outputs"

# Path where to put rasters

outFolder = r"G:\Thesis\Lake_Chad\WetSpass_albedo\NoFire\2003\output_rasters\LCB"

ascList = glob.glob(filepath + "/*.asc")

printascList

for ascFile in ascList:

    outRaster = outFolder + "/" + os.path.split(ascFile)[1][:-3] + ".tif"

    printoutRaster

    arcpy.ASCIIToRaster_conversion(ascFile, outRaster, "FLOAT")

# ASCII to RasterConversion Finished-----
-

arcpy.AddMessage("    Done!")

```

Appendix H.

Summation of Raster by Land Use Class Arcpy Tool

```
#-----  
# Python Code for class conversion ArcGIS 10.x  
#  
# Python code by Forrest Black  
# Department of Geosciences, University of Missouri - Kansas City  
#  
# Date: 2.21.2016  
#  
#-----  
  
# Import the arcpy site package  
  
import arcpy, numpy  
  
import csv  
  
import os  
  
  
type = 'Fire'  
  
yr = '2011'  
  
mydir = r'G:\Thesis\Lake_Chad\Analysis\WetSpass-M\Chari\ '  
  
os.chdir(mydir)  
  
arcpy.env.workspace = mydir
```

```

out = open(mydir+yr+type+ 'fire_frst.csv', 'w')

out.write('{} , {} , {} , {} , {} , {} , {} , {} , {} , {} , {} \n'.format('Year','Month','CF_ET','CF_Runoff',
'CF_Recharge','DF_ET','DF_Runoff','DF_Recharge','MF_ET','MF_Runoff','MF_Recharg
e'))

for i in range(1,13):

# Crop ET

    et_raster1 = r'G:\Thesis\Lake_Chad\Analysis\WetSpas-
M\Chari\Fire\2011\cf\et'+str(i)+'.tif'

    et_array1 = arcpy.RasterToNumPyArray(et_raster1, nodata_to_value = 0)

    et_output1 = et_array1.sum()

    et_output1 = str(et_output1)

    arcpy.AddMessage(str(i)+' Crop ET ' + str(et_output1))

# Crop Runoff

    ro_raster1 = r'G:\Thesis\Lake_Chad\Analysis\WetSpas-
M\Chari\Fire\2011\cf\ro'+str(i)+'.tif'

    ro_array1 = arcpy.RasterToNumPyArray(ro_raster1, nodata_to_value = 0)

    ro_output1 = ro_array1.sum()

    ro_output1 = str(ro_output1)

    arcpy.AddMessage(str(i)+' Crop Runoff ' + str(ro_output1))

```

```
# Crop Recharge
```

```
rchg_raster1 = r'G:\Thesis\Lake_Chad\Analysis\WetSpas-  
M\Chari\Fire\2011\cf\rchg'+str(i)+''.tif  
  
rchg_array1 = arcpy.RasterToNumPyArray(rchg_raster1, nodata_to_value = 0)  
  
rchg_output1 = rchg_array1.sum()  
  
rchg_output1 = str(rchg_output1)  
  
arcpy.AddMessage(str(i)+' Crop Recharge ' + str(rchg_output1))
```

```
# Savanna ET
```

```
et_raster2 = r'G:\Thesis\Lake_Chad\Analysis\WetSpas-  
M\Chari\Fire\2011\df\et'+str(i)+''.tif  
  
et_array2 = arcpy.RasterToNumPyArray(et_raster2, nodata_to_value = 0)  
  
et_output2 = et_array2.sum()  
  
et_output2 = str(et_output2)  
  
arcpy.AddMessage(str(i)+' Savanna ET ' + str(et_output2))
```

```
# Savanna Runoff
```

```
ro_raster2 = r'G:\Thesis\Lake_Chad\Analysis\WetSpas-  
M\Chari\Fire\2011\df\ro'+str(i)+''.tif  
  
ro_array2 = arcpy.RasterToNumPyArray(ro_raster2, nodata_to_value = 0)  
  
ro_output2 = ro_array2.sum()  
  
ro_output2 = str(ro_output2)
```

```

arcpy.AddMessage(str(i)+' Savanna Runoff ' + str(ro_output2))

# Savanna Recharge

rchg_raster2 = r'G:\Thesis\Lake_Chad\Analysis\WetSpas-
M\Chari\Fire\2011\df\rchg'+str(i)+'.tif'

rchg_array2 = arcpy.RasterToNumPyArray(rchg_raster2, nodata_to_value = 0)

rchg_output2 = rchg_array2.sum()

rchg_output2 = str(rchg_output2)

arcpy.AddMessage(str(i)+' Savanna Recharge ' + str(rchg_output2))

# Grass ET

et_raster3 = r'G:\Thesis\Lake_Chad\Analysis\WetSpas-
M\Chari\Fire\2011\mf\et'+str(i)+'.tif'

et_array3 = arcpy.RasterToNumPyArray(et_raster3, nodata_to_value = 0)

et_output3 = et_array3.sum()

et_output3 = str(et_output3)

arcpy.AddMessage(str(i)+' Grass ET ' + str(et_output3))

# Grass Runoff

ro_raster3 = r'G:\Thesis\Lake_Chad\Analysis\WetSpas-
M\Chari\Fire\2011\mf\ro'+str(i)+'.tif'

ro_array3 = arcpy.RasterToNumPyArray(ro_raster3, nodata_to_value = 0)

ro_output3 = ro_array3.sum()

```

```

ro_output3 = str(ro_output3)

arcpy.AddMessage(str(i)+' Grass Runoff ' + str(ro_output3))

# Grass Recharge

rchg_raster3 = r'G:\Thesis\Lake_Chad\Analysis\WetSpas-
M\Chari\Fire\2011\mf\rchg'+str(i)+'.tif'

rchg_array3 = arcpy.RasterToNumPyArray(rchg_raster3, nodata_to_value = 0)

rchg_output3 = rchg_array3.sum()

rchg_output3 = str(rchg_output3)

arcpy.AddMessage(str(i)+' Grass Recharge ' + str(rchg_output3))

out.write('{} , {} , {} , {} , {} , {} , {} , {} , {} , {} , {} \n'.format(yr,str(i),et_output1,ro_outpu
t1,rchg_output1,et_output2,ro_output2,rchg_output2,et_output3,ro_output3,rchg_output3
))

out.close()

```

Appendix I.

BGR Stations Used for River Input in Groundwater Model.

Station Name	Gage Height (m)	Width (m)
NDJAMENA TP	5.88	326.90
MAILAO	5.01	436.20
Kouloumbou	5.95	77.20
LOGONE GANA	5.95	206.00
Katoa	4.09	207.10
Bongor	4.01	326.10

REFERENCES

- Abdollahi, K., Bashir, I., Verbeiren, B. et al. (2017). *A distributed monthly water balance model: formulation and application on Black Volta Basin. Environmental Earth Sciences*, 76(198). <https://doi.org/10.1007/s12665-017-6512-1>.
- Al-Hamdan, M.Z., Oduor, P., Flores, A.I., Kotikot, S.M., Mugo, R., Ababu, J., & Farah, H. (2017). Evaluating land cover changes in Eastern and Southern Africa from 2000 to 2010 using validated Landsat and MODIS data. *International Journal of Applied Earth Observation and Geoinformation* (62), 8-26, <https://doi.org/10.1016/j.jag.2017.04.007>.
- Allen, R.G., Smith, M., Pereira, L.S., & Perrier, A. (1994). An update for the calculation of reference evapotranspiration. *ICID Bull.* 43(2), 35–92.
- Babamaaji, R. A. (2013). *Impacts of precipitation, land use land cover and soil type on the water balance of Lake Chad Basin*. UMI 3610188. ProQuest LLC.
- Babamaaji, R. A., & Lee, J. (2014). Land use/land cover classification of the vicinity of lake chad using NigeriaSat-1 and landsat data. *Environmental Earth Sciences*, 71(10), 4309-4317. doi:10.1007/s12665-013-2825-xnd *Envir.* 126: 67-80.
- Batelaan, O., & De Smedt, F. (2007). GIS-based recharge estimation by coupling surface-subsurface water balances. *Journal of Hydrology*, 337(3-4), 337-355. doi:10.1016/j.jhydrol.2007.02.001.
- Boronina, A., Favreau, G., Coudrain, A., Leduc, C. & Dieulin, C. (2007). Hydrogeology of the Phreatic Aquifer in the Lake Chad Basin: Groundwater Modeling in Conditions of Data Scarcity. *HydroSciences*. Montpellier, France: IRD-Université de Montpellier II.
- Boronina A., & Ramillien, G. (2008). Application of AVHRR Imagery and GRACE Measurements for Calculation of Actual Evapotranspiration over the Quaternary Aquifer (Lake Chad Basin) and Validation of Groundwater Models. *Journal of Hydrology* 348(1-2), 98–109.
- Bosilovich, M. G. (2006). A comparison of MODIS land surface temperature with in situ observations, *Geophysical Research Letters*, 33, L20112, doi:10.1029/2006GL027519.
- Bouchez, C., Goncalves, J., Deschamps, P., Vallet-Coulomb, C., Hamelin, B., Doumnang, J. -, & Sylvestre, F. (2016). Hydrological, chemical, and isotopic budgets of Lake Chad: A quantitative assessment of evaporation, transpiration and infiltration fluxes. *Hydrology and Earth System Sciences*, 20(4), 1599-1619. doi:10.5194/hess-20-1599-2016.

- Bowman D., Balch, J., Artaxo, P., Bond, W., Carlson, J., Cochrane, M.D., Antonio, C., DeFries R., Doyle, J., Harrison, S., Johnston, F., Keeley, J., Krawchuk, M., Kull, C., Marston, J., Moritz, M., Prentice, I., Roos, C., Scott, A., Swetnam, T., van der Werf, G., & Pyne, S. (2009). Fire in the earth system. *Science* 324, 481–484.
- Brutsaert, W. (2005). *Hydrology: An introduction*. Cambridge: Cambridge University Press.
- Buma, W. G., Lee, S., & Seo, J. Y. (2016). Hydrological evaluation of Lake Chad basin using space borne and hydrological model observations. *Water (Switzerland)*, 8(5), 205. doi:10.3390/w8050205.
- Candela, L., Elorza, F. J., Tamoh, K., Jiménez-Martínez, J., & Aureli, A. (2014). Groundwater modelling with limited data sets: The chari-logone area (Lake Chad basin, Chad). *Hydrological Processes*, 28(11), 3714-3727. doi:10.1002/hyp.9901
- Carter, R. C., Morgulis, E. D., Dottridge, J., & Agbo, J. U. (1994). Groundwater Modeling with Limited Data: A Case Study in a Semi-arid dunefield of Northeast Nigeria. *Quarterly Journal of Engineering Geology*, 27(85-94), 0481-2085/94.
- Coe, M. T. & Foley, J. A. (2001). Human and natural impacts on the water resources of the Lake Chad Basin. *Journal of Geophysical Research*, 106(D4), 3349–3356.
- Eberschweiler, C. (1993). Monitoring and management of groundwater resources in the Lake Chad Basin: Mapping of aquifers water resource management. *Final report R35985. BRGM, Orle´ans, France*.
- Coll, C., Wan, Z., & J. M. Galve. (2009). Temperature-based and radiance-based validations of the V5 MODIS land surface temperature product. *Journal of Geophysical Research*, 114, D20102, doi:10.1029/2009JD012038.
- De Bano, L. F. (1981). *Water repellent soils: A state-of-the-art*. US Department of Agriculture, Forest Service, General Technical Report, (PSW-46).
- De Sales, F., Xue, Y., & Okin, G. S. (2016). Impact of burned areas on the northern African seasonal climate from the perspective of regional modeling. *Climate Dynamics*, 47(11), 3393-3413. doi:10.1007/s00382-015-2522-4.
- Eklund, L., Romankiewicz, C., Brandt, M., Doevenspeck, M., & Samimi, C. (2016). Data and methods in the environment-migration nexus: A scale perspective. *Erde*, 147(2), 139-152. doi:10.12854/erde-147-10.
- Engelstaedter, S., & Washington, R. (2014). *Evaluation of reanalysis near-surface winds over northern Africa in Boreal summer*. EGU General Assembly 2014 April 27 - Vienna, Austria, id.13169.

- Food and Agricultural Organization. (2009). Adaptive water management in the Lake Chad Basin: Addressing current challenges and adapting to future needs. *Food and Agriculture Organization (FAO) Water Seminar Proceedings*. World Water Week, Stockholm, August 16-22, 10-19.
- Friedl, M.A., Sulla-Menashe, D., Tan, B., Schneider, A., Ramankutty, N., Sibley, A., & Huang, X. (2010). MODIS collection 5 global land cover: Algorithm refinements and characterization of new datasets. *Remote Sensing of Environment* 114, 168–182.
- Friedl, M.A., McIver, D.K., Hodges, J.C., Zhang, X., Muchoney, D., Strahler, A.H., Woodcock, C.E., Gopal, S., Schneider, A., & Cooper, A. (2002). Global land cover mapping from MODIS: Algorithms and early results. *Remote Sensing of Environment* 83, 287–302.
- Gao, H., Bohn, T. J., Podest, E., McDonald, K. C., & Lettenmaier, D. P. (2011). On the causes of the shrinking of Lake Chad. *Environmental Research Letters*, 6(3), doi:10.1088/1748-9326/6/3/034021.
- Gatebe, C. K., Ichoku, C. M., Poudyal, R., Román, M. O., & Wilcox, E. (2014) Surface albedo darkening from wildfires in Northern Sub-Saharan Africa. *Environmental Research Letters*, 9(6), 5003.
- Gessner, U., Bliefernicht, J., Rahmann, M., & Dech, S. (2012). Land cover maps for regional climate modeling in West Africa—a comparison of datasets. *Proceedings of the 32nd Annual EARSeL Symposium. Advances in Geosciences* (388-397).
- Giglio, L., Descloitres, J., Justice, C. O., & Kaufman, Y. J. (2003). An enhanced contextual fire detection algorithm for MODIS. *Remote Sensing of Environment*, 87(2–3), 273–282, doi:10.1016/S0034-4257(03)00184-6.
- Govaerts, Y., Pereira, J., Pinty, B., & Mota, B. (2002). Impact of fires on surface albedo dynamics over the African continent. *Journal of Geophysical Research-Atmospheres* 107(D22), 4629. doi:10.1029/2002JD002388.
- Harbaugh, A.W. (2005). MODFLOW-2005, The U.S. Geological Survey modular groundwater model—the groundwater flow process: U.S. Geological survey techniques and methods 6-A16, variously p.
- Hughes, D.A. (2006). Comparison of satellite rainfall data with observations from gauging station networks. *Journal of Hydrology*, 327, 399–410, <https://doi.org/10.1016/j.jhydrol.2005.11.041>.
- Hulley, G. C. & Hook, S. J. (2009) Intercomparison of versions 4, 4.1 and 5 of the MODIS Land Surface Temperature and Emissivity products and validation with

- laboratory measurements of sand samples from the Namib desert, Namibia. *Remote Sensing of Environment*, 113, 1313-1318, <https://doi.org/10.1016/j.rse.2009.02.018>.
- Ichoku, C., & Ellison, L. (2014). Global top-down smoke-aerosol emissions estimation using satellite fire radiative power measurements. *Atmospheric Chemistry and Physics*, 14(13), 6643-6667, doi:10.5194/acp-14-6643-2014.
- Ichoku, C., Ellison, L.T., Willmot, K. E., Matsui, T., Dezfuli, A. K., Gatebe, C. K., . . . & Habib, S. (2016). Biomass burning, land-cover change, and the hydrological cycle in northern sub-saharanAfrica. *Environmental Research Letters*, 11(9), doi:10.1088/1748-9326/11/9/095005.
- Isiorho, S. A., & Nkereuwem, O. T. (1996). Reconnaissance study of the portion of the Lake Chad. *Journal of Environmental & Engineering Geophysics 1*(1), 47-54.
- Justice, C. O., Giglio, L., Korontzi, S., Owens, J., Morisette, J. T., Roy, D., Descloitres, J., Alleaume, S., Petitcolin, F., & Kaufman, Y. (2002). The MODIS fire products. *Remote Sensing of Environment*, 83, 244–262.
- Kimmage, K., & Adams, W. M. (1992). Wetland agricultural production and river basin development in the Hadejia-Jama'are Valley, Nigeria. *The Geographical Journal* 158: 1-12.
- Kindler, J., Warshall, P., Arnould, E. J., Hutchinson, C. F., & Varady, R. (1990). *The Lake Chad Conventional Basin - a diagnostic study of the environmental degradation*. Report prepared for the U.N. Environment Program and U.N. Sudano-Sahelian Office by the Office of Arid Land Studies. University of Arizona, Tuscon, AZ.
- Lake Chad Basin Commission. (1966). Study of water resources in the Lake Chad Basin / Hydrogeology.
- Leblanc, M., Favreau, G., Maley, J., Nazoumou, Y., Leduc, C., Stagnitti, F., van Oevelen, F., Delclaux, P. J., & Lemoalle, J. (2006). Reconstruction of Megalake Chad using shuttle radar topographic mission data. Science Direct. *Palaeogeography, Palaeo-climatology, Palaeoecology*, 239, 16–27.
- Leblanc, M., Favreau, G., Tweed, S., Leduc, C., Razack, M., & Mofor, L. (2007). Application of remote sensing and GIS for groundwater modeling of large semiarid areas: Example of the Lake Chad Basin, Africa. *Hydrology of the Mediterranean and Semiarid Regions, Proceedings of an International Symposium held at Montpellier, IAHS 278*, 186–192.

- LeCoz, M., Delclaux, F., Genthon, P., & Favreau, G. (2009). Assessment of Digital Elevation Model (DEM) Aggregation methods for hydrological modeling: Lake Chad Basin, Africa. *Journal of Computers & Geosciences* 35, 1661–1670.
- Li, F., Lawrence, D.M., & Bond-Lamberty, B. (2018). Human impacts on 20th century fire dynamics and implications for global carbon and water trajectories. *Global and Planetary Change*, 162, 18-27.
<https://doi.org/10.1016/j.gloplacha.2018.01.002>.
- Li, M., & Shao, Q. (2010) An improved statistical approach to merge satellite rainfall estimates and raingauge data. *Journal of Hydrology*, 385, 51–64,
<https://doi.org/10.1016/j.jhydrol.2010.01.023>.
- Lyons E., Jin Y., & Randerson, J. (2008) Changes in surface albedo after fire in boreal forest ecosystems of interior Alaska assessed using MODIS satellite observations. *Journal of Geophysical Research*. 113(G02012), doi:10.1029/2007JG000606.
- Maier, S.W., Ebke, W., & Ruppert, T. (2004) MODIS-Processing at DLR/DFD. *Presented at MODIS Workshop, Perth, Australia*.
http://www.eoc.csiro.au/modis/nov02_ws/dlr_dfd.pdf
- Masuoka, E., Fleig, A., Wolfe, R.E., & Patt, F. (1998). Key characteristics of MODIS data products. *IEEE Transactions of Geoscience and Remote Sensing*, 36(4), 1313–1323.
- Mughal, M.O., Lynch, M., Yu, F., McGann, B., Jeanneret, F., & Sutton, J. (2017) Wind modelling, validation and sensitivity study using weather research and forecasting model in complex terrain. *Environmental Modelling & Software*, 90, 107–125.
<https://doi.org/10.1016/j.envsoft.2017.01.009>.
- Musa, I. K. (2008). *Saving Lake Chad*. Proceedings of Sirte Roundtable. Lake Chad Basin Commission and International Commission of Irrigation (LCBC and ICID), December 17. Libya.
- Ndehedehe, C. E., Awange, J. L., Kuhn, M., Agutu, N. O., & Fukuda, Y. (2017). Climate teleconnections influence on West Africa's terrestrial water storage. *Hydrological Processes*, 31(18), 3206-3224, doi:10.1002/hyp.11237.
- Nicholson, S. E., Some, B., & Kone, B. (2000). An analysis of recent rainfall conditions in west Africa, including the rainy seasons of the 1997 el nino and the 1998 la nina years. *Journal of Climate*, 13(14), 2628–2640.
- Nicholson, S. (2013). The West African Sahel: A review of recent studies on the rainfall regime and its interannual variability. *ISRN Meteorology*. (453521).

- Notaro, M., Wyrwoll, K. H., & Chen, G. (2011). Did aboriginal vegetation burning impact on the Australian summer monsoon? *Geophysical Research Letters*, 38(L11704), doi:10.1029/2011GL047774.
- Nyman, P., Smith, H. G., Sherwin, C. B., Langhans, C., Lane, P. N. J., & Sheridan, G. J. (2015). Predicting sediment delivery from debris flows after wildfire. *Geomorphology*, 250, 173–186, doi:10.1016/j.geomorph.2015.08.023.
- Ojo, J. S., & Omotosho, T. V. (2013). Comparison of 1-min rain rate derived from TRMM satellite data and rain gauge data for microwave applications in Nigeria. *Journal of Atmospheric and Solar-Terrestrial Physics*, 102, 17–25, <https://doi.org/10.1016/j.jastp.2013.04.008>.
- Oliver, F. C., & Singels, A. (2012). The effect of crop residue layers on evapotranspiration, growth and yield of irrigated sugarcane. *Water SA*38(1), 77–86.
- Penman, H. L. (1963). *Technical communication No. 53*. Commonwealth Bureau of Soils. Harpenden, Harpenden, England.
- Polivka, T. N., Wang, J., Ellison, L. T., Hyer, E. J., & Ichoku, C. M. (2016). Improving nocturnal fire detection with the VIIRS day–night band. *IEEE Transactions on Geoscience and Remote Sensing*, 54(9), 5503–5519, doi: 10.1109/TGRS.2016.2566665
- Pombo, S., & Proença de Oliveira, R. (2015). Evaluation of extreme precipitation estimates from TRMM in Angola. *Journal of Hydrology*, 523, 663–679, <https://doi.org/10.1016/j.jhydrol.2015.02.014>.
- Ramillien, G., Frappart, F., & Seoane, L. (2014). Application of the regional water mass variations from GRACE satellite gravimetry to large-scale water management in Africa. *Remote Sensing*, 6(8), 7379–7405. doi:10.3390/rs6087379
- Rulli, M. C., Offeddu, L., & Santini, M. (2013). Modeling post-fire water erosion mitigation strategies. *Hydrology and Earth System Sciences*, 17(6), 2323–2337. doi:10.5194/hess-17-2323-2013.
- Saha, M. V., D'Odorico, P., & Scanlon, T. M. (2017). Albedo changes after fire as an explanation of fire-induced rainfall suppression. *Geophysical Research Letters*, 44(8), 3916–3923. doi:10.1002/2017GL073623.
- Sanogo, S., Fink, A. H., Omotosho, J. A., Ba, A., Redl, R., & Ermert, V. (2015). Spatio-temporal characteristics of the recent rainfall recovery in West Africa. *International Journal of Climatology*, 35(15), 4589–4605. doi:10.1002/joc.4309.

- Sarch, M. T. (2001). Fishing and farming at Lake Chad: Institutions for access to natural resources. *Journal of Environmental Management*, 62(2), 185–199, <https://doi.org/10.1006/jema.2001.0430>.
- Schulze, E. D., & Küppers, M. (1979). Short-term and long-term effects of plant water deficits on stomatal response to humidity in *Corylusavellana* L. *Planta* 146, 319–326,doi: 10.1007/BF00387804.
- Schuster, M., Roquin, C., Durringer, P., Brunet, M., Caugy, M., Fontugne, M., Mackaye, H.T., Vignaud, P., & Ghienne J.-F. (2005). Holocene Lake Mega-Chad Palaeoshorelines from space. *Quaternary Science Reviews*, 24, 1821–1827.
- Schwartz, F. W., & Zhang, H. (2003). *Fundamentals of ground water*. New York: Wiley.
- Seeber, K. (2013) 2nd Mission on Discharge Measurements at Chari, Logone and Koulambou River, Chad. 2010.2274.8. BGR-No.: 05-2355.
- Shuttleworth, W. J. (1993). *Evaporation*. McGraw-Hill, New York.
- Schneider, J. L., & Wolff, J. P. (1992). Geologic maps of hydrogeology of the Republic of Chad. Document BRGM; 209.
- Sun, G., Ranson, K. J., Kharuk, V. I., & Kovacs, K. (2003). Validation of surface height from shuttle radar topography mission using shuttle laser altimeter. *Remote Sensing of Environment*, 88(4), 401–411, <https://doi.org/10.1016/j.rse.2003.09.001>.
- Thonicke, K., Venevsky, S., Sitch, S., & Cramer, W. (2001). The role of fire disturbance for global vegetation dynamics: Coupling fire into a dynamic global vegetation model. *Global Ecology and Biogeography*, 10, 661–677.
- Tsiko, C. T., Makurira, H., Gerrits, A. M. J., & Savenije, H. H. G. (2012). Measuring forest floor and canopy interception in a savannah ecosystem. *Physics and Chemistry of the Earth, Parts A/B/C*(47–48), 122–127, ISSN 1474-7065, doi: 10.1016/j.pce.2011.06.009.
- Valiantzas, J. D. (2006). Simplified versions for the penman evaporation equation using routine weather data. *Journal of Hydrology*, 331(3-4), 690–702, doi:10.1016/j.jhydrol.2006.06.012.
- van der Werf, G. R., Randerson, J. T., Giglio, L., Collatz, G. J., Mu, M., Kasibhatla, P. S., Morton, D. C., DeFries, R. S., Jin, Y. & van Leeuwen, T. T. (2010) Global fire emissions and the contribution of deforestation, savanna, forest, agricultural, and peat fires (1997–2009) *Atmospheric Chemistry and Physics*, 10, 11707–35.

- vanZyl, J. J. (2001). The Shuttle Radar Topography Mission (SRTM): A breakthrough in remote sensing of topography. *Acta Astronautica*, 48(5 – 12), 559–565.
- Vintrou, E., Desbrossea, A., Beguea, A., Traoreb, S., Barona, C., & Seena, D., (2012). Crop area mapping in West Africa using landscape stratification of MODIS time series and comparison with existing global land products. *International Journal of Applied Earth Observations and Geoinformation* 14(1),83–93.
- Wan, Z., & Li, Z. L. (2010). Radiance-based validation of the V5 MODIS land-surface temperature product. *International Journal of Remote Sensing*, 29(17–18), 5373–5395, DOI: 10.1080/01431160802036565
- World Health Organization. (2012). *Cholera Country Profile: Cameroon*. Date accessed May 1, 2014.
<http://www.who.int/cholera/countries/CameroonCountryProfile2011.pdf>
- World Health Organization. (2017). *Lake Chad Basin Humanitarian Response Plan 2017*. <http://www.who.int/emergencies/response-plans/2017/lake-chad-basin/en/>
- Yang, Y., Xiao, P., Feng, X., & Li, H. (2017). Accuracy assessment of seven global land cover datasets over China. *ISPRS Journal of Photogrammetry and Remote Sensing* 125, 156–173, <https://doi.org/10.1016/j.isprsjprs.2017.01.016>.
- Yu, X., & Lu, C. (2014). Urban percent impervious surface and its relationship with land surface temperature in Yantai City, China. *IOP Conference Series: Earth and Environmental Science (EES)*, 17(1), 7, doi:101088/1755-1315/17/1/012163.
- Zhang, W., Brandt, M., Guichard, F., Tian, Q., & Fensholt, R. (2017). Using long-term daily satellite based rainfall data (1983–2015) to analyze spatio-temporal changes in the sahelian rainfall regime. *Journal of Hydrology*, 550, 427–440, doi:10.1016/j.jhydrol.2017.05.033.
- Zomer R. J., Trabucco, A., Bossio, D. A., van Straaten, O., & Verchot, L. V. (2008). Climate change mitigation: A spatial analysis of global land suitability for clean development mechanism afforestation and reforestation. *Agriculture, Ecosystems, and Environment*, 126, 67–80.
- Zomer R. J., Bossio, D.A., Trabucco, A., Yuanjie, L., Gupta, D. C., & Singh, V. P. (2007). Trees and water: smallholder agroforestry on irrigated lands in northern India. *Colombo, Sri Lanka: International Water Management Institute*, 45. (IWMI Research Report 122).
<https://ageconsearch.umn.edu/bitstream/53067/2/RR122.pdf>.

VITA

Forrest Weston Black was born on December 23, 1986 in Kansas City, Missouri. In 2010 he graduated Summa Cum Laude earning a Bachelor of Arts Degree in Geography and a GIS certification from the University of Missouri - Kansas City. In the spring of 2014, he returned to The University of Missouri - Kansas City to begin work toward a Master Degree in Environmental and Urban Geosciences. During his research there, he worked as a graduate research assistant funded by NASA and the NSF on the project "Interactions and feedbacks between biomass burning and water cycle dynamics across the Northern Sub-Saharan African (NSSA) region". He also worked as lead graduate research assistant for environmental science labs from Fall 2015 to May 2016.

From August 2016 to August 2017 he worked as an intern for the Crew Systems and Aviation Operations Branch of NASA Langley Research Center in Hampton, Virginia. During his time at NASA he developed software which allowed pilots to view current weather forecasts from numerical weather models. He also assisted in developing software tools allowing aeronautical researchers to view real-time flight simulations to be viewed in Google Earth.

He currently works in Kansas City as a Aeronautical GIS Specialist as contract support for the Federal Aviation Administration (FAA). Forrest can be contacted at forrest.w.black@gmail.com.